Universidade de Aveiro Departamento de Electrónica e Telecomunicações

1999

Carlos Alberto da Costa Bastos

A model for the simulation of Doppler ultrasound signals from pulsatile blood flow

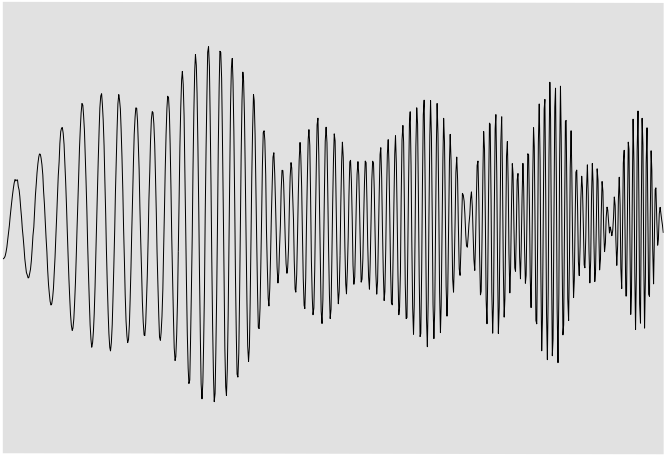

Carlos Alberto da Costa Bastos

A model for the simulation of Doppler ultrasound signals from pulsatile blood flow

Um modelo para a simulação de sinais Doppler ultra-sónicos provenientes de fluxo sanguíneo pulsátil

Thesis submitted to the Universidade de Aveiro for the degree of Doctor of Philosophy in Electrical Engineering under the supervision of Mr. Peter Fish, Reader in the School of Electronic Engineering and Computer Systems of the University of Wales–Bangor, United Kingdom, and Dr. Francisco Vaz, Professor of the Departamento de Electrónica e Telecomunicações of the Universidade de Aveiro

Dissertação apresentada à Universidade de Aveiro para cumprimento dos requesitos necessários à obtenção do grau de Doutor em Engenharia Electrotécnica, realizada sob a orientação científica de Mr. Peter Fish, Professor da School of Electronic Engineering and Computer Systems da University of Wales–Bangor, Reino Unido, e do Dr. Francisco Vaz, Professor Catedrático do Departamento de Electrónica e Telecomunicações da Universidade de Aveiro

o jurí / examiners committee
presidente / president

Prof. Doutor Casimiro Adrião Pio
professor catedrático de Universidade de Aveiro por delegação do Reitor da Universidade de Aveiro

Prof. Doutor Francisco António Cardoso Vaz
professor catedrático da Universidade de Aveiro (orientador)

Prof. Doutor José Alberto dos Santos Rafael
professor associado da Universidade de Aveiro

Prof. Doutor António Miguel Pontes Pimenta Monteiro
professor auxiliar da Faculdade de Engenharia da Universidade do Porto

Prof. Doutor Augusto Marques Ferreira da Silva
professor auxiliar da Universidade de Aveiro

Prof. Doutor José Carlos da Silva Cardoso
professor auxiliar da Universidade de Trás-os-Montes e Alto Douro

Mr. Peter John Fish
Reader na School of Electronic Engineering and Computer Systems da University of Wales-Bangor, Reino Unido (co-orientador)

agradecimentos / acknowledgements

I would like to express my most sincere thanks to Mr. Peter Fish and Prof. Dr. Francisco Vaz for their supervision, critical suggestions, support, assistance, patience and advice throughout the course of this work. Without their help and support this work would probably never exist.

I thank all my colleagues but specially Tomás Oliveira e Silva, Osvaldo Pacheco and Luís Almeida at Aveiro, and Robin Steel and José Carlos Cardoso at Bangor, for their friendship, support and encouragement. The help of Tomás with the Latex word processor and daily incentive during the last stages of writing up are gratefully acknowledged. Also Robin's help in finding a solution for the integral in Appendix A has to be mentioned.

I thank the Universidade de Aveiro, the Departamento de Electrónica e Telecomunicações, the School of Electronic Engineering and Computer Systems of the University of Wales–Bangor, and INESC Aveiro, for providing the means and the environment that made this work possible. I extend my thanks to the staff members of these institutions that contributed in any way to my work.

The financial support of Fundação para a Ciência e Tecnologia (formerly JNICT) through a CIENCIA grant extended to a PRAXIS grant is gratefully acknowledged. The PRAXIS grant benefited from the support of the Science and Technology Subprogram of the 2^{nd} Community Support Framework (Sub-Programa Ciência e Tecnologia do 2^{o} Quadro Comunitário de Apoio). Thanks are also due to Fundo Social Europeu for supporting Universidade de Aveiro with a PRODEP grant that provided the financial means for part of my work.

I would like to thank my parents, my sister and my grandparents for their love, support and encouragement during the course of this work.

Very special thanks and love to my wife Olga and my daughter Inês for their unconditional love and patience throughout the course of this work and the long absences at Bangor. Olga's sacrifice of her own professional career to join me in Bangor for a complete year is also gratefully acknowledged.

Resumo

O detector ultra-sónico de fluxo sanguíneo usa o efeito Doppler para estimar de forma não invasiva a velocidade do sangue na circulação. Tem sido bastante usado nas últimas quatro décadas para detectar a presença de estenoses.

O desenvolvimento de novas técnicas de processamento do sinal Doppler necessita de sinais de teste cujas características sejam conhecidas ou possam ser medidas com precisão. Isto é difícil de obter com sinais Doppler medidos *in vivo* devido à elevada variação do fluxo sanguíneo de pessoa para pessoa e também com o estado fisiológico da pessoa no momento da medida, por exemplo a tensão arterial influencia significativamente o fluxo sanguíneo. Um modelo para gerar sinais Doppler simulados cujas características sejam controláveis e/ou mensuráveis é uma ferramenta bastante útil, pois permite que as novas técnicas de processamento do sinal Doppler sejam testadas em condições controladas. Permite, também, estudar o efeito de vários factores que afectam o espectro do sinal Doppler. Habitualmente o efeito individual dos vários factores não pode ser identificado quando são usados sinais medidos *in vivo*.

Neste trabalho foi desenvolvido um modelo para gerar sinais Doppler ultra-sónicos simulados. O modelo contém dois sub-modelos, um para o fluxo sanguíneo nos membros inferiores de um ser humano e outro para gerar os sinais simulados a partir do campo de velocidades do sangue e das características do instrumento.

O fluxo sanguíneo nos membros inferiores foi simulado com um análogo eléctrico para a rede vascular dos membros inferiores. Cada artéria foi simulada por uma linha de transmissão com perdas e as redes vasculares periféricas por um circuito *Windkessel* com três elementos. O circuito eléctrico foi implementado com o simulador de circuitos SPICE.

Para simular a interacção entre os glóbulos vermelhos e o campo de ultra-sons o vaso sanguíneo foi dividido em pequenos volumes elementares. As contribuições dos volumes elementares foram todas somadas para gerar o sinal Doppler simulado. O modelo fez algumas aproximações como sejam, por exemplo, considerar o fluxo sanguíneo laminar e sem rotação.

As características dos sinais gerados pelo modelo são bastante parecidas com as esperadas para o sinal Doppler real. O modelo desenvolvido foi usado para estudar a influência que a aceleração sanguínea, o tamanho do volume de amostragem e a duração da janela de amostragem têm na largura de banda eficaz do espectro do sinal Doppler. Foi deduzida uma fórmula que estima a largura de banda eficaz a partir das contribuições individuais do alargamento espectral devido à não estacionaridade, do alargamento espectral intrínseco, do alargamento espectral devido à duração da janela de amostragem e ainda da gama das velocidades que passam pelo volume de amostragem.

Foram, ainda, deduzidas expressões em forma fechada para o espectro de potência do sinal Doppler devido unicamente à gama de velocidades que atravessam um volume de amostragem com forma Gaussiana colocado num perfil de velocidades com forma exponêncial. Foram, também, obtidas expressões para a largura de banda eficaz no caso especial do volume de amostragem Gaussiano ter simetria esférica e estar colocado no centro do vaso sanguíneo.

Abstract

The Doppler ultrasonic blood flow detector estimates non-invasively the velocity of blood in the circulatory system. It has been extensively used in the last four decades for the detection of stenoses in the circulation.

The development of new signal processing techniques for the Doppler signal requires test signals with known or measurable characteristics. This is very difficult to achieve with Doppler signals obtained *in vivo* because of the variability of blood flow between persons and with physiological state, for example blood pressure. A model for generating simulated Doppler signals whose characteristics are controllable and/or measurable is a useful tool because it permits the test of new processing techniques under controlled conditions. It permits also the study of the effect of various factors on the Doppler spectrum. Usually these effects cannot be isolated with *in vivo* measurements.

During this work a model for the generation of simulated Doppler ultrasound signals was developed. It comprised two sub-models one for blood flow in the human lower limb and the other for generating simulated signals from the blood velocity field and the instrument's characteristics.

Blood flow in the lower limb was modelled by an electric analogue for the lower limb vascular tree. Each artery was modelled by a lossy transmission line and the peripheral vascular beds by three–element *Windkessel* models. The electric analogue circuit was implemented with the SPICE circuit simulator.

To simulate the inter-action of the blood cells with the ultrasonic field the vessel was divided into small elemental volumes whose contributions were added together to generate the simulated Doppler signal. The model assumed irrotational laminar flow and some other simplifying approximations.

The characteristics of the signals generated by the model were similar to those expected for the Doppler signal. The model was used to study the influence of blood acceleration, sample volume size and data segment duration on the root mean square (rms) width of the Doppler spectrum. A simple formula was derived for estimating the Doppler rms spectral width from the individual contribution of non-stationarity broadening, intrinsic broadening, window broadening and the range of blood velocities passing through the sample volume.

In addition closed form expressions were derived for the Doppler power spectrum due solely to the range of blood velocities passing through a Gaussian sample volumes placed in irrotational laminar flow with a velocity profile obeying a simple power law. Closed form expressions were also obtained for the root mean square spectral width in the special case of a spherically symmetric Gaussian sample volume placed in the centre of the vessel.

À Olga,
à Inês, à Ana Raquel
e aos meus pais

Contents

List of Figures

List of Tables

List of Symbols

Δa range of accelerations within the sample volume;

Δp -pressure difference between two points;

Δr width of a circular flow shell;

$\Psi(y)$ relation between pulsatile volumetric flow and velocity profile;

Ω_m moment of order m of the power spectrum;

α Womersley parameter; scaling factor in the Bessel Distribution; R_0/σ_{sv} in Chapter 5;

α_p $R_0\sqrt{p\,\omega_1/\nu}$;

β $\arctan(z_0\,\sigma_y^2/y_0\,\sigma_z^2)$ in Chapter 5; constant mean frequency variation in Chapter 6;

$\chi(y)$ phase of $\Psi(y)$;

δ angle between the transmitter and receiver beams in continuos wave systems;

$\delta(\omega)$ Delta function;

ϵ_p phase of the pth harmonic of $\overline{v}(t)$;

ϵ_r error in σ_{b1} that arises from assuming that Δa is negligible;

ϕ phase shift angle;

ϕ_{qm} phase of Doppler signal from elemental volume qm at $t = 0$;

ϕ_{1qm} phase;

γ_h propagation constant;

$\gamma(a, x)$ incomplete gamma function;

λ wavelength;

μ fluid viscosity;

ν kinematic viscosity;

θ angle between the direction of scatterer movement and the beam (bisector of the transmitter and receiver beams in continuous wave systems);

ρ fluid density;

σ scaling factor in the Choi-Williams Distribution; root mean square spectral width; standard deviation of a white noise source; Poisson ratio;

σ_1 rms width of $|W_1(\omega)|^2$;

σ_b rms width of $S_b(\omega)$;

σ_{b1} rms width of $S_{b1}(\omega)$;

$\sqrt{\sigma_{bs}}$ backscattering cross-section;

σ_G rms width of $S_G(\omega)$;

$\sigma(n, \alpha)$ rms width of the Doppler spectrum from a power law velocity profile (n) passing through a spherically symmetrical Gaussian sample volume ($\alpha = R_0/\sigma_{\rm sv}$);

$\sigma_{\rm sv}$ rms width of a spherically symmetric Gaussian sample volume;

σ_t rms width of $w^2(t)$;

σ_w rms width of the energy spectrum of the window function;

$\sigma_{x'}, \sigma_{y'}, \sigma_{z'}$ rms widths of a Gaussian sample volume along the x', y' and z' axes;

σ_y $\sqrt{\sigma_{y'}^2 \cos^2(\theta) + \sigma_{x'}^2 \sin^2(\theta)}$;

σ_z σ_z';

ω angular frequency;

$\overline{\omega}$ mean angular frequency;

ω_0 transmitted angular frequency;

ω_1 fundamental angular frequency of $\overline{v}(t)$;

ω_d Doppler angular frequency shift;

ω_{d0} central streamline Doppler angular frequency shift;

$\omega_d(y, z)$ Doppler angular frequency shift from a flow streamline at position (y, z);

$\omega_d'(r, \phi)$ Doppler angular frequency shift from a flow streamline at position $(r\phi)$;

A amplitude of signal;

A_{qm} amplitude of signal from elemental volume qm;

A_q^2 $E[A_{qm}^2]$;

$A(z)$ z transform of the numerator of the transfer function of a linear digital filter, $H(z)$;

$\mathrm{BD}(t, \omega)$ Bessel time-frequency distribution;

$B(z)$ z transform of the denominator of the transfer function of a linear digital filter, $H(z)$;

C constant;

C' electric capacitance per unit length;

C_h' flow capacitance per unit length;

C_p peripheral compliance of a vascular bed;

$\mathrm{CWD}(t, \omega)$ Choi Williams time-frequency distribution;

E Young's modulus of the blood vessel wall;

$\mathrm{E}[\,]$	expectation operator;
$F_{qm}(\omega, t_w)$	Fourier transform of the deterministic part of the Doppler signal from an elemental volume;
G'	electric conductance per unit length;
G'_h	flow conductance per unit length;
G_{leak}	total electrical conductance accounting for blood 'leakage' in the electrical model of an artery;
$G_{qm}(.)$	beam sensitivity along the path of elemental volume qm;
$G(\vec{r}(t))$	beam sensitivity across the scatterer's path;
$G(x, y, z)$	beam sensitivity;
$H(z)$	transfer function of a linear digital filter;
I	electric current;
I_d	degree of distortion of $G(.)$;
I_k	modified Bessel function of order k;
I_{out}	current driven by the input generator to the lower limb model;
$I(\omega)$	periodogram;
$I_{\mathrm{ave}}(\omega)$	averaged periodogram;
$I_{\mathrm{win}}(\omega)$	windowed periodogram;
J_i	Bessel function of order i;
K	constant;
L'	electric inertance per unit length;
L'_h	flow inertance per unit length;
$\mathrm{M}(a, b, \beta)$	$\int_0^{2\pi} \exp\left(a\cos(\phi - \beta) + b\cos(2\phi)\right)\, d\phi$;
M'_{10}, ϵ'_{10}	functions used by Womersley to relate pulsatile pressure gradient to volumetric flow;
N	number of samples; number of lossless transmission line sections in the lumped model of lossy transmission lines;
O	origin of the vessel coordinate system;
O'	origin of the beam coordinate system;
PI	pulsatility index of a flow waveform or a spectrogram;
Q	volumetric flow;
Q_{in}	inflow;
Q_{out}	outflow;
R	fluid resistance;
R'	electric resistance per unit length;
R_0	internal radius;

Re Reynolds number;

R'_h flow resistance per unit length;

R_{in} equivalent resistor of the input current generator of the lower limb model;

R_p peripheral resistance of a vascular bed;

R_s series resistors in the lumped model of a transmission line;

R_t transverse resistors in the lumped model of a transmission line;

R_v electrical equivalent of R_{vh};

R_{vh} total flow resistance accounting for viscous losses in an artery;

$S(\omega)$ power spectrum;

$S(\omega, t_w)$ Dopper power spectrum at time t_w;

$S_b(\omega)$ power spectrum of $s_b(t, t_w)$;

$S_{b1}(\omega)$ baseband spectrum without intrinsic broadening;

$S_G(\omega)$ energy spectrum of $G\left(\overline{v}(t_w)(t - t_w) + \int_{t_w}^{t} \overline{v}_d(\tau)\, d\tau, y_0, z_0\right)$;

$S_q(\omega, t_w)$ Dopper power spectrum from elemental tube q;

$S_{qm}(f)$ Doppler power spectrum from elemental volume qm;

$S_{\text{AR}}(\omega)$ power spectral density of the output of and autoregressive filter;

$S_{\text{ARMA}}(\omega)$ power spectral density of the output of and autoregressive-moving average filter;

$S_{\text{MA}}(\omega)$ power spectral density of the output of and moving average filter;

$S_{\text{norm}}(\omega)$ normalised Doppler power spectrum;

$S_{\text{STFT}}(t, \omega)$ short-time Fourier transform;

$S_{\text{spec}}(t, \omega)$ spectrogram;

T_D window duration;

$U(\omega)$ step function;

V electric voltage;

$W_K(\omega)$ square of the absolute value of the Fourier transform of the window function, $w_K(k)$;

$W(\omega)$ Fourier transform of the window function, $w(t)$;

$W_1(\omega)$ Fourier transform of $w_1(t, t_w)$;

$W'(r, \phi)$ power of the Doppler signal received from a flow streamline at position (r, ϕ);

$W_{\text{sh}}(r)$ power returned by a flow shell at a distance r from the centre of the vessel;

$W(y, z)$ power of the Doppler signal received from a flow streamline at position (y, z);

$\text{WVD}(t, \omega)$ Wigner-Ville time-frequency distribution;

Y_{th} transverse flow admittance per unit length;

Z electric impedance;

Z_h flow impedance;

Z_{0h} characteristic flow impedance;

Z_{lh} longitudinal flow impedance per length;
Z_{th} transverse flow impedance times unit length;

a acceleration;
a_{qm} acceleration of elemental volume qm;
c speed of propagation of the sound;
c_0 pulse wave velocity;
d distance across the sample volume;
$d(t)$ Doppler signal from a single scatterer passing through a finite ultrasonic beam;
$d_{id}(t)$ Doppler signal from a single scatterer passing through a plane wave unit-amplitude infinite wide ultrasonic field;
e natural number;
f frequency;
f_0 transmitted frequency;
f_d Doppler frequency shift;
f_{d0} central streamline Doppler frequency shift;
$f_{d_{\max}}$ maximum frequency shift detectable by a pulsed wave system;
f_r received frequency;
f_{rs} frequency received by a scatterer;
h vessel wall thickness;
j imaginary unit number;
$\vec{k}$ wave vector;
k wave number (modulus of the wave vector);
l length;
m elemental volume;
n exponent of power law velocity profile;
p pressure;
p_0, p_1, p_2 coefficients of a second order polynomial;
q elemental tube;
qm elemental volume m in elemental tube q;
$\vec{r}(t)$ trajectory;
r radial distance from the centre of the tube/vessel;
r_n distance between the centre of a circular flow shell and the centre of the vessel;
$r_{ww}(k)$ autocorrelation of the window function $w_K(k)$;
$r_{xx}(\tau)$ autocorrelation function of $x(t)$;
$\hat{r}_{xx}(k)$ estimate of the autocorrelation function;

(r, ϕ, z) cylindrical coordinate system;

$s(t)$ Doppler signal;

$s_b(t, t_w)$ part of the Doppler signal describing the effect of the beam and the velocity variation within the beam;

$s_{\mathrm{mod}}(t, t_w)$ part of the Doppler signal consisting in a modulation at the mean Doppler frequency shift;

$s_q(t)$ Doppler signal from elemental tube q;

$s_w(t, t_w)$ Doppler signal during a window centred on time t_w;

t time;

t_r fixed reference time;

t_w time corresponding to the centre of a time window;

$u_{qm}(t)$ Doppler signal from elemental volume qm;

v velocity;

$\overline{v}$ mean velocity;

$\overline{v}(t)$ mean velocity waveform; spatial mean velocity within the sample volume;

$\overline{v}_d(t)$ difference between $\overline{v}(t)$ and the mid-window velocity, $\overline{v}(t_w)$;

$\overline{v}(t_w)$ mid-window velocity;

$v(r)$ velocity profile;

v_0 velocity of the central streamline;

v_{dqm} difference between the velocity of elemental volume qm and its mid-window velocity;

$v_{qm}(t)$ velocity waveform of elemental volume qm;

v_p magnitude of the pth harmonic of $\overline{v}(t)$;

v_r radial component of velocity;

v_x longitudinal component of velocity;

$v(y_1, t)$ time varying velocity profile;

var[ ] variance;

$w_K(k)$ window function;

$w(t)$ window function;

$w(t - t_w)$ time window function centred on time t_w;

$w_1(t, t_w)$ part of the Doppler signal consisting in a complex chirp with an envelope equal to the window function and a frequency variation given by the acceleration-induced change in spatial mean frequency during the window;

x longitudinal coordinate;

$x(n)$ input of a linear digital filter;

$x(t)$ stochastic process; time signal; time variation of the longitudinal distance;

x, y, z	coordinate system for the vessel;
x', y', z'	coordinate system for the ultrasonic beam;
x_{qm}, y_{qm}, z_{qm}	position of elemental volume qm in the vessel coordinate system;
x_{qm0}	position along the x axis at $t = 0$;
y	normalised radial coordinate, r/R_0, in Chapter 2; one of the coordinate axes;
$y(n)$	output of a linear digital filter;
y_1	normalised radial coordinate, r/R_0, in Chapter 4;;
(y_0, z_0)	coordinates of sample volume centre in the vessel coordinate system;

List of Acronyms

AORT	AORTa artery;
AR	AutoRegressive;
ARMA	AutoRegressive-Moving Average;
ATA	Anterior Tibial Artery;
BD	Bessel Distribution;
DC	Direct Current;
CFA	Common Femoral Artery;
CFD	Computational Fluid Dynamics;
cgs	centimetre-gram-second system of units;
CNS	Central Nervous System;
CO_2	carbon dioxide;
CW	Continuous Wave;
CWD	Choi Williams Distribution;
FFT	Fast Fourier Transform;
FIR	Finite Impulse Response;
MA	Moving Average;
PI	Pulsatility Index;
POP	POPliteal artery;
PRF	Pulse Repetition Frequency;
PW	Pulsed Wave;
rms	root mean square;
SPICE	Simulation Program with Integrated Circuit Emphasis;
STFT	Short-Time Fourier Transform;
WVD	Wigner-Ville Distribution;

List of Publications

Bastos, C. A. C., Fish, P. J. & Vaz, F. [1999], 'Spectrum of Doppler ultrasound signals from nonstationary blood flow', *IEEE Transactions on Ultrasonics, Ferroelectrics, and Frequency Control* **46**(5), 1201–1217.

Bastos, C. A. C., Fish, P. J., Steel, R. & Vaz, F. [1999], 'Doppler power spectrum from a Gaussian sample volume'. submitted for publication in Ultrasonics.

Bastos, C. A. C., Fish, P. J. & Vaz, F. [1997], Acceleration effects in Doppler ultrasound signals from pulsatile flow, *in* 'Proceedings of the 19th Annual International Conference of the IEEE Engineering in Medicine and Biology Society, Chicago, Illinois, USA, October 30-November 2', Vol. 19, pp. 238–241.

Bastos, C. A. C., Fish, P. J. & Vaz, F. [1996], A model for generating Doppler ultrasound signals from pulsatile blood flow, *in* 'Proceedings of the 18th Annual Conference of the IEEE Engineering in Medicine and Biology Society, Amsterdam, The Netherlands, October 31-November 3', Vol. 18, p. 1.3.1.

Bastos, C. A. C., Fish, P. J. & Vaz, F. [1996], A Doppler ultrasound signal model for steady flow, *in* 'Proceedings of BioEng'96, 4th Portuguese Congress on Biomedical Engineering, Aveiro, Portugal, April 18–19', pp. VIII.3.1–3.

Bastos, C. A. C., Fish, P. J. & Vaz, F. [1994], Simulação do fluxo sanguíneo no membro inferior com um análogo eléctrico, *in* 'Proceedings of the 3rd Portuguese Congress on Biomedical Engineering, Porto, Portugal, November 24–26', p. 3.

Bastos, C. A. C., Fish, P. J. & Vaz, F. [1994], Model of lower limb blood flow using SPICE, *in* 'Abstracts of the World Congress on Medical Physics and Biomedical Engineering, Rio de Janeiro, Brazil, August 21–26', p. 217. Published in Physics in Medicine and Biology, Vol 39a, Part 1.

Chapter 1

Introduction

1.1 Overview

Cardiovascular diseases like heart attacks and embolic strokes are leading causes of death or severe disability in the population of the so called "developed world". Better and more sensitive techniques capable of detecting, at an early stage, the conditions that often precede such diseases, for example the formation of arterial plaque and the partial blockage of the vessel lumen by stenoses, are needed in order to improve the efficiency and the outcome of medical treatments. These diagnostic techniques should be low cost, since expensive methods are not suitable for the large scale testing required to detect the diseases at an early stage.

The ultrasonic Doppler blood flow detector, usually in conjunction with an ultrasonic imaging instrument, has been the technique of choice in the detection of stenosed vessels because it is a non-invasive technique performed at lower cost than some other diagnostic modalities, e.g. magnetic resonance imaging.

The ultrasonic Doppler blood flow detector determines the blood velocity by measuring the Doppler shift in the frequency of ultrasound backscattered by the moving blood cells making use of the Doppler effect named after the Austrian physicist Christian Doppler (1803-1853). The Doppler effect is the change in frequency sensed by an observer when moving in relation to a wave source.

In essence, ultrasound is transmitted towards the blood vessel under investigation, backscattered ultrasound is received on a transducer and the electrical signal from this is demodulated, i.e. multiplied by the transmitted signal, and low pass filtered to produce a signal, the Doppler signal, whose frequency is proportional to the velocity of the moving blood cells.

The Doppler signal is random because the ultrasound is scattered from a large number of blood cells with a random distribution. Due to the range of blood cells velocities passing through the instrument's resolution cell (sample volume), amongst other effects discussed later, the Doppler signal contains a complete spectrum of frequencies instead of a single frequency [Evans et al. 1989]. Even the Doppler signal scattered from a single blood cell

contains a spectrum of frequencies rather than a single frequency due to the finite path length of the blood cell within the resolution cell.

Blood flow is pulsatile due to the intermittent pumping action of the heart and as a consequence the frequency content of the Doppler signal also varies with time. Thus the Doppler signal is non-stationary, that is its statistics change with time and is usually approximately cyclo-stationary because the cardiac cycle and the physiological state change slowly with time.

The velocity waveform at any site of the arterial circulation is determined by the condition of the complete vascular system and its physiological state. For example, vasodilatation of vessels of one limb affects not only the local blood velocity waveforms, by changing the local flow impedance, but also the waveforms at other sites in the circulation and eventually even the output of the heart.

The shape of the time variation of the mean or maximum frequency of the Doppler spectrum and any abnormal increase in the range of frequencies (spectral width) are used to detect the presence of stenoses in vessels. Usually a broader Doppler spectrum is associated with disturbed flow created by an obstructive lesion. Thus, the lower limit of stenoses that can be detected is determined by the sensitivity to small degrees of flow disturbance and this is conditioned by the method of spectral analysis used [Fish 1991] and the characteristics of the measuring system.

Ideally, the width of the Doppler spectrum should be determined only by the range of blood velocities passing through the instrument's sample volume, but in practice several other factors like blood acceleration, scattering characteristics of blood, sample volume characteristics and window duration, contribute to the spectrum [Gill 1985, Fish 1991, Jones 1993]. In order to lower the limit of detectable flow disturbances it is necessary to understand and quantify the effect of each factor on the Doppler spectrum allowing the development of new analysis techniques.

The impossibility of controlling vascular conditions in a person and the high variability of the Doppler signal obtained from different persons (even from the same person at different times) makes the task of obtaining clinical Doppler signals under controlled conditions almost impossible.

It seemed, then, interesting to develop a model for the generation process of the Doppler signal. This would allow the generation of simulated Doppler signals under controlled conditions thus enabling the study of the relative importance of various factors on the Doppler spectral width. The use of the model would also help in the development of new methods of waveform analysis and disease state prediction and their test under controlled conditions, avoiding the use of long, time consuming, clinical trials in the development phases.

The work presented here is part of a broader effort, by our research group, aimed at improving the sensitivity of the Doppler flow detector to smaller degrees of arterial stenoses. This broader goal includes also the study of the autonomous regulation of blood flow and the development of techniques for model based vascular disease detection.

This is an interdisciplinary work involving knowledge in various areas like physiology of the circulation, fluid dynamics, physics, signal processing and electrical engineering.

1.2 Objectives

The main objective of this work is the development of a computer model for the generation process of the ultrasonic Doppler signal capable of producing signals with controllable and repeatable characteristics. The model can be subdivided into the following two models:

- Computer model of the blood flow in the lower limb arterial tree.
- Computer model for the beam/velocity field interaction with input of sample volume characteristics and the velocity field produced by the blood flow model, and output of the simulated Doppler signal.

We have chosen to model the blood flow of the lower limb arterial tree because it is one of the parts of the arterial circulation were stenosis are more common and also because it is composed of relatively straight and long vessels.

Another important objective of this work is to study the influence of blood acceleration, sample volume size and window duration on the width of the Doppler spectrum.

1.3 Thesis organization

This first Chapter presents a general overview of medical Doppler ultrasound and the motivations for this work. This Chapter also lists the main objectives of this work and achievements.

Chapter 2 has some background on the areas of knowledge relevant to this work, that is, blood flow, medical Doppler ultrasound theory and instrumentation, and spectral estimation of Doppler signals. It briefly describes the circulatory system and the different types of blood flow usually found in the circulation. The section on Doppler ultrasound introduces the Doppler effect and Doppler ultrasound instruments used as medical diagnosis tools; it also describes contributing factors to the Doppler spectrum as well as models for the Doppler signal. The section on spectral estimation describes the various techniques that have been used to estimate the spectrum of the Doppler signal.

Chapter 3 describes the implementation of an electric analogue for the lower limb arterial circulation using the SPICE circuit simulator.

Chapter 4 presents a new computer model for the generation of simulated Doppler signals from non steady laminar blood flow. The model uses as inputs the characteristics of the

sample volume and the velocity field. It can generate either simulated Doppler signals or the expected spectrum of the signals.

Chapter 5 presents the derivation of a closed expression for the Doppler power spectrum from a sample volume with a Gaussian sensitivity variation placed anywhere in a vessel with a power law velocity profile. It presents, also, closed form expressions for the mean frequency and root mean square (rms) width of the Doppler spectrum in the special case of a symmetric Gaussian sample volume centred in the vessel.

In Chapter 6 the new formulation for the Doppler signal introduced in Chapter 4 is used as the basis for an investigation into the various factors affecting the Doppler spectrum. This allowed the study of the relative contribution of blood acceleration, sample volume size and window duration to the spectral width of the Doppler signal.

This thesis ends in Chapter 7 with a summary of the work carried out and some suggestions for future work.

1.4 Main contributions

- Development of an electric analogue model of the blood flow in the lower limb arterial circulation using SPICE, an industry standard for the simulation of electric circuits. This was an ideal platform on which to develop the model because it was very easy to change the model parameters and the circuit description file is highly portable. The qualitative validation of the model looked into the Pulsatility Index (PI) of the flow waveforms in addition to other model outputs.

- Development of a software model for the generation of simulated Doppler ultrasound signals received from irrotational non steady blood flow in straight rigid vessels. The model is closely linked to physical the characteristics of the Doppler instrument and since the velocity of the scatterer's is allowed to vary while crossing the sample volume the model is suitable to study the effects of acceleration on the Doppler spectrum. The way in which the Doppler system was modelled permitted the computation of the expected power spectrum thus enabling the removal of the randomness from the simulated spectrum.

- Derivation of closed form expressions for the Doppler power spectrum from Gaussian sample volumes placed anywhere in a vessel with a n^{th} power velocity profile[1].

- Derivation of closed form expressions for the mean frequency and root mean square (rms) spectral width of Doppler signals from symmetric Gaussian sample volumes placed in the centre of vessels with a power law velocity profile.

[1] The solution of the integral $\int_0^{2\pi} \exp\left(a\cos(\phi-\beta)+b\cos(2\phi)\right)\, d\phi$ presented in Appendix A was found with the help of Dr. Robin Steel from the University of Wales, Bangor, UK.

- New formulation for the Doppler ultrasound signal that allows the separation of the effect of blood acceleration, sample volume size and data window duration on the spectral width of the Doppler signal[2].
- Model based numerical study of the effect of blood acceleration, data window duration and sample volume size on the rms spectral width of the Doppler spectrum.
- Introduction of a simple formula for estimating the rms spectral width under some idealised conditions[2].

[2]The theoretical development presented in Chapter 6 resulted from collaborative work between the author and one of his supervisors, Mr. Peter Fish.

Chapter 2

Background

2.1 Introduction

This chapter describes the background knowledge for the general areas of this interdisciplinary work.

Firstly, blood flow in humans is described in section 2.2. The description includes the circulatory system, types of blood flow encountered in humans and models and theories to describe blood flow in the circulatory system.

Secondly, Doppler ultrasound is presented in section 2.3. The section includes: a description of the basic physical principles behind the Doppler effect; a description of the most common Doppler ultrasound instruments; the description of the origins of the Doppler spectrum and models proposed in the past to describe the Doppler signal backscattered by blood.

Finally, the basics of spectral estimation techniques usually used to process the Doppler signal are presented in section 2.4. The periodogram, parametric modelling and time-frequency spectral estimation techniques are all briefly described.

2.2 Blood flow

This section briefly describes the flow of blood in the human circulatory system. It starts with the physiology of the circulatory system and its main components: heart, vessels and blood. The types of blood flow commonly found in the human circulation are also described and the section ends with the description of models for the blood flow in arteries.

No outline of the history of hemodynamics is made in this work. Very good reviews on the main contributions to the present knowledge on blood flow in the human circulation can be found in [Fich & Li 1983, Milnor 1989, Nichols & O'Rourke 1990, Noordergraaf 1969].

2.2.1 The circulatory system

The circulatory system consists of the heart, which pumps the blood, the blood vessels and the blood. Its main functions are the transport of substances (nutrients, oxygen and hormones)

to the cells and the removal of products and wastes of the cellular metabolism (e.g., carbon dioxide).

The human vascular system is shown diagrammatically in figure 2.1 to illustrate how the various components of the circulation are interconnected and how the blood is distributed in the different parts of the circulatory system.

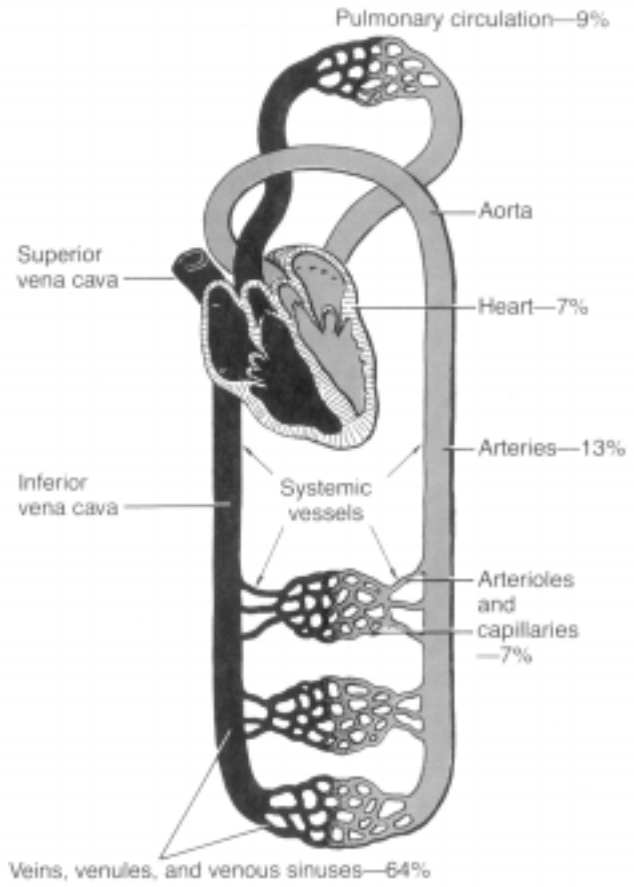

Figure 2.1: Diagram of the human vascular system and the distribution of blood volume in the different portions of the circulatory system (from [Guyton 1991]).

The heart

The human heart is a hollow muscle situated in the chest cage between the lungs. It has the general shape of a pyramid turned up side down [Reith et al. 1978].

The heart functions as two pumps arranged in series. The right side of the heart pumps blood to the lungs (pulmonary circulation) via the pulmonary artery and the left side to the rest of the body (systemic circulation) via the aorta [Stanier & Forsling 1990].

The heart is divided into four chambers: right atrium, left atrium, right ventricle and left ventricle. The blood enters the heart at the atria and leaves it forced by the ventricular

contractions. The blood flow in the heart is unidirectional due to the use of valves; the atrioventricular valves between the atria and the ventricles, and the semilunar valves in the base of the main arteries (aorta and pulmonary artery) leaving the ventricles. Figure 2.2 shows the heart and the major blood vessels connected to it.

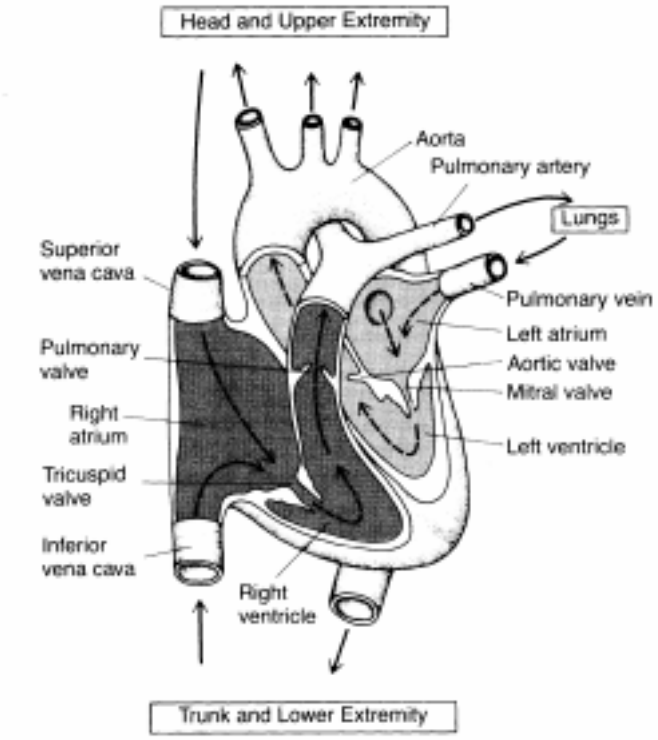

Figure 2.2: The structure of the heart and the flow of blood through the heart chambers (from [Guyton 1991]).

During its life, the heart is constantly pumping blood to the arteries in a cyclic succession of muscle contraction and relaxation.

The normal cardiac rate in humans is on average approximately 70 beats per minute [Jacob et al. 1990]. This rhythmic nature of the heartbeat is an intrinsic property of some parts of its musculature (myocardium fibres). The heart rate may be modified by several factors (chemical composition of blood, temperature and nerve impulses), but the initiation of the beat is myogenic: that is to say, a property of the myocardium muscle fibres themselves [Stanier & Forsling 1990]. The resting heart rate is mainly determined by the inherent rhythm of the fastest beating portion of the myocardium, and by signals from two sets of nerve fibres (one to accelerate and another to slow down the heart) that connect heart to the central nervous system (CNS). The CNS uses the blood temperature and the information received from several strategically placed sensory organs, which measure the pressure (baroreceptors) and the chemical composition of blood (chemoreceptors), to regulate the heart rate.

Blood vessels

The blood vessels in the human body are classified into the following groups: arteries, arterioles, capillaries, venules, and veins.

The arteries carry the blood from the heart to the main regions of the body: head, trunk and limbs. The arteries close to the heart have large diameters in order to accommodate the high blood flow rates, but as the arteries successively branch they get narrower. The walls of the large arteries have a significant percentage of elastic fibres that contribute to smoothing out the pressure wave delivered by the heart. The elasticity of the arterial walls allows the sudden intake of blood ejected from the ventricles during systole, the walls then recoil squeezing the blood into the arterioles [Stanier & Forsling 1990]. With age, arteries lose their elasticity, resulting in strain on the arterial wall. Figure 2.3 shows the physical structure of the arterial wall.

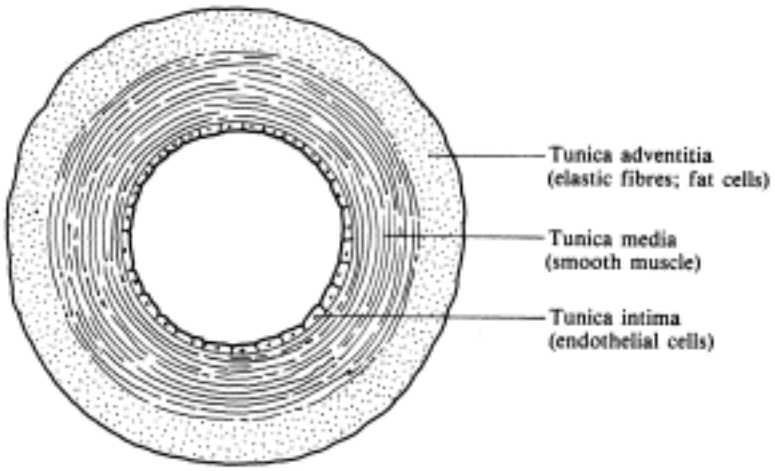

Figure 2.3: Cross-section of an artery (from [Stanier & Forsling 1990]).

From the arteries, the blood passes to the arterioles that are directly connected to the capillaries. The arterioles may be dilated or constricted through the action of the smooth muscle contained in their walls. This ability of the arterioles to change their diameter allows the CNS to adjust the blood flow rate to the various parts of the body according to their physiological needs. The CNS controls the diameter of the arterioles by changing the frequency of the nervous impulses sent to the smooth muscle of the arterioles.

From the arterioles, the blood passes to the capillaries where the exchange of nutrients, waste products and gases with the individual cells occurs. The capillaries are the smaller vessels of the circulatory system, their walls consist of a single layer of endothelial cells and do not contain any smooth muscle or elastic fibres. The capillaries connect the arterial and

venous trees.

The veins and the venules are the vessels that transport the blood back to the heart. They have thinner walls than their arterial counterparts, arteries and arterioles respectively, because the blood pressure on their walls is much smaller. While arterial blood is propelled by the action of the heart, venous blood is manly propelled by the action of the muscles surrounding the veins. The muscles squeeze the thin walls of the veins forcing the blood forward to the heart. Valves prevent blood from flowing backwards.

Blood

The blood is the liquid substance that is pumped through the blood vessels by the heart. It is the medium for the transport of substances between the different parts of the body. Among the many functions of blood some of the most important are:

- Transport of nutrients to the cells;
- Transport of oxygen from the lungs to the cells;
- Transport of metabolism waste products (for example, carbon dioxide) from the cells to the organs of excretion;
- Transport of hormones through the body.

The blood is formed essentially of erythrocytes (red blood cells), leukocytes (white blood cells), and platelets in suspension in the plasma.

The main function of the erythrocytes is to transport oxygen from the lungs to the tissues and carbon dioxide (CO_2) from the tissues to the lungs. The oxygen combines in the lungs with hemoglobin (a molecule contained in the erythrocytes) and is then transported to the cells where it oxidises the nutrients for energy.

Although, about 98% of the oxygen in the blood is carried by the hemoglobin, only about 25% [Reith et al. 1978] of the CO_2 is carried by the hemoglobin. The major fraction of CO_2 present in the blood reacts with the water contained in the blood. This is possible because of the *carbonic anhydrase* enzyme contained in the erythrocytes which is responsible for accelerating the rate of reaction between water and CO_2 about 5000-fold [Guyton 1991].

The leukocytes are the cells that provide defences against any infectious agent that might be present in the body and the platelets help to prevent blood loss from ruptured vessels.

2.2.2 Types of blood flow

When two adjacent layers of a fluid slide over each other a frictional force arises between them due to viscosity.

Viscosity is a physical property of a fluid. For most simple fluids (e.g. water) viscosity is independent on the rate at which the adjacent fluid layers slide over each other (shear rate) and those fluids are usually referred as Newtonian fluids.

Blood is a mixture of solid cells (erythrocytes, leukocytes and platelets) in suspension in the liquid plasma therefore the viscous properties of blood are complex. Fortunately, it is possible to neglect the non-Newtonian behaviour of blood viscosity for the major arteries in the human circulation [Caro et al. 1978, Evans et al. 1989, Hatle & Anglesen 1985] and consider the asymptotic value of blood viscosity, that is the value to which the apparent viscosity tends at high shear rates. Although asymptotic viscosity depends on both hematocrit (percentage of blood volume that is made of cells) and temperature, its value at normal physiological conditions is in the range 3–4 $\times 10^{-3}\mathrm{N\,s\,m^{-2}}$ [Caro et al. 1978, Milnor 1989].

The flow of a fluid within closed vessels may be of two different types: laminar or turbulent. In laminar (or streamline) flow the fluid particles move along smooth paths in layers with every layer sliding smoothly over its neighbour [Evans, 1989, pp 7]. As the velocity increases, laminar flow becomes unstable, vortices start to form, and eventually flow becomes turbulent.

When the flow is turbulent the velocity vectors of the fluid particles change rapidly with time, both in magnitude and direction.

Blood flow in arteries is complex. The flow is pulsatile, the blood is an inhomogeneous fluid, and branches, curves, tapers, and arterial obstructions cause even more complexity [Evans et al. 1989].

Laminar flow

In a circular long rigid straight tube, steady laminar flow of a Newtonian fluid gives rise to a parabolic velocity profile across the tube lumen. The fluid moves in cylindrical layers; the central layer moves with maximal velocity and the fluid near the wall is almost stationary.

The parabolic velocity profile of laminar flow is:

$$v(r) = v_0 \left[1 - \left(\frac{r}{R_0}\right)^2\right] \qquad , 0 \le r \le R_0 \tag{2.1}$$

where $v(r)$ is the velocity of the fluid layer at distance r from the centre of the tube, v_0 is the velocity of the central layer and R_0 is the internal radius of the tube.

The rate of fluid flow, Q, sometimes also referred as volumetric flow, may be calculated by integrating $v(r)$ over the tube cross-section:

$$\begin{aligned} Q &= \int_0^{2\pi} \int_0^{R_0} v(r) r \, dr d\theta \\ &= \pi R_0^2 \, \frac{v_0}{2} \end{aligned} \tag{2.2}$$

The mean velocity, $\overline{v} = v_0/2$, is obtained by dividing the volumetric flow by the tube cross-sectional area.

The relationship between volumetric flow and pressure gradient in a segment of a circular

rigid tube with steady laminar flow is given by Poiseuille's (1799-1869) law:

$$\Delta p = p_1 - p_2 = \frac{8\mu Q l}{\pi R_0^4} \tag{2.3}$$

where p_1 and p_2 are the pressures at the beginning and end of the tube, μ is the fluid viscosity and l is the length of the tube.

If we rewrite Poiseuille's law as:

$$\begin{aligned} \frac{\Delta p}{Q} &= \frac{8\mu l}{\pi R_0^4} \\ \Delta p &= RQ \qquad\qquad , \; R = \frac{8\mu l}{\pi R_0^4} \end{aligned} \tag{2.4}$$

it is easy to see the parallel with the familiar Ohm's law, which relates a steady electrical current trough a device to the potential difference across its terminals. Due to this analogy between the electrical and fluid realities, the constant R is usually referred as the fluid resistance.

Turbulent flow

At high velocities, laminar flow tends to become turbulent; the trajectories of the fluid particles seem to be erratic and random.

The velocity at which flow becomes turbulent depends on the geometry of the tube and on the physical properties of the fluid. This critic velocity cannot be exactly predicted, but it is closely related to the Reynolds number, Re, which for a circular pipe is:

$$Re = \frac{2R_0\overline{v}}{\nu} \tag{2.5}$$

where ν is the kinematic viscosity of the fluid.

Although, the critical Reynolds number (at which the flow becomes turbulent) depends on the tube geometry, for most practical purposes related to blood flow in human arteries, it is taken to be approximately 2000 [Evans et al. 1989]. Whenever there is any intrusion, like for example a stenosis, into the vessel lumen turbulence can develop at much lower Reynolds numbers.

The average velocity profile found in turbulent blood flow is flatter than that found in laminar flow [Evans et al. 1989].

When the flow is turbulent a significant fraction of blood flow energy is lost to form eddies resulting in a higher flow resistance to flow than in the case of laminar flow [Hatle & Anglesen 1985].

Turbulent blood flow is rarely seen in the normal human circulation but vortices do form in and near the heart. Turbulent flow in the circulation usually develops as a result of vascular disease (e.g. arterial stenoses). This is explored by some diagnostic techniques, such as Doppler ultrasound, to detect sites with arterial disease.

Pulsatile flow

The blood flow in arteries is pulsatile due to the intermittent pumping of the heart. The pulsatile nature of arterial blood flow and the viscoelastic properties of the arterial walls imply the propagation of pressure and velocity waves along the arterial tree with a finite pulse velocity.

The equation for the velocity of pulse propagation in a thin-walled eslastic tube filled with and incompressible and nonviscous liquid was first derived in the 19th century by two Dutch scientists and is known as the Moens-Korteweg equation,

$$c_0 = \sqrt{\frac{Eh}{2\rho R_0}} \tag{2.6}$$

where c_0 is the pulse wave velocity, E is the Young's modulus of the tube wall, ρ is the density of the fluid and h is the wall thickness.

A number of more complex equations taking into account parameters such as the viscosity of the liquid were also derived. Nevertheless, equation (2.6) predicts the pulse wave velocity with an error not exceeding 15% of the values measured in the human arteries, which is well within normal experimental error and physiological variability [Caro et al. 1978].

Poiseuille's law gives the relationship between the pressure gradient and the volumetric flow for steady flow. [Womersley 1955*a*] showed that a similar expression holds for the case of sinusoidal flow in a rigid circular tube,

$$Q = \frac{M'_{10}}{\alpha^2} \times \frac{\pi R_0^4}{\mu l} \Delta p \sin\left(\omega t + \phi + \epsilon'_{10}\right) \tag{2.7}$$

for a pressure gradient of $\Delta p \cos(\omega t + \phi)/l$, ω is the angular frequency of the velocity waveform, t is time and ϕ is a phase shift angle. M'_{10} and ϵ'_{10} are both functions of the non-dimensional parameter α know as Wormersley parameter defined as:

$$\alpha = R_0 \sqrt{\frac{\omega}{\nu}} \tag{2.8}$$

From the above equation it is clear that the pressure and flow waveforms are generally not in phase.

The velocity profile for steady flow in a circular pipe is parabolic. In the case of pulsatile flow the velocity profile depends on α. The relationship between sinusoidal volumetric flow, $Q(t) = Q\cos(\omega t + \phi)$, and the velocity profile in a rigid tube was derived by Evans [1982*a*] from Womersley's equations:

$$v(y) = \frac{1}{\pi R_0^2} \times Q\,|\Psi(y)| \cos\left(\omega t + \phi + \chi(y)\right) \tag{2.9}$$

where $y = r/R_0$ and $|\Psi(y)|$ and χ are respectively the magnitude and phase of function:

$$\Psi(y) = \frac{\tau J_0(\tau) - \tau J_0(y\tau)}{\tau J_0(\tau) - 2J_1(\tau)} \qquad ,\tau = \alpha j^{3/2} \tag{2.10}$$

where j is the unit imaginary number, J_0 and J_1 are Bessel functions of the first kind and orders 0 and 1.

If the flow waveform is periodic, then it may be expressed as a Fourier series:

$$Q(t) = \ Q_0 + \sum_{k=1}^{\infty} Q_k \cos\left(k\omega t + \phi_k\right) \tag{2.11}$$

and the actual velocity profile is given by the summation (assuming that the system is linear) of the profiles for each single frequency [Evans 1982*b*]:

$$v(y) = \frac{1}{\pi R_0^2}\left[2Q_0\left(1-y^2\right) + \sum_{k=1}^{\infty} Q_k\left|\Psi_k\right|\cos\left(k\omega t + \phi_k + \chi_k\right)\right] \tag{2.12}$$

For very small α the flow varies very slowly and the velocity profile is approximately parabolic.

2.2.3 The effects of geometric changes

Each curve, branch and constriction in the circulatory system changes both the velocity profile and the local pressure gradient [Evans et al. 1989].

Curves

The flow pattern in a curved section of a vessel is changed by the centrifugal force acting on the fluid. This force is proportional to the velocity squared and inversely proportional to the radius of curvature. When the profile at the entrance of the curve is parabolic the fluid at the centre has the highest velocity and will tend to move towards the outside wall of the vessel [Evans et al. 1989] and the profile becomes skewed in that direction.

If the velocity profile is flat at the entrance of the curve, the profile in the curve becomes skewed in the direction of the inner wall because the radius of curvature is smaller for the streamlines near the inner wall.

Branches

Blood flow at (or near) the branch point of a vessel is very complex. Factors like the mismatch in size, characteristic impedance and angle of branching contribute to determine the characteristics of the flow in the daughter and parent vessels.

The effect of the branch on the velocity profile depends on the exact geometry of the junction. Normally, there is flow separation and secondary motion near the inner wall of the

daughter vessel. These sites where flow separation and secondary motion occur naturally are common sites for the occurrence of atherosclerosis, an example of such site in the circulation is the carotid bifurcation.

The characteristic impedance mismatch at branches produces reflected pressure and flow waves that interact with the incident waves. Thus, arterial branches (and also stenosis) change the pressure and flow waveforms both locally and globally.

It is important to note that the flow in curves and at branches is nonlinear and therefore the behaviour of a pulsatile flow waveform cannot be predicted by adding the contributions of individual sinusoidal waves [Evans et al. 1989].

Tapering

All the blood vessels, with the exception of the capillaries, taper. A converging lumen has the effect of stabilising laminar flow, flattening the velocity profile and rising the critical Reynolds number.

The major blood vessels also show some degree of elastic tapering (i.e. the Young's modulus of the vessel changes progressively with distance), which also contributes to stabilising the blood flow in the circulation.

Stenoses

The most frequent arterial disease is atherosclerosis in which atheromatous plaque develops inside the arterial wall. With time these plaques may grow larger and invade the vessel lumen thus reducing blood flow and eventually obstructing the vessel completely. The obstructive lesions caused by the deposition of plaque in the arterial wall are normally called stenoses.

When a vessel has a stenosis the cross-section of the lumen is reduced and the stenosis contributes with an extra resistance to the flow of blood. Since the volumetric flow remains constant throughout the narrowing, the blood inside the stenosis needs to travel at a higher velocity than outside the stenosis. The pressure drop in a stenosis is higher than that predicted by Poiseuille's law. In addition to the pressure drop due to viscous losses (Poiseuille's law) there are also pressure drops due to nonlinear effects associated with the convergence and divergence of the flow and to the pressure-difference needed to accelerate the blood [Young et al. 1975]. The exact contribution of each of the above effects to the pressure drop at a stenosis depends on the geometry of the stenosis.

Whenever the vessel widens suddenly (for example after a stenosis) the inertia of the flowing blood may lead to the separation of flow and eventually the formation of eddies. Depending on the severity of the vessel narrowing and the volumetric blood flow, the eddies produced by the stenosis may rapidly die away or the flow may even become turbulent [Evans et al. 1989].

Doppler ultrasound is normally used to detect the flow disturbance caused by the stenoses. Usually, the eddies and/or turbulence that occur after the stenosis produce broader Doppler

spectra due to the higher range of velocities passing through the sample volume. The mean frequency waveform is also usually changed in the vicinity of a stenosis; for example if there is a mild to severe stenosis in the common femoral artery, the spectrogram downstream the stenosis may not contain the negative frequencies normally associated with the reverse flow in the lower limb.

If a vessel becomes blocked or the volumetric flow through it is significantly reduced (severe stenosis) the body usually adapts by developing and opening collateral vessels to supply the vascular bed [Guyton 1991]. The flow supplied by the collateral circulation may be enough to feed the vascular bed under resting conditions but the collateral vessels rarely ever become large enough to supply the blood flow needed during strenuous activities.

2.2.4 Models of arterial blood flow

The *Windkessel* model

In 1733 Stephen Hales (cited in [Milnor 1989]) suggested that the arterial system is similar to an old fire engine system. He viewed the arterial system as an elastic fluid reservoir that converted an intermittent inflow into a fairly steady outflow. His suggestion led Otto Frank in 1899 to propose a theoretical model for the arterial system in order to compute the cardiac output from arterial pressure recordings. The model proposed by Otto Frank (cited in [Milnor 1989]) is known nowadays as the *Windkessel* which is the German word for the compression chamber of the old fire engines. A schematic representation of the *Windkessel* model is shown in figure 2.4.

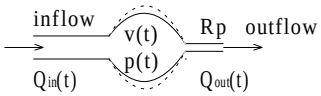

Figure 2.4: The *Windkessel* model.

The *Windkessel* model represents the microcirculation by a single resistance to flow and the systemic arterial circulation as an elastic chamber that expands when $Q_{in} > Q_{out}$ and recoils again when $Q_{in} < Q_{out}$. This buffering action was considered to be similar to the smoothing of the flow waveform by the arterial system.

The *Windkessel* model may also be represented by an electric equivalent circuit as shown in figure 2.5. The capacitor C_p represents the compliance of the systemic arterial circulation and R_p the total peripheral resistance.

The *Windkessel* model assumes that any pressure perturbations are "felt" simultaneously at any site within the arterial system, that is the same to say that the pressure waves travel with infinite wave velocity in the arterial system. This assumption is in clear contradiction to the real behaviour of the mammalian arterial system.

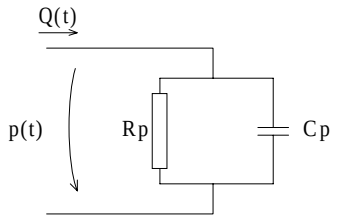

Figure 2.5: Electric equivalent of the *Windkessel* .

Several attempts were made to improve the *Windkessel* model but its built-in contradictions and its impossibility to model the pressure pulse in the circulation as a travelling wave led to search for new ways to describe the dynamics of the circulation. Nevertheless, the *Windkessel* model and its derivations like the *Westkessel* [Westerhof et al. 1971, Noordergraaf 1978]

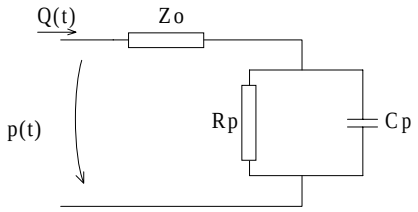

Figure 2.6: The *Westkessel* model.

shown in figure 2.6 are still being used to model the load impedance seen by the heart or as termination impedances of large vessels. The *Windkessel* represents the load of the more peripheral vessels and the microcirculation. The *Westkessel* model mimics the frequency variation of the input impedance of the arterial tree much better than the *Windkessel* model [Westerhof et al. 1971].

Some examples of the recent use of the *Windkessel* and *Westkessel* models can be found in [Avanzolini et al. 1989, Burkhoff et al. 1988, Chen et al. 1997, Mo et al. 1988, Toy et al. 1985].

Womersley's theory

Although, Womersley's work on pulsatile blood flow was not the first of its kind, his systematic and extensive treatment of blood flow had tremendous impact on the study of hemodynamics.

Womersley successively studied the flow in a rigid cylindrical tube [Womersley 1955*a*], in a thin-walled elastic tube [Womersley 1955*b*] and in a constrained elastic tube [Womersley 1957].

The model for pulsatile flow proposed by Womersley is sometimes referred as a linearized model because he neglected the nonlinear terms of the Navier-Stokes equations after showing that their effect should be small when applied to blood flow. A detailed description of several linear models for blood flow may be found in [Cox 1969].

The Navier-Stokes equations for a Newtonian incompressible fluid flow free of rotational flow are [Noordergraaf 1969]:

$$-\frac{\partial p}{\partial x} = \rho\left[\frac{\partial v_x}{\partial t} + v_r\frac{\partial v_x}{\partial r} + v_x\frac{\partial v_x}{\partial x}\right] - \mu\left[\frac{\partial^2 v_x}{\partial r^2} + \frac{1}{r}\frac{\partial v_x}{\partial r} + \frac{\partial^2 v_x}{\partial x^2}\right] \tag{2.13}$$

$$-\frac{\partial p}{\partial r} = \rho\left[\frac{\partial v_r}{\partial t} + v_r\frac{\partial v_r}{\partial r} + v_x\frac{\partial v_r}{\partial x}\right] - \mu\left[\frac{\partial^2 v_r}{\partial r^2} + \frac{1}{r}\frac{\partial v_r}{\partial r} + \frac{\partial^2 v_r}{\partial r} - \frac{v_r}{r^2}\right] \tag{2.14}$$

where x is the longitudinal distance and v_x and v_r are respectively the longitudinal and radial components of the velocity.

[Womersley 1955*a*] studied laminar irrotational flow of an incompressible Newtonian fluid in an infinite long (with no reflections) rigid cylindrical tube. Under these conditions equation (2.14) is eliminated and v_r, $\partial v_x/\partial x$, and $\partial^2 v_x/\partial x^2$ are zero. The Navier-Stokes equations are then reduced to:

$$-\frac{\partial p}{\partial x} = \rho\frac{\partial v_x}{\partial t} - \mu\left[\frac{\partial^2 v_x}{\partial r^2} + \frac{1}{r}\frac{\partial v_x}{\partial r}\right] \tag{2.15}$$

Womersley further assumed that the pressure gradient was a function of time only and considered a sinusoidal pressure gradient (expressed as a complex quantity for simplicity),

$$-\frac{\partial p}{\partial x} = Ae^{j(\omega t+\phi)} \tag{2.16}$$

substituting (2.16) into the equation of motion,

$$\frac{\partial^2 v_x}{\partial r^2} + \frac{1}{r}\frac{\partial v_x}{\partial r} - \frac{\rho}{\mu}\frac{\partial v_x}{\partial t} = \frac{A}{\mu}e^{j(\omega t+\phi)} \tag{2.17}$$

Womersley considered then the longitudinal velocity as $v_x = u\,e^{j\omega t}$ where u is a function of r alone and made the following substitutions, $y = r/R_0$ and $\alpha = R_0\sqrt{\omega/\nu}$. The equation of motion was then rewritten as:

$$\frac{\partial^2 u}{\partial y^2} + \frac{1}{y}\frac{\partial u}{\partial y} - j\alpha^2 u = \frac{R_0}{\mu}Ae^{j\phi} \tag{2.18}$$

whose solution is:

$$v_x = A\frac{R_0^2}{\mu}\frac{1}{j^3\alpha^2}\left[1 - \frac{J_0\left(\alpha j^{3/2}\,y\right)}{J_0\left(\alpha j^{3/2}\right)}\right]e^{j(\omega t+\phi)} \tag{2.19}$$

The fluid volumetric flow is the integral of the velocity across the tube cross-section:

$$\begin{aligned} Q &= 2\pi R_0^2 \int_0^1 v_x y \, dy \\ &= \frac{\pi A R_0^4}{\mu j^3 \alpha^2} \left[1 - \frac{2J_1\left(\alpha j^{3/2}\right)}{\alpha j^{3/2} J_0\left(\alpha j^{3/2}\right)} \right] e^{j(\omega t + \phi)} \end{aligned} \tag{2.20}$$

For a real pressure gradient given by $\Delta p/l \cos(\omega t + \phi)$ we get:

$$Q = \frac{M'_{10}}{\alpha^2} \frac{\pi R_0^4}{\mu l} \Delta p \sin\left(\omega t + \phi + \epsilon'_{10}\right) \tag{2.21}$$

which is equal to (2.7). The quantities M'_{10} and ϵ'_{10} are the magnitude and phase of the expression between the square brackets in (2.20).

The volumetric flow is only in phase with the pressure when $\epsilon'_{10} = 90^o$ i.e. when $\alpha \ll 1$.

Comparing (2.21) with Poiseuille's law (2.3) it can be seen that the frequency dependent factor M'_{10}/α^2 takes the place of the constant 1/8 in Poiseuille's law. Figure 2.7 shows the variation of M'_{10}, M'_{10}/α^2 and ϵ'_{10} as functions of α.

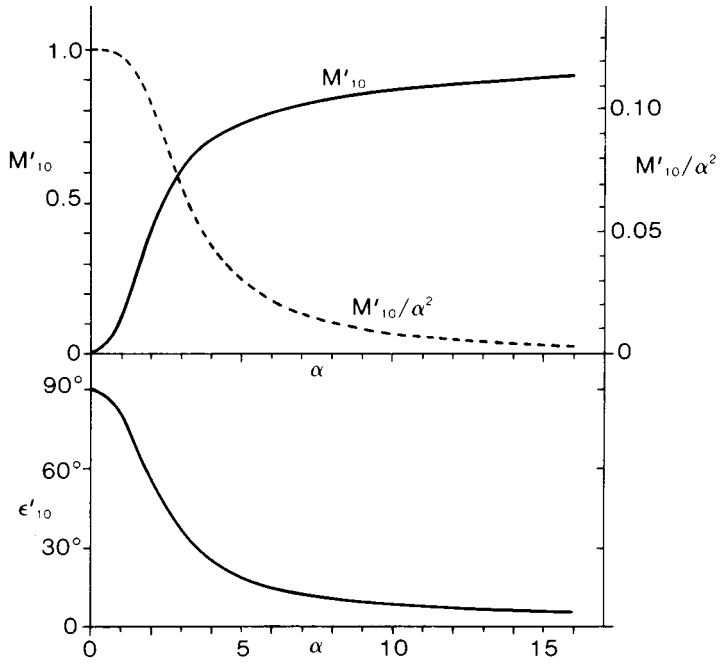

Figure 2.7: M'_{10}, M'_{10}/α^2 and ϵ'_{10} as functions of Womersley's parameter α (from [Milnor 1989]).

Transmission line models

The transmission of pressure and flow waves through arteries has strong similarities with the propagation of voltage and current waves in electrical transmission lines [Noordergraaf 1969]. The correspondence between hemodynamic and electric quantities may be made in two different ways, but the most generally used is the one that "translates" pressure into voltage and volumetric flow into electric current.

The equations that describe the transmission of the electric signals through an uniform transmission line are usually known as the "telegraph equations":

$$-\frac{\partial V}{\partial x} = L'\frac{\partial I}{\partial t} + R'I \tag{2.22}$$

$$-\frac{\partial I}{\partial x} = G'V + C'\frac{\partial V}{\partial t} \tag{2.23}$$

where V is voltage, I is current, L' is inductance per unit length, R' is resistance per unit length, G' is conductance per unit length and C' is capacitance per unit length. The schematic for an infinitesimally small block of an electric transmission line is shown in figure 2.8.

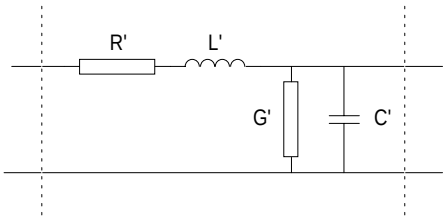

Figure 2.8: Infinitesimally small transmission line element.

The Navier-Stokes equation for $\partial p/\partial x$ (2.13) may be simplified to a form similar to that of (2.22) [Milnor 1989, Noordergraaf 1969] if some basic assumptions are made:

- the inertial longitudinal and convective acceleration terms, $v_r\frac{\partial v_x}{\partial r}$ and $v_x\frac{\partial v_x}{\partial x}$, can be neglected;
- the three viscous terms are equivalent to a resistor multiplied by the volumetric flow;
- axial flow is unaffected by radial oscillations;
- "leakage" of flow through lateral branches or through the wall is directly proportional to pressure.

These conditions are not fully met in the blood circulation. Nevertheless, it is remarkable that experimental studies have found that pressure and flow harmonics *in vivo* closely approximate those predicted by linear models [Milnor 1989]. The major discrepancy being an underestimation of the DC resistance in the linear models, which may possibly arise from neglecting the convective acceleration term [Milnor 1989].

Making use of the above simplifications, the Navier-Stokes equations and a continuity equation expressing the conservation of mass may be written as:

$$-\frac{\partial p}{\partial x} = L'_h \frac{\partial Q}{\partial t} + R'_h Q \tag{2.24}$$

$$-\frac{\partial Q}{\partial x} = G'_h p + C'_h \frac{\partial p}{\partial t} \tag{2.25}$$

where L'_h is flow inertance per unit length, R'_h is flow resistance per unit length, G'_h is flow leakage per unit length and C'_h is vessel compliance per unit length.

Defining the longitudinal flow impedance per unit length as Z_{lh} and the transverse flow admittance per unit length as Y_{th}:

$$Z_{lh} = -\frac{\partial p/\partial x}{Q} \tag{2.26}$$

$$Y_{th} = \frac{1}{Z_{th}} = -\frac{\partial Q/\partial x}{p} \tag{2.27}$$

where Z_{th} is called the transverse flow impedance times unit length.

The characteristic flow impedance, Z_{0h}, and the propagation constant, γ_h, are given by,

$$Z_{0h} = \sqrt{Z_{lh} Z_{th}} \tag{2.28}$$

$$\gamma_h = \sqrt{\frac{Z_{lh}}{Z_{th}}} \tag{2.29}$$

For sinusoidal flow the various impedances and the propagation constant are:

$$Z_{lh} = R'_h + j\omega L'_h \tag{2.30}$$

$$Z_{th} = \frac{1}{G'_h + j\omega C'_h} \tag{2.31}$$

$$Z_{0h} = \sqrt{\frac{R'_h + j\omega L'_h}{G'_h + j\omega C'_h}} \tag{2.32}$$

$$\gamma_h = \sqrt{\left(R'_h + j\omega L'_h\right)\left(G'_h + j\omega C'_h\right)} \tag{2.33}$$

In order to use an electric transmission line to model an artery it is necessary to measure or calculate the characteristics of the transmission line (for example R'_h, G'_h, L'_h and C'_h). Normally, it is very difficult to measure directly (in an artery) the characteristics used in the previous equations and they are usually calculated from some physical characteristics less difficult to measure, such as the Young's modulus, the length and the diameter of the artery.

Various electrical models for blood flow in the entire arterial system or in regional parts of it based on the above equations were developed in the past [Avolio 1980, de Pater & van den Berg 1964, McIlroy et al. 1986, Mo et al. 1988, Raines et al. 1974, Snyder et al. 1968, Westerhof et al. 1969] to allow the study of the arterial system.

2.3 Doppler ultrasound

The frequency seen by an observer moving in relation to a wave source is different from the frequency of the emitted wave. This simple but important phenomenon is known as the Doppler effect after the Austrian physicist Johanes Christian Doppler (1803-1853).

Ultrasound has been extensively used since the fifties to visualise the interior of the human body. Since the work of Satomura [1957] ultrasonic waves in conjunction with the Doppler effect have been used to monitor moving structures within the body, for example foetal movement or blood flow.

The Doppler ultrasound instrument transmits an ultrasonic beam into the body at a certain frequency. The ultrasonic wave is reflected/scattered in the body and if the reflector/scatterer is moving in relation to the ultrasonic transducer the frequency of the received wave is different from that of the emitted one. The frequency difference (Doppler frequency shift) is proportional to the relative velocity between the reflector/scatterer and the ultrasonic transducer.

In this section we describe the basics of Doppler ultrasound physics, some Doppler ultrasound instruments and models for the Doppler signal backscattered from moving blood.

2.3.1 Ultrasound

A sound wave consists of a mechanical disturbance propagating through a medium, unlike the electromagnetic waves (e.g., light and radio waves) that even propagate in the absence of matter (*vacuum*). Although the sound needs matter to propagate, the matter itself does not travel from one point to another, only the mechanical perturbation.

Ultrasound is the sound whose frequency is so high that cannot be heard by an human being (> 20 kHz).

The ultrasonic frequencies used in medical applications of ultrasound are in the 1–20 MHz range [Fish 1990]. The speed of sound propagation depends on the compressibility and density of the medium; usually different media have different propagation speeds. In soft tissues the speed of sound varies slightly but clusters around 1540 $\mathrm{m\,s^{-1}}$ [Bamber 1986].

2.3.2 The Doppler effect

As already mentioned, when a wave source and an observer are moving in relation to each other the wave frequency measured by the observer is different from that emitted by the source.

In medical applications of Doppler ultrasound the source (transmitting transducer) and the final observer (receiving transducer) are stationary. It is the movement of any reflector or scatterer in the path of the ultrasonic radiation that produces the Doppler frequency shift.

Any reflector or scatterer in the path of the radiation acts both as an observer and a source of ultrasonic waves. The reflector acts as an observer when it is picking up the ultrasonic wave emitted by the transmitter and acts as a source when it reradiates the ultrasonic wave.

Figure 2.9 shows diagrammatically the beam/scatterer arrangement.

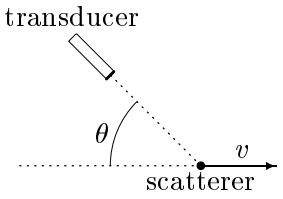

Figure 2.9: Arrangement of ultrasonic beam and scatterer movement for systems with a single transducer.

The apparent frequency of the ultrasonic wave received by the scatterer, f_{rs}, is:

$$f_{rs} = \frac{c - v\cos(\theta)}{c} f_0 \tag{2.34}$$

where f_0 is the frequency of the transmitted wave and c is the speed of propagation of the radiation, v is the velocity of the scatterer (considered positive when the scatterer is moving away from the transducer) and θ is the angle between the ultrasonic beam axis and the direction of the scatterer movement. The scatterer reradiates the ultrasonic wave and the transducer receives a wave whose frequency is:

$$\begin{aligned} f_r &= \frac{c}{c + v\cos(\theta)} f_{rs} \\ &= \frac{c - v\cos(\theta)}{c} \times \frac{c}{c + v\cos(\theta)} f_0 \\ &= \left(1 - \frac{2v\cos(\theta)}{c + v\cos(\theta)}\right) f_0 \end{aligned} \tag{2.35}$$

and the Doppler frequency shift is:

$$f_d = f_r - f_0 = -\frac{2v\cos(\theta)}{c + v\cos(\theta)} f_0 \tag{2.36}$$

In medical Doppler ultrasonic applications $v \ll c$ and the previous expression can be approximated by:

$$f_d = -\frac{2v\cos(\theta)}{c} f_0 \tag{2.37}$$

which is usually referred as the Doppler equation. The minus sign in (2.37) reflects the convention that when the scatterer is moving away from the transducer the velocity is positive and the frequency is reduced.

Continuous wave systems have separate transducers for transmitting and receiving the ultrasound, thus a small correction must be introduced into (2.37) to account for the different angles between the transducers and the scatterer movement [Fish 1986]. The corrected

equation is:

$$f_d = -\frac{2v\cos(\theta)\cos(\delta/2)}{c} f_0 \tag{2.38}$$

where δ is the angle between the transmitter and receiver beams and θ is, in this case, the angle between the bisector of the transmitter and receiver beams and the direction of scatterer movement. Often $\delta/2$ is small so that $\cos(\delta/2) \approx 1$ and equation (2.37) can still be used.

2.3.3 Doppler ultrasound instruments

Doppler ultrasound instruments are usually used in conjunction with ultrasonic scanners so that the position of the range cell is known. Hence we start this sub-section by describing ultrasonic scanners. Then we describe continuous wave instruments, pulsed wave systems, flow direction discrimination techniques and colour flow imaging.

Ultrasonic scanners

When an ultrasound beam passes from one medium to another (e. g., from soft tissue to bone) part of the radiation passes through the boundary and the remaining radiation is reflected back. The degree of reflection depends on the acoustic impedance mismatch between the two media and on the angle of attack. The acoustic impedance is the ratio between the acoustic pressure and the medium velocity [Morse & Ingard 1986, p. 259]. For fluids and soft mediums like tissue the acoustic impedance depends on the density and compressibility of the medium.

Several types of ultrasonic scanners were developed in the past to visualise the interior of the body. Usually, the instrument sends an ultrasonic pulse into the body and measures the time delays of the reflections from the various interfaces in the wave's path.

The earliest and simplest ultrasonic scanner is the A-mode scanner in which the ultrasonic beam is directed into the body along a single path. The echoes received from the tissue boundaries along the beam path are displayed against time. The position of each echo is determined by the corresponding time delay that is proportional to the depth of the reflecting interface. The echoes are displayed with an height determined by the strength (amplitude) of the received signal. The structure and physical composition of the various interfaces and the attenuation of beam along its path determine the amplitude of the received echo.

Since the A-mode scanner investigates a single beam path it can only generate a one-dimensional representation of the signal amplitude versus depth.

A more complex system capable of generating two-dimensional images is the B-mode scanner. The transducer is moved by hand along a scan plane and several beam paths are investigated to calculate a single image. The time delays, the amplitude of the received echoes and the position of the beam for the various scans are all combined together to calculate a two-dimensional static image. The brightness of each pixel is determined by amplitude of the echo signal corresponding to the position in the image.

Major progress on transducer technology, electronics and computers allowed the development of real-time scanners capable of displaying 'moving' images in real-time. The real-time scanners have almost totally replaced the static B-mode scanners. The ultrasonic beam of the real-time scanners is rapidly swept, either mechanically or electronically, through the imaging plane and several images are computed and displayed sequentially so that the resulting image appears flicker free.

When investigating blood flow in the circulatory system real-time scanners are frequently combined with Doppler instruments. This arrangement allows the simultaneous visualisation of the blood vessel anatomy and the blood velocity waveform (usually as a sonogram). If a pulsed wave Doppler system is used the operator can even accurately control the position of the sample volume in the vessel. The instrument incorporating a real-time scanner and a Doppler system is commonly known as a Duplex scanner and an example of its output is shown in figure 2.10.

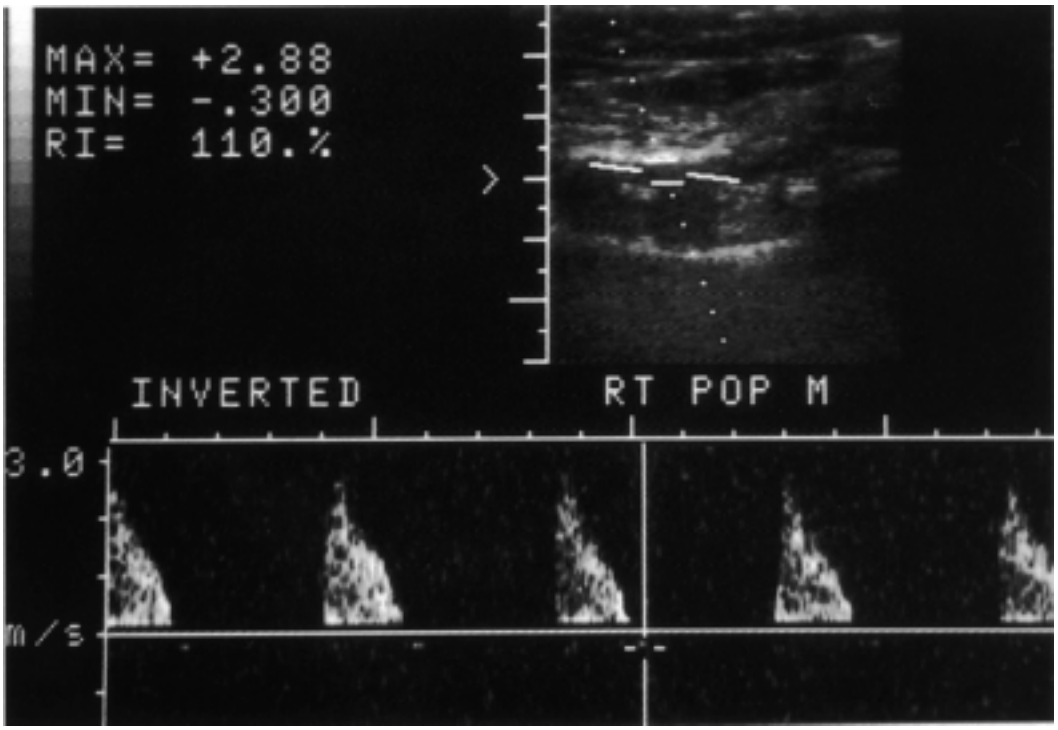

Figure 2.10: Example of the output image of a Duplex scanner from a popliteal artery with a 70% stenosis (from [Polak 1995]). Top right is a longitudinal image of the vessel and surrounding tissue. The dotted line indicates the ultrasound beam axis, the two solid lines crossing this the extent of the sample volume and the remaining solid lines the vessel axis markers. The spectrogram of the Doppler signal is displayed at the bottom of the figure.

The Duplex scanner was further improved by superimposing a colour coded image of the blood flow onto the greyscale image of the real-time scanner in what is known as colour flow imaging.

Continuous wave systems

The continuous wave (CW) Doppler instrument was introduced by Satomura [1957] to investigate blood flow.

Figure 2.11 shows a block diagram of a simple CW Doppler device. The CW instrument has two distinct transducers: the transmitter (T) continuously emitting ultrasonic radiation and the receiver (R) continuously picking up the ultrasonic radiation reflected or scattered from tissue. Usually the two crystals are mounted in the same probe with a slight inward tilt so that their beams overlap. The region in which the two beams overlap is usually called the sample volume.

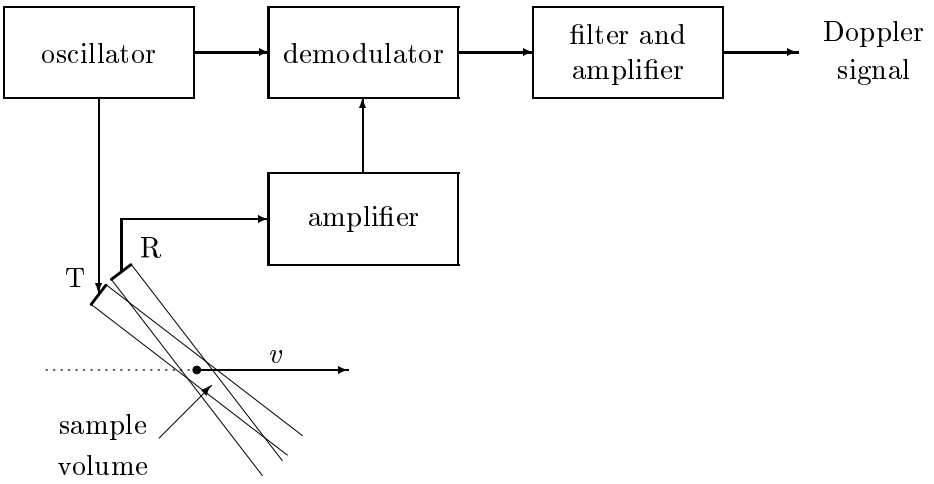

Figure 2.11: Continuous wave Doppler instrument (adapted from [Fish 1990]).

The signal picked up by the receiver is first amplified and then multiplied in the demodulator by a reference signal from the oscillator. The demodulator output signal contains both the sum and the difference frequencies of the two input signals. In order to isolate the difference frequency, the Doppler frequency shift, the demodulator's output is low-pass filtered.

The receiver transducer collects not only the radiation backscattered by the red blood cells but also the radiation reflected back by tissue interfaces along the beam path, such as blood vessel walls. The amplitude of the reflected radiation is, usually, much stronger than that of the backscattered radiation. Thus, the signal must be high-pass filtered so that the strong signal arising from the wall reflection is rejected. This high-pass filter is usually referred as the 'wall thump' filter (see for example [Kremkau 1995]). The downside of using the 'wall thump' filter is that the signal backscattered by the slow moving red blood cells is also removed from the output signal. This may be critical in some application like the assessment of blood flow in small peripheral vessels and the investigation of blood flow near

the wall of larger vessels.

The simple CW device presented in figure 2.11 is not capable of discriminating the direction of the flow, that is to say that the output from flow moving towards the transducer is indistinguishable from flow moving away from the transducer. Flow discrimination techniques used in Doppler instruments will be described latter (see page 29).

Pulsed wave systems

The major limitation of the CW instrument is its lack of range resolution. As a consequence, the CW instrument cannot separate the signals from any two vessels crossed by the beam and cannot be used to examine the blood flow at different parts of a vessel. For these reasons the CW instrument is not suitable for examining deep structures like the heart nor vascular organs as the brain [Evans et al. 1989].

Pulsed wave (PW) systems overcome the range resolution limitation by controlling the distance from which the backscattered radiation is received. Pulsed wave systems use a single transducer to transmit and receive the ultrasonic radiation. The transducer emits, at regular intervals, short bursts of ultrasound, after a certain time delay the receiver gate opens and the received signal from the selected region of the beam, (called the sample volume) is processed.

The time delay between the transmission and reception determines the distance between the transducer and the sample volume and the duration of the transmission interval and of the reception interval determine its axial length. The width of the sample volume corresponds to the width of the ultrasonic beam at the depth being investigated. The operator can adjust the position of the sample volume and its axial length by changing the parameters controlling the operation of the gates.

Figure 2.12 presents the block diagram of a PW instrument with no flow direction discrimination. The timing circuits control the opening and closure of the transmitter and receiver gates.

The added versatility of the PW instruments comes at a price, the instruments are more complex than the CW ones and also have other limitations. For each pulse repetition frequency (PRF) there is a maximum frequency shift that can be unambiguously detected $f_{d_{\max}} = \mathrm{PRF}/2$ (the Nyquist limit). As the depth of interest increases the maximum PRF that can be used decreases to allow for the ultrasound burst to travel the longer distance and return. Since the PRF decreases the maximum detectable velocity also decreases. For a given depth of interest and for a constant angle of attack the maximum detectable velocity decreases as the transmitted frequency increases. As an example, a 5 MHz transducer with an angle of attack of 0^{o} can detect velocities up to $1.2\ \mathrm{m\,s^{-1}}$ at a depth of 5 cm and only up to $0.6\ \mathrm{m\,s^{-1}}$ at a depth of 10 cm, for a 10 MHz with the same angle of attack and at the same depths the maximum detectable velocities are half those for the 5 MHz transducer (values tabulated by Hedrick et al. [1995]).

As in any sampling system, if the sampling rate of the PW system is not adequate for the frequencies being measured, aliasing occurs and the frequencies above the Nyquist limit

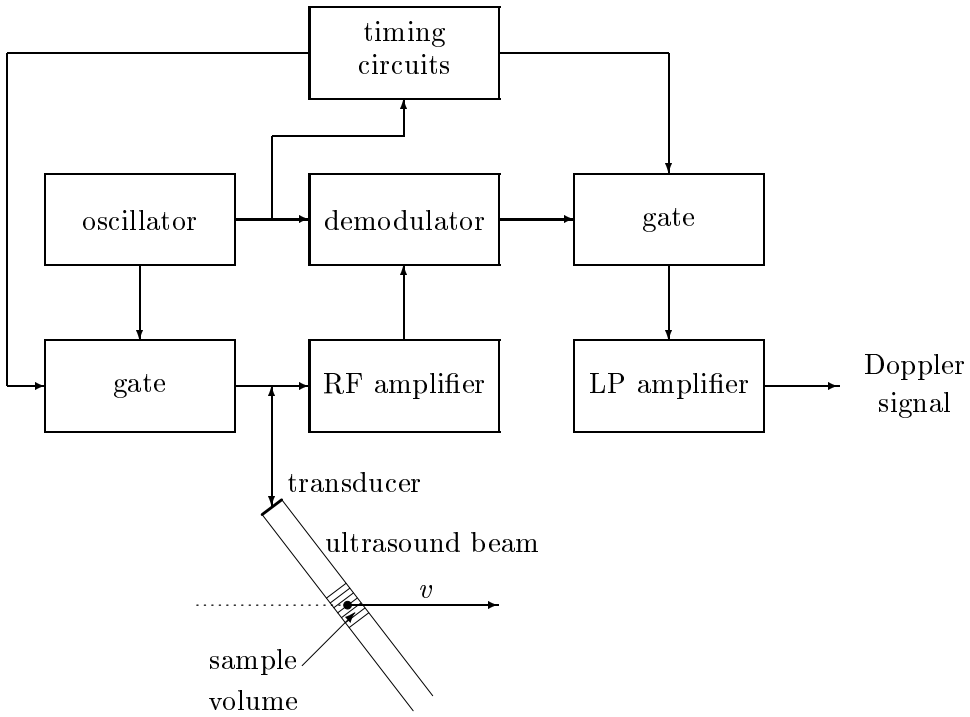

Figure 2.12: Pulsed wave Doppler instrument (adapted from [Fish 1990]).

are represented as low frequencies.

Although the PW instrument shown in figure 2.12 has a single channel, it is possible to replicate the demodulator and gate blocks so that several sample volumes are simultaneously investigated in parallel. One of the uses of multi-channel PW systems is to evaluate blood velocity profiles.

Since the Doppler signal spectrum varies with time following the cardiac cycle, it is usually displayed as a sonogram, also called a spectrogram, where the horizontal axis represents time, the vertical axis represents frequency and the intensity of the greyscale plot is related to the power of the spectrum. An example of a sonogram is shown in figure 2.13.

Flow direction discrimination

The CW and PW instruments presented previously (figures 2.11 and 2.12) are not capable of differentiating between forward and reverse flow. Three techniques have been used to permit flow direction detection: single sideband detection, heterodyne detection and quadrature phase detection.

Single sideband detection consists on separately filtering the frequencies above and below the frequency of the reference signal. The received signal is split into two branches; one of the

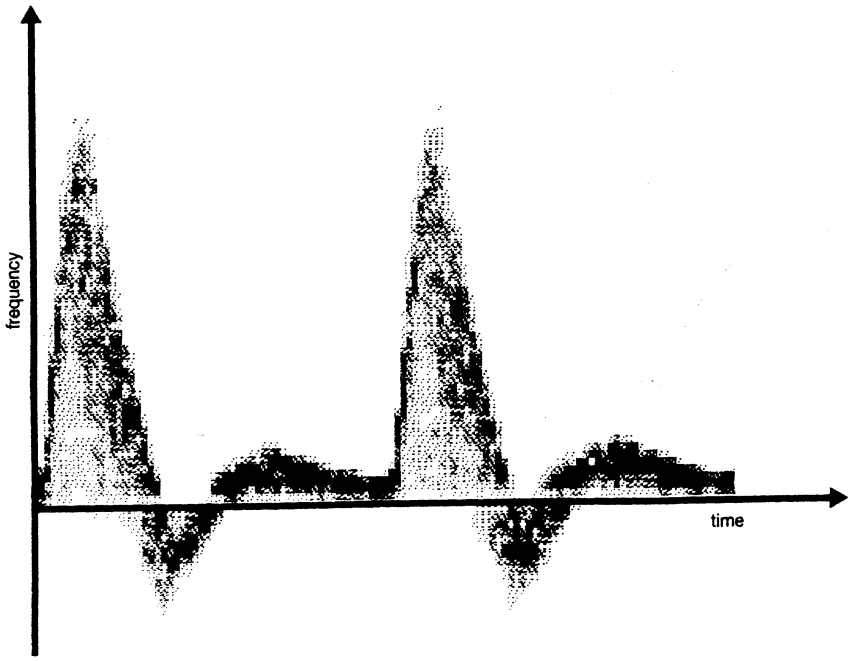

Figure 2.13: Sonogram of the Doppler signal from a common femoral artery (from [Evans et al. 1989]).

branches is high-pass filtered with the cut-off frequency set to the frequency of the oscillator while the other is low-pass filtered with the same cut-off frequency. Both signals are then mixed with the reference signal and low-pass filtered. The signal from one of the branches corresponds to the forward flow and the other to the reverse flow. The major problem with this flow direction detection method is the need for extremely sharp sideband filters which makes it inapplicable for pulsed systems due to the long ringing time of the sharp filters.

Another method used for flow direction discrimination, the heterodyne detection, mixes the received signal with a reference signal whose frequency has an offset in relation to the oscillator frequency. The demodulated signal is low-pass filtered in the usual way. The positive frequency shifts, corresponding to forward flow (towards the transducer), are represented above the offset frequency while the negative frequency shifts, corresponding to reverse flow, are represented below the offset frequency.

Quadrature phase detection is the most commonly used method for flow direction discrimination. Figure 2.14 illustrates the quadrature phase method for a CW instrument. The same principle applies to PW instruments.

After amplification the received signal is split into two channels to be demodulated with two reference signals with quadrature phases. The in-phase channel is mixed with the oscillator signal while the in-quadrature channel is mixed with the oscillator signal 90^{o} phase shifted.

The two output channels have a phase difference of $+90^{o}$ or -90^{o}. The sign of the phase

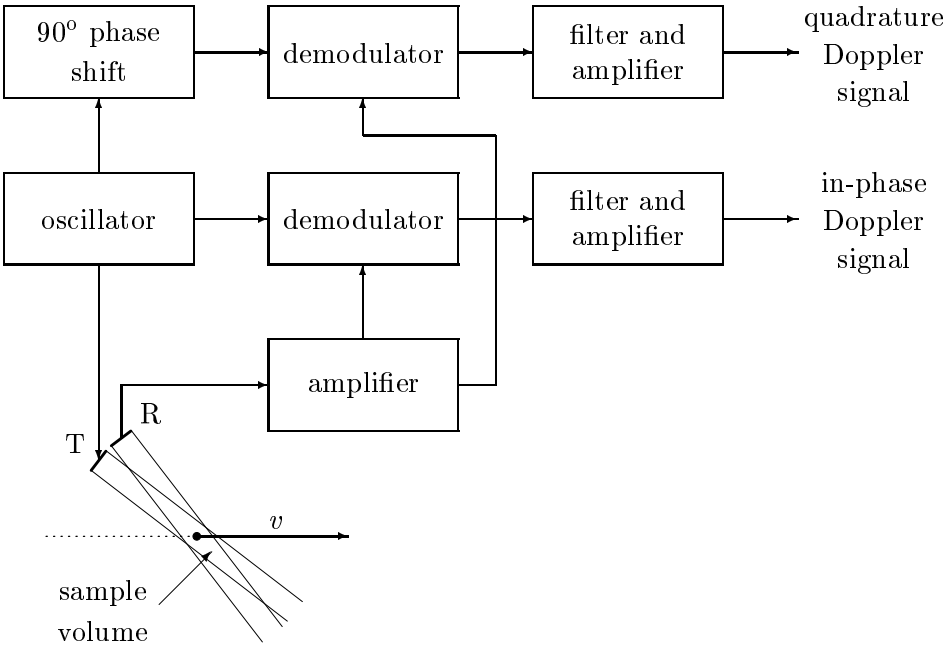

Figure 2.14: In phase and quadrature flow direction discrimination for a continuous wave Doppler instrument (adapted from [Fish 1990]).

difference is determined by the direction of flow and can be detected by a phase detector circuit.

Colour flow imaging

Real-time colour flow imaging instruments allow the simultaneous visualisation of anatomical structure and blood flow as a colour-coded image. Usually forward flow is represented with shades of red, reverse flow shades of blue and turbulent flow with green.

Velocity information is obtained from a large number of sample volumes to calculate the flow image. For each sample volume position the beam must stay stationary for a number of transmitted pulses in order to estimate the mean velocity (typically 10 pulses). The methods to estimate the velocity have to be very fast so that an acceptable frame rate is obtainable. The most frequently used velocity estimation methods are the autocorrelation method [Kasai et al. 1985], which measures the phase shift between successive echo signals, and time-domain methods (for example, [Bonnefous & Pesqué 1986]), which use the cross-correlation between the echoes following successive transmitted pulsed to track the movement of the scatterers.

Recently two new techniques for imaging the blood flow have emerged: pwer imaging [Rubin et al. 1994] and harmonic imaging [Chang et al. 1995]. Power imaging uses the power of the backscattered signal instead of the Doppler frequency shift. In harmonic imaging

encapsulated bubble contrast agents are injected into the circulation to increase the power of the backscattered signal. The second harmonic of the backscattered signal is then used to generate the image. With this method much slower flow can be detected than with conventional methods. The power of the second harmonic of the signal backscattered from tissue is much lower than the power from the signal coming from the contrast agent.

A more detailed description of medical ultrasound instruments can be found in several textbooks, for example [Evans et al. 1989, Fish 1990, Hedrick et al. 1995, Jensen 1996, Kremkau 1995, Meire & Farrant 1995, Taylor et al. 1995].

2.3.4 The Doppler spectrum

The Doppler equation (2.37) is only valid for a single scatterer passing through an infinitely wide and uniform ultrasonic field.

Doppler ultrasound instruments do not meet these conditions when investigating blood flow; blood contains a large number of particles (with various velocities) in suspension in the plasma and the ultrasonic fields produced by real systems are neither infinitely wide nor uniform. As a consequence, the Doppler signal contains a range of frequencies, a spectrum, rather than a single frequency.

Ideally, it should be possible to directly relate the frequency content of the Doppler spectrum with the distribution of the velocities of the scatterers passing through the sample volume. In fact, external factors like the characteristics of the ultrasonic field, the shape and size of the sample volume and the spectral estimation technique used to compute the spectrum alter the measured Doppler spectrum. These alterations result in a widening (broadening) of the Doppler spectrum and are commonly referred as spectral broadening.

The next sections describe the relation between the Doppler spectrum and the velocity distribution of the red blood cells together with the various sources of spectral broadening.

Scattering of ultrasound from blood

As mentioned in section 2.2.1 the major particles in blood are erythrocytes (red blood cells), leukocytes (white blood cells) and platelets. The dimensions, concentration and other physical properties of these particles affect the way in which they scatter ultrasound. Table 2.1 presents some of the characteristics of the blood particles.

There are many more red blood cells than white blood cells and the volume of red blood cells is much larger than that of platelets. Thus, it is generally accepted that the scattering of ultrasound by blood is mainly due to the red blood cells [Shung et al. 1976].

For medical applications of ultrasound, the diameter of the erythrocytes is much smaller than the wavelength of the ultrasonic radiation. At low concentrations the erythrocytes act as a random distribution of independent point targets, this type of scattering is know as Rayleigh scattering after Lord Rayleigh's [1872] work.

In normal human whole blood the hematocrit (fraction of blood volume occupied by cells)

	Concentration (particles/mm^3)	Dimensions (μm)	% total blood volume
Erythrocytes	5×10^6	7.2×2.2	45
Leukocytes	8×10^3	$9 - 25$	~ 0.8
Platelets	2.5×10^5	$2 - 3$	~ 0.2

Table 2.1: The dimensions and concentration of the major particles in normal human blood (from [Evans et al. 1989, p. 117]).

is around 0.45. At this high concentration the distance between two red blood cells is only about 10% of its diameter and the positions of the particles are no longer independent from one another [Shung et al. 1976] and the backscattered power is less than would be produced by an ensemble of independent particles.

The effect of hematocrit on backscattering of ultrasound from blood was studied by Shung and associates [Shung et al. 1976, Shung 1982] and they observed that the peak of backscattering occurred for an hematocrit between 20 and 30 percent. The same group also studied the effect of flow disturbance [Shung et al. 1984, Shung et al. 1992], shear rate [Shung et al. 1992, Yuan & Shung 1988*a*] and fibrinogen concentration [Yuan & Shung 1988*b*] on the backscattering of ultrasound from blood. They observed that flow disturbance, low shear-rate and increased fibrinogen concentration increase the power of the backscattered ultrasound signal. Cloutier & Shung [1993] found that the Doppler power changes cyclically with the cardiac cycle for high hematocrit, large velocities and in the presence of turbulence. The authors suggested that the cyclic power variation might be associated with changes in the correlation among particles induced by the turbulence. Bascom & Cobbold [1995, 1996] proposed a model that uses the spatial variation of a packing factor to explain the changes in the backscattered Doppler power with flow conditions.

Aggregation of red blood cells to form rouleaux occurs specially at low shear rates with high fibrinogen concentration and is probably another process that affects the ultrasonic backscatter from blood [Shung & Thieme 1993*a*, Yuan & Shung 1988*b*]. Cloutier et al. [1996] used the variations in the Doppler power to study the dynamics of red blood cell aggregation in porcine whole blood and concluded that their method is sensitive to the presence of red blood cell aggregation for shear rates below 10 s^{-1}.

A different approach to describe the scattering of ultrasound from blood is to treat the blood as an isotropic continuum and to consider that scattering arises from local fluctuations in the compressibility and mass density of the continuum [Angelsen 1980].

Velocity profile and beam pattern

The velocity field, the size of the sample volume and the pattern of the beam sensitivity have a strong influence on the shape of the Doppler spectrum. If spectral broadening effects are

neglected, the range of frequencies contained in the Doppler spectrum corresponds directly to the range of velocities passing through the sample volume. Under uniform insonation conditions, the total power in any frequency interval is proportional to the volume occupied by the particles with velocities in the corresponding range[Evans et al. 1989, p. 115].

It is possible to compute the theoretical Doppler spectrum for some simple velocity profiles and sample volume shapes. For example, for a uniform beam wider than the vessel and a velocity profile obeying a power law, $v(r) = v_0[1 - (r/R_0)^n]$, it is easy to compute the expected Doppler spectrum (see section 5.2.1); $v(r)$ represents the velocity of the streamline at distance r from the centre of the vessel, v_0 is the velocity at the centre of the vessel, R_0 is the vessel radius and n is a parameter that controls the flatness of the velocity profile. Figure 2.15 shows the Doppler power spectrum for three velocity profiles under an uniform wide ultrasonic beam.

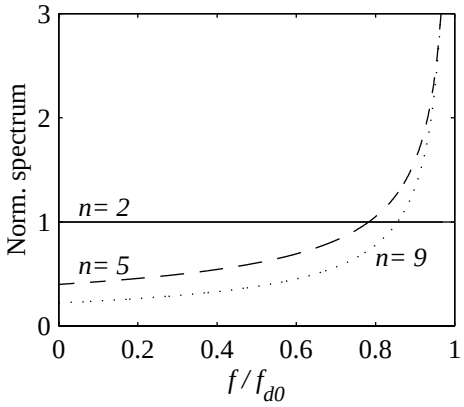

Figure 2.15: Theoretical Doppler power spectrum [Fish 1986] for a wide uniform ultrasonic beam insonating a vessel with a power law velocity profile $v(r) = v_0[1 - (r/R_0)^n]$; v_0 is the velocity at the centre of the vessel and f_{d0} is the corresponding Doppler frequency shift.

Several authors have studied the influence of velocity profile, sample volume shape and size on the Doppler spectrum shape. Evans [1982*b*] developed a theoretical model to predict the effect of ultrasonic beam width on some frequency processors for rectangular beams centred in vessels with parabolic and plug flow. He later extended his model [Evans 1985] to non-centred beams. Cobbold et al. [1983] used a computational model to calculate the Doppler spectrum for continuous wave systems using uniform and Gaussian beams, allowing for tissue attenuation and improper alignment of the beam and vessel. Their work was latter extended to include intrinsic spectral broadening (due to beam shape) by using a geometric approach. They derived closed form expressions for the spectrum in the cases of a uniform circular beam of equal radius to the vessel centred on the vessel [Bascom et al. 1986] and a centred Gaussian beam [Bascom & Cobbold 1990].

Fish [1986] presented a theoretical study, based on previous work by Angelsen [1980], of the origins of the Doppler spectrum for continuous wave and pulsed wave systems relating

the spectral shape to sample volume sensitivity variation in the general case and allowing for non-plane wave conditions. Censor et al. [1988] related the Doppler spectrum maximum frequency to transducer geometry in the case of far-field insonation for long strip, rectangular and circular transducers. Aldis & Thompson [1992] derived expressions for the Doppler ultrasound spectral power density for continuous wave systems showing that, for axisymmetric flow, these could be reduced to expressions involving single integrals—elliptic integrals for uniform circular beams, and Bessel functions for Gaussian beams.

Spectral broadening

Of particular interest is the width of the spectrum since this influences the sensitivity of flow disturbance detection and mean velocity estimation. Several measures of spectral width can be used in the Doppler spectrum: -3 dB frequency, root mean square (rms) width, etc.

In this work we use the rms width, σ, defined by,

$$\sigma = \frac{1}{2\pi}\sqrt{\frac{\int_{-\infty}^{\infty}(\omega-\overline{\omega})^2\,S(\omega)\,d\omega}{\int_{-\infty}^{\infty}S(\omega)\,d\omega}} \tag{2.39}$$

since this measure potentially allows correction for two spectral broadening mechanisms, window and non-stationarity broadening [Wang & Fish 1997]; ω is the angular frequency and $\overline{\omega}$ is the mean angular frequency of the Doppler power spectrum $S(\omega)$.

It should be noted that the perceived width from a spectrogram will in general be larger since this represents the width between spectral "edges" determined by the spectral estimator word length, display monitor settings and any compression used.

Unfortunately the Doppler spectral width is not entirely determined by the blood velocity field and the scattering characteristics of blood. Other factors like the finite dimensions of the sample volume, the variation of the velocity field during the time of observation and the spectral estimation technique used to estimate the spectrum contribute to broaden the measured spectrum. Detailed descriptions of some sources of error and spectral broadening that affect the Doppler ultrasound signal can be found in [Gill 1985, Hoeks et al. 1991, Jones 1993]. The effects of the various types of spectral broadening are illustrated in figure 2.16 and are briefly described below.

The finite dimensions of the ultrasonic transducer and the finite pulse duration result in a spreading of the Doppler spectrum known as intrinsic spectral broadening. This type of spectral broadening is due to the properties of the measurement system rather than the properties of the system being measured [Evans et al. 1989].

The intrinsic spectral broadening occurs even for a single scatterer and can be explained in two different ways. Either in terms of the range of angles subtended by the scatterer as it crosses the beam (geometric broadening) or in terms of the amplitude modulation of the

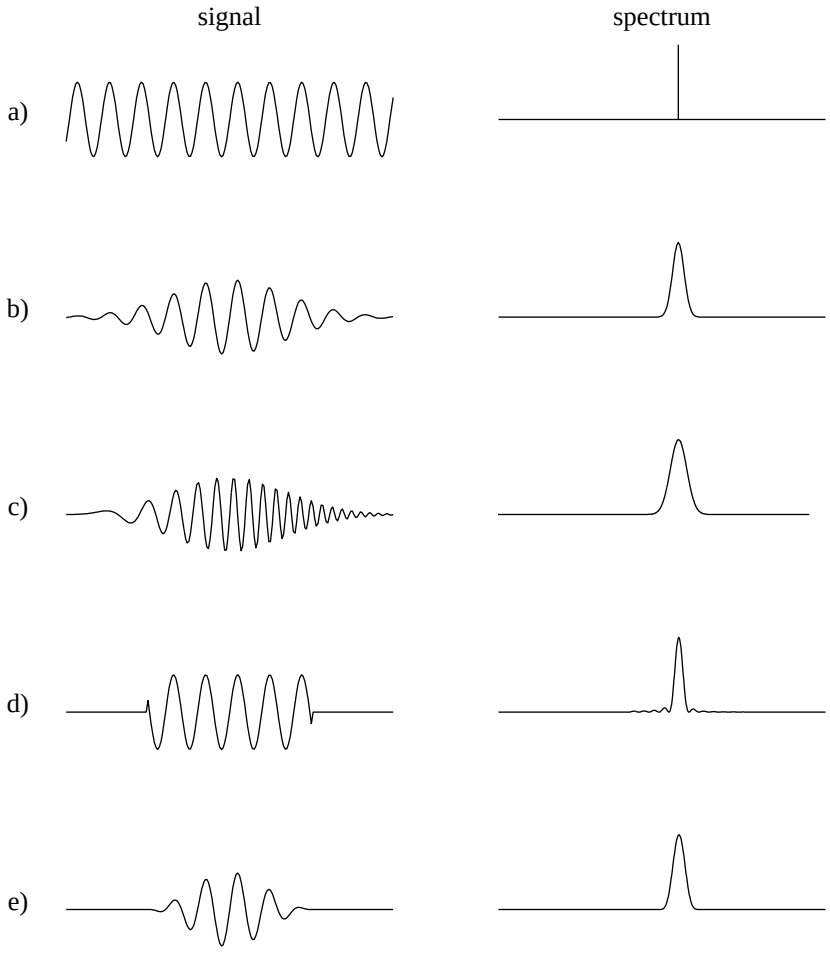

Figure 2.16: Illustration of various spectral broadening effects: a) ideal case of infinite wide uniform beam; b) transit time broadening due to the finite size of the sample volume; c) nonstationarity broadening due to variation of scatter's velocity during its passage through the sample volume; d) window broadening due to the finite time window (boxcar); and e) window broadening with reduction of spectral leakage by using a smooth tapered window (Hanning).

backscattered radiation due to the finite transit time taken by the scatterer to cross the beam (transit time broadening).

Green [1964] was the first to identify spectral spreading effects not related with the blood velocity field. Latter Griffith et al. [1976] and Newhouse et al. [1976] studied transit time broadening and Newhouse et al. [1977] studied geometrical broadening. Bascom et al. [1986] used the geometrical approach to compute intrinsic spectral broadening for continuous wave systems.

Transit time and geometrical spectral broadening were considered for some time to be two independent effects because the Doppler bandwidth predicted using transit time broadening theory was much smaller than that observed experimentally for flow in the near field of

the transducers. Under the same circumstances the bandwidth predicted with geometric broadening theory agreed well with the experimental values [Newhouse et al. 1977]. Latter Newhouse et al. [1980] showed that transit time broadening and geometrical broadening are equivalent, the previous transit time calculations were erroneous because they did not take into account the complex beam pattern in the near field. The equivalence between geometric and transit time broadening had already been established previously in the Doppler laser field [Angus et al. 1971, Edwards et al. 1971].

Cloutier et al. [1993] evaluated experimentally the effect of intrinsic spectral broadening on the Doppler spectrum using porcine whole blood in a pulsatile flow model. They observed that the relative Doppler bandwidth is independent of flow velocity for steady flow. This was previously verified by Tortoli et al. [1992] using a string phantom. Both works demonstrated experimentally a theoretical proposition of Newhouse & Reid [1990] stating that the relative bandwidth of the Doppler spectrum does not depend on the lateral displacement in the far field of an unfocused transducer or near the focal plane of a focused transducer. Willink & Evans [1996] studied the effect of intrinsic spectral broadening, using a geometrical approach, on the estimation of the mean blood velocity.

When estimating the Doppler power spectrum only the signal between two time instants (time window) is used. As a consequence, the spectral estimate is broadened (window broadening) because it results from the convolution of the Doppler power spectrum with the energy spectrum of the time window [Fish 1991]. Spectral estimation techniques that require a stationary signal like those based on the Fourier Transform are more sensitive to window broadening than those developed specifically for nonstationary signals.

The acceleration and deceleration of the blood during the cardiac cycle give rise to the variation of the mean Doppler frequency. The mean frequency variation causes spectral broadening in the Doppler spectrum usually known as nonstationary (or nonstationarity) spectral broadening. This type of spectral broadening occurs whenever the spectral estimation technique, for example the short time Fourier transform, divides the Doppler signal into segments to compute the frequency spectrum and the signal is not stationary during the duration of the segment. The measured spectrum is an average of the signal's frequency content for the duration of the data segment.

Several authors have studied nonstationary broadening. Kikkawa et al. [1987] analysed the effect of blood acceleration on the bandwidth of the Doppler spectrum obtained from the ascending aorta of the dog. They concluded that during the accelerative and decelerative phases of the cardiac cycle the bandwidth is significantly higher than that predicted for steady flow. Fish [1991] studied the influence of mean frequency variation and data segment duration on the bandwidth of the Doppler spectrum. He concluded that for each rate of frequency variation exists a segment duration that giving maximal spectral resolution. In an experimental study Cloutier et al. [1993] verified that the Doppler spectrum from pulsatile

flow is broader during acceleration and deceleration of blood.

Since reducing the influence of spectral broadening on the Doppler bandwidth is important to allow the detection of lower levels of flow disturbance, Fish and co-workers have developed methods to reduce/remove nonstationary broadening from the Doppler spectrum[Bastos 1990, Cardoso et al. 1996, Wang & Fish 1997].

2.3.5 Models for the Doppler signal backscattered from moving blood

Since the early seventies, several models of the process leading to the generation of simulated Doppler ultrasound signals have been developed and have contributed significantly to improve our understanding of the Doppler signal. Routh et al. [1989] say that "Mathematical and physical models are essential tools in both fundamental and clinical applied Doppler ultrasound research".

The randomness of the Doppler signal and the variability of physiological characteristics among human subjects makes the study of *in vivo* Doppler signals under controlled conditions almost impossible. Models allow the study, under controlled conditions, of the influence of various factors on the characteristics of the signal.

Several classification schemes can be used to classify Doppler ultrasound signal models. In this text we divide the Doppler models into: physical models, those that use the movement of physical particles to mimic the flow of red blood cells; and mathematical models, those that use mathematics to describe the characteristics of the Doppler signal. The mathematical models are sometimes used to generate simulated Doppler signals with electronic circuits or computer software.

Typically physical models have been used to measure and/or study the characteristics of the Doppler signal at an experimental level and as test objects to calibrate Doppler systems; physical models are also useful in the validation of mathematical models. Mathematical models are used mainly to express quantitatively our current knowledge of the Doppler process and the generation and interpretation of Doppler signals. Mathematical models are also used to generate simulated Doppler signals with known characteristics that can then be used in the development of new tools for interpreting Doppler ultrasound signals or for evaluating the performance of existing tools.

In this section we describe some of the models for the Doppler ultrasound signal as well as computer simulators that produce signals whose characteristics are similar to those of clinically obtained Doppler signals. Our literature review on Doppler ultrasound models does not pretend to be all-inclusive but simply to illustrate the various types of models and simulators for the Doppler signal with particular emphasis on those models from which our model evolved (see chapter 4).

Physical models

At least two types of physical models have been used in Doppler ultrasound: flow rigs and moving string phantoms. Figure 2.17 shows an example of a flow test-rig used to simulate Doppler signals from steady flow.

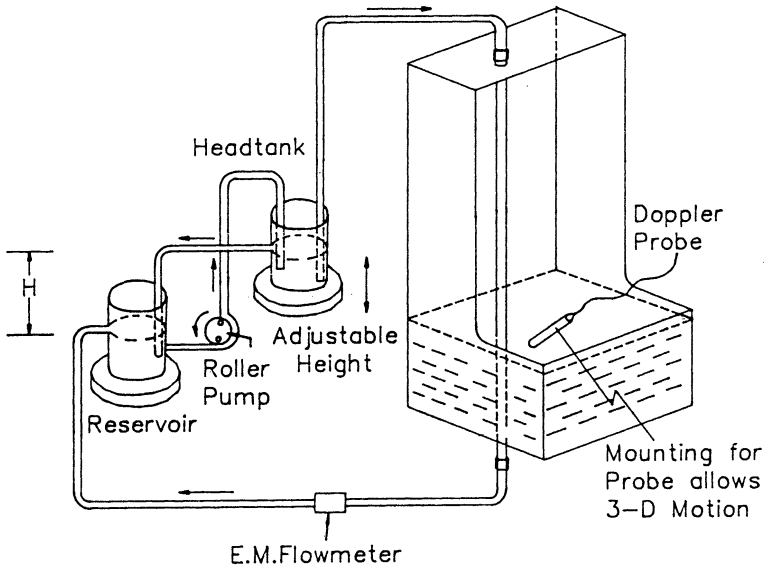

Figure 2.17: Physical flow model for steady flow, the height between the two tanks controls the volumetric flow in the tube circuit (taken from [Law et al. 1989]).

The incorporation of a pulsatile pump [Law et al. 1987, McCarty & Locke 1986] or a pulsatile valve [Wendling 1991] in the tube circuit of figure 2.17 can transform the model into a pulsatile flow model.

Examples of applications of flow test-rigs in Doppler ultrasound are: the study of scattering characteristics of blood [Shung et al. 1992]; study the effects of sample volume size and position on the Doppler spectrum [Law et al. 1991]; calibration of Doppler flowmeter [McCarty & Locke 1986]; validation of a mathematical model [Wendling 1991].

Moving string phantoms consist basically on a motor-driven continuous loop of string (or thread) immersed in a water bath. Examples of practical applications are quality assurance of Doppler systems [Russell et al. 1993, Lange & Loupas 1996] and test signal processing techniques [Hoskins 1996, Tortoli et al. 1994],.

One advantage of moving string phantoms is their ability to simulate the signal from a single velocity streamline. This allows studies where knowing the trajectory of the scatterers along the sample volume is important like the one by Tortoli et al. [1992] to experimentally prove the Doppler bandwidth invariance theorem [Newhouse & Reid 1990].

Mathematical models

Several theoretical models of the physics of the generation of the Doppler ultrasound signal have been published.

Brody & Meindl [1974] considered the red blood cells as independent random positioned scatterers and derived the Doppler power spectral density for continuous wave systems. Garbini et al. [1982*a*] also assumed scattering from random independent scatterers in their analytical model of the Doppler pulsed wave flowmeter used to study fluid turbulence [Garbini et al. 1982*b*].

In whole blood the distance between red blood cells is about 10% of the cells diameter [Shung et al. 1976]. At these high concentrations the movement of the scatterers is hindered by the presence of other scatterers and their position can no longer be considered independent [Shung et al. 1976], the power backscattered by whole blood is significantly lower than that from independent scatteres. A different approach was used by [Angelsen 1980] who considers that the scattering arises from local fluctuations in the mass density and compressibility of blood. This was previously proposed by Gore & Leeman [1977] for the scattering of ultrasound from human tissue. Fish [1986] extended Angelsen's work to nonplane wave conditions.

None of these theoretical works aimed at producing time series signals but formed the basis for much of the models later developed to generate simulated Doppler signals.

One of the simplest possibilities to generate simulated Doppler signals is to consider the signal to be filtered broadband Gaussian noise. Some examples of the application of this idea to simulate Doppler signals are mentioned below.

Sheldon & Duggen [1987] developed a signal simulator for stationary Doppler signal by filtering broad-band noise with a second order low-pass filter implemented with a switched capacitor integrated circuit. Bastos & Fish [1991] extended this idea to simulate nonstationary Doppler signals by controlling the cut-off frequencies of a band-pass filter with a computer. Kristoffersen & Angelsen [1988] used a FIR (Finite Impulse Response) filter to generate stationary Doppler signals used to fill the gaps in the measured Doppler signal of time-shared B-mode scanners and Doppler systems. Wang & Fish [1996] used a filter with a time-varying impulse response to simulate nonstationary Doppler signals.

Another approach to model the Doppler signal is to first specify the signal characteristics in the frequency domain and then transform it into the time domain. In order to obtain the time signal van Leeuwen et al. [1986] used the inverse fast Fourier transform while Mo & Cobbold [1986] summed a large number of sinusoids with appropriate amplitudes and phases. In the latter model the Doppler signal is expressed as:

$$s(t) = \sum_{m=1}^{M} \sqrt{2P(f_m)\Delta f\, y_m}\cos(2\pi f_m t + \phi_m) \tag{2.40}$$

where y_m are chi-squared random variables with two degrees of freedom, $P(f_m)$ is the power

spectral density of the desired Doppler spectrum (band limited to the interval $[0, f_{max}]$), $\Delta f = f_{max}/M$, $f_m = (m-1/2)\Delta f$ and ϕ_m is uniformly distributed in the interval $[0, 2\pi]$. Mo & Cobbold extended their model to simulate signals from pulsatile flow [Mo & Cobbold 1989] by allowing $P(f_m)$ to be a function of time. Talhami & Kitney [1988] proposed a model consisting of a frequency modulated sine wave,

$$s(t) = A(t)\cos(\phi(t)) \tag{2.41}$$

where $A(t)$ is a stochastic function of time and $\phi(t)$ is the time-variant phase. The signal does not include the random phase that is usually present in Doppler signals.

The above models need a previous knowledge of the Doppler power spectrum and make no attempt to directly relate the simulated signal to the Doppler instrument parameters, the beam pattern or the blood velocity field.

Jones & Giddens [1990] proposed a time domain model for steady flow where the amplitude and phase of the signal are self-correlated random variables obtained by weighting two independent sets of zero mean Gaussian random numbers with a sliding window that is related to the shape of the sample volume. The spectrum of the simulated signal incorporates transit time broadening. A modified version of this model was developed by Wendling et al. [1992] for pulsatile and non-steady flow. The signal from a single scatterer, i, in Wendling et al.'s [1992] model is given by:

$$s_i(t) = A_i(t)\cos(\omega_0 t + \Psi_D(t) + \phi_i) \tag{2.42}$$

$$\Psi_D(t) = \frac{2\omega_0 \cos\theta}{c}\int_0^t v(\tau)\, d\tau \tag{2.43}$$

where $A_i(t)$ incorporates the backscattering coefficient of the particle and the shapes of the transmitted pulse and receiver gate, $\Psi_D(t)$ is the time varying phase caused by the scatterer motion and the phase ϕ_i is random and uniformly distributed between $[0, 2\pi]$. Although the signal is statistically equivalent to that of Mo & Cobbold [1986] the time domain approach provides additional information into the effects of transit time spectral broadening [Jones 1993] and allows the simulation of Doppler signals from accelerating (decelerating) blood.

Mo & Cobbold [1992] proposed an hybrid approach to model the Doppler signal in an effort to unify the particle and continuum approaches commonly used to model the scattering of ultrasound from blood. They divide the vessel into small voxels (elemental volumes) containing a large number of red blood cells. The simulated Doppler signal is computed as the sum of the contributions from all the voxels within the sample volume (particle approach). The signal from each voxel is considered to arise from the random fluctuations in local hematocrit (continuum approach). Their model includes geometric broadening and monotonic velocity profiles. Mo & Cobbold's model was further improved by Bascom & Cobbold [1996] who introduced a packing factor to explain the changes in the backscattered power with different flow conditions.

The above models generate signals corresponding to the demodulated Doppler signal. Other models exist that simulate directly the returned echoes from the blood. These models are very important in the study and assessment of the new time domain methods for estimating the blood velocity [Hein & O'Brien 1993, Jensen 1996]. Some examples of this type of model are referred below.

Olinger & Siegel [1981] have used a model of this type to study the usefulness of some Doppler signal processors. Azimi & Kak [1985] developed a model to study the effect of signal bandwidth, tissue attenuation constants and transducer characteristics on pulsed Doppler ultrasound systems. Bonnefous & Pesqué [1986] generated input signals for the time domain correlation algorithm that included transit time effects. This model was latter extended to generate two-dimensional colour flow images [Kerr & Hunt 1992*a*, Kerr & Hunt 1992*b*]. Oung & Forsberg [1996] developed a model for Doppler signals from pulsatile flow that includes nonaxial flow.

Good reviews on models of Doppler ultrasound signals can be found in [Jones 1993, Mo 1990, Mo & Cobbold 1993].

2.4 Doppler signal spectral estimation

In this section we describe some of the spectral estimation techniques commonly used to estimate the Doppler spectrum. We describe the periodogram (based on the Fourier transform), parametric methods, and time-frequency transforms. Although the short time Fourier transform is based in the Fourier transform, its description is only introduced in section 2.4.4 because it also belongs to the class of time-frequency transforms.

We do not describe the time-domain methods used in colour flow imaging because we are interested in the full frequency content of the Doppler signal and usually those methods are only used to estimate the mean frequency and variance of the spectrum.

A recent review of signal processing techniques used in cardiovascular ultrasound can be found in [Fish et al. 1997].

2.4.1 Spectral estimation basics

The Doppler signal received by the ultrasonic transducer arises from the scattering of the ultrasonic field by a large number of red blood cells. Thus, the received signal is stochastic (random) and its spectrum can only be estimated. The estimates of the Doppler spectrum themselves are stochastic.

The power spectrum (also known as power spectral density) of a wide sense stationary stochastic process, $x(t)$, is [Papoulis 1991]:

$$S(\omega) = \int_{-\infty}^{\infty} r_{xx}(\tau)\, e^{-j\omega\tau}\, d\tau \tag{2.44}$$

where,

$$r_{xx}(\tau) = \mathrm{E}[x(t+\tau)x^*(t)] \tag{2.45}$$

is the autocorrelation function, E[ ] is the expectation operator, and x^* denotes the complex conjugate of x.

The autocorrelation function is defined as the expectation of $x(t+\tau)x^*(t)$ obtained when averaged over an ensemble of realisations of the stochastic process [Kay 1988], but usually only a segment of a single realisation is available. For ergodic processes ensemble averages can be substituted by time averages [Kay 1988]. Thus, under these circumstances the autocorrelation function may be written [Kay & Marple 1981] as:

$$r_{xx}(\tau) = \lim_{T\to\infty} \frac{1}{2T} \int_{-T}^{T} x(t+\tau)x^*(t)\, dt \tag{2.46}$$

and the power spectrum may be represented [Kay & Marple 1981] by,

$$S(\omega) = \lim_{T\to\infty} \mathrm{E}\left\{ \frac{1}{2T} \left| \int_{-T}^{T} x(t)\, e^{-j\omega t}\, dt \right|^2 \right\} \tag{2.47}$$

Equations (2.44) and (2.47) are equivalent for stationary ergodic stochastic processes.

Nowadays, with the advent of the digital computer, the power spectrum and other signal processing techniques are usually evaluated digitally (Digital Signal Processing). The continuous-time signals are first sampled, normally at equally spaced time intervals, and the samples (discrete-time signals) are then processed numerically in the digital computer as sets of numbers.

2.4.2 The periodogram

In practice it is impossible to compute the theoretical power spectrum of a stationary random process because we can only observe the process for a limited time interval or the process can only be considered approximately stationary during a short time interval. Although the theoretical power spectrum cannot be computed, methods exist to estimate it. One of the more frequently used methods is the periodogram.

The periodogram of a discrete signal is,

$$I(\omega) = \frac{1}{N} \left| \sum_{n=0}^{N-1} x_n e^{-j\omega n} \right|^2 \tag{2.48}$$

where x_n is the n^{th} sample of the signal, The periodogram is periodic with period 2π and for real signals is an even function of ω. It can also be evaluated using an estimate of the

autocorrelation function [Kay 1988]

$$I(\omega) = \sum_{k=-(N-1)}^{N-1} \hat{r}_{xx}(k) e^{-j\omega k} \tag{2.49}$$

in a procedure sometimes called the Blackmann-Tukey method; $\hat{r}_{xx}$ is an estimate of the autocorrelation function and may be computed as:

$$\hat{r}_{xx}(k) = \begin{cases} \dfrac{1}{N} \displaystyle\sum_{n=0}^{N-1-k} x(n+k)x^*(n) & , k = 0, 1, \ldots, N-1 \\ \\ \hat{r}^*_{xx}(-k) & , k = -(N-1), -(N-2), \ldots, -1 \end{cases} \tag{2.50}$$

If the peridogram is evaluated at uniformly spaced frequencies[1] $\{\omega_m = 2\pi m/N, -N/2 \leq m < N/2\}$ it takes the form,

$$I(\omega_m) = \frac{1}{N} \left| \sum_{n=0}^{N-1} x_n e^{-j2\pi mn/N} \right|^2 \tag{2.51}$$

which can be evaluated with the FFT (Fast Fourier Transform) algorithm.

Because the FFT is so popular and such a computationally efficient algorithm the periodogram is usually evaluated with expression (2.51).

A major limitation of spectral estimation techniques that apply the periodogram to non-stationary processes is the trade off between the time and the frequency resolutions. For example, if the sampling time of each data segment is increased the frequency resolution of the spectral estimate increases but the time resolution decreases.

The expected value of the periodogram is [Oppenheim & Schafer 1975]

$$\begin{aligned} \mathrm{E}[I(\omega)] &= \sum_{k=-(N-1)}^{N-1} \mathrm{E}\left[\hat{r}_{xx}(k)\right] e^{-j\omega k} \\ &= \sum_{k=-(N-1)}^{N-1} \frac{N-|k|}{N} \, r_{xx}(k) \, e^{-j\omega k} \end{aligned} \tag{2.52}$$

$\mathrm{E}[I(\omega)]$ is not equal to the Fourier transform of r_{xx} due to the finite number of samples used and due to the factor $(N-|k|)/N$. Thus the periodogram is a biased estimate of the power spectrum, $S(\omega)$. Equation (2.52) can be interpreted as the Fourier transform of the product of the autocorrelation function by a Bartlett window [Kay 1988] and therefore the average

[1] Note that discrete-time angular frequency ω_m corresponds to a continuous-time frequency of $m\,f_s/N\,T_s$, where f_s is the sampling frequency, T_s is the window duration and N is the number of samples.

periodogram is the convolution of the true power spectrum with the Fourier transform of a Bartlett window.

Computing the variance of the periodogram is in general very complex but Oppenheim & Schafer [1975] have shown that for a Gaussian stochastic process the variance of the periodogram spectral estimate is,

$$\mathrm{var}[I(\omega)] = S(\omega)^2 \left\{ 1 + \left[\frac{\sin(\omega N)}{N \sin(\omega)} \right]^2 \right\} \tag{2.53}$$

The fractional variance of the periodogram is always greater than unity even for large N, thus the periodogram is not a consistent estimate of the power spectrum. As N becomes very large the variance tends to the square of the power spectrum and any individual estimate fluctuates wildly about the true spectrum value.

Since the periodogram is an inconsistent estimate of the power spectrum several methods were developed to reduce its variance. We describe here one of such methods, periodogram averaging.

Periodogram averaging

A simple procedure to reduce the variance of the periodogram is to divide the signal into several segments, compute the periodogram of each segment and finally average the individual periodograms [Porat 1994]. This method is sometimes referred as Bartlet's procedure [Oppenheim & Schafer 1975].

A simple implementation of the method is as follows. The N samples of the signal are divided into N_2 segments each with N_1 samples, so that $N = N_1 \times N_2$. If the separate periodograms are represented as:

$$I_p(\omega) = \frac{1}{N_1} \left| \sum_{n=0}^{N_1-1} x_{n+pN_1} \, e^{-j\omega n} \right|^2 \qquad , \, 0 \le p \le N_2 - 1 \tag{2.54}$$

the averaged periodogram is then:

$$I_{\mathrm{ave}}(\omega) = \frac{1}{N_2} \sum_{p=0}^{N_2-1} I_p(\omega) \tag{2.55}$$

If the separate segments are statistically independent the bias of $I_{\mathrm{ave}}(\omega)$ is the same as that of a single periodogram based on the same number of samples and the variance is reduced by a factor of N_2,

$$\begin{aligned} \mathrm{var}[I_{\mathrm{ave}}(\omega)] &= \frac{1}{N_2} \mathrm{var}[I_p(\omega)] \\ &= \frac{1}{N_2} S(\omega)^2 \left\{ 1 + \left[\frac{\sin(\omega N)}{N \sin(\omega)} \right]^2 \right\} \end{aligned} \tag{2.56}$$

for a Gaussian stochastic process. By using averaging, the variance of the spectral estimate can be reduced but this comes at a price, the resolution of the estimate is also reduced because the separate periodograms are computed using only N_1 samples instead of the original N.

The averaging of the periodogram is frequently used to reduce the variance of the Doppler spectrum [Evans et al. 1989], but due to the nonstationarity of Doppler signals the method must be used with some caution.

Any spectral estimation technique based on the Fourier transform requires the signal to be stationary, but the Doppler signal from arterial blood may not be considered stationary for periods longer than 10–20 ms [Evans et al. 1989]. Thus, the minimum time interval over which the signal may be considered stationary determines the maximum resolution of the spectral estimate. Periodograms of Doppler signals may only be averaged if the averaging is performed on the periodograms of corresponding parts from a number of heartbeats. This requires the proper alignment of the signals from the different heartbeats. Figure 2.18 illustrates how to carry out the averaging of the periodograms of Doppler signals.

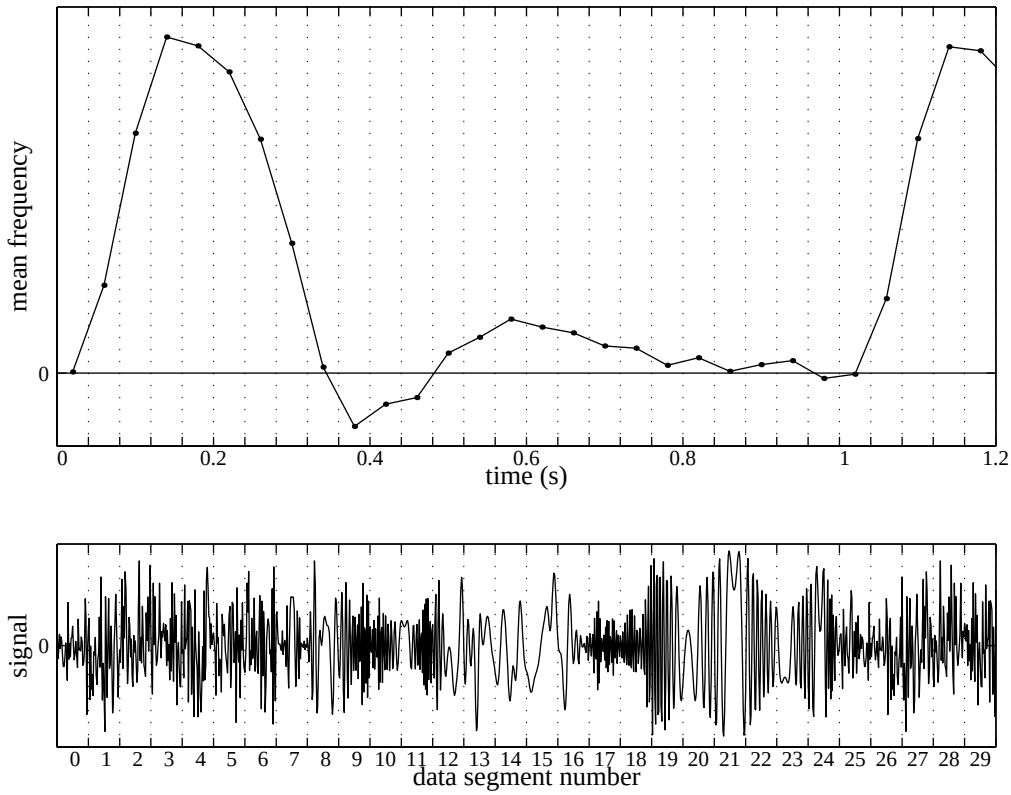

Figure 2.18: Illustration of the averaging procedure. The periodograms of data segments corresponding to the same part of the cardiac cycle (e.g. data segments 0 and 25) are averaged to reduce the spectral variance.

Periodograms of windowed signals

The periodogram suffers from an additional problem, spectral leakage into sidelobes. In order to reduce spectral leakage the time signals are, usually, multiplied by a smooth tapered window. As a result, the power spectrum is the convolution of the original power spectrum with the square of the modulus of the Fourier transform of the window. In fact the periodogram as defined in (2.48) results from the multiplication of the signal by a square window. The Fourier transform of the square window has significant side lobes that result in considerable frequency leakage.

In the present context a window, $w_K(k)$, is a function defined for all K such that, $-K \leq k \leq K$, with the following properties:

1. $w_K(k) = w_K(-k)$;
2. $w_K(0) = 1$;
3. $0 \leq w_K(k) \leq 1$.

The signal is multiplied by the window and the resulting periodogram is (assuming K¡N):

$$I_{\text{win}}(\omega) = \frac{1}{r_{ww}(0)} \sum_{k=-K}^{k=K} r_{ww}(k)\hat{r}_{xx}(k)e^{-j\omega k} \tag{2.57}$$

where $r_{ww}(k)$ represents the autocorrelation function of the window $w_K(k)$ computed as in (2.50).

The influence of the windowing on the periodogram is better understood if studied in the frequency domain. It is clear from (2.57) that the windowed periodogram is the multiplication of two signals in the time domain. Multiplication in the time domain is equivalent to convolution on the frequency domain and the windowed periodogram may also be represented by

$$I_{\text{win}}(\omega) = \frac{1}{2\pi} \int_{-\pi}^{\pi} W_K(\nu) I(\omega - \nu)\, d\nu \tag{2.58}$$

where $W_K(\omega)$, know as the smoothing kernel, is the Fourier transform of the autocorrelation of the window function. Using the autocorrelation theorem [Bracewell 1986, p. 115] it is possible to compute $W_K(\omega)$ directly from the window, $W_K(\omega)$ is simply the square of the absolute value of the Fourier transform of the window function.

The windows usually used in the Doppler signal to reduce the spectral leakage are the Hanning and the Hamming. The definitions of these windows and their energy spectra are shown in table 2.2 and in graphical form in figure 2.19. The boxcar window is also presented for comparison.

Name	Definition ($\|k\| \leq K$)	Energy Spectrum, $W_K(\omega)$
Boxcar	$w_K(k) = 1$	$\left[W^{\mathrm{B}}(\omega)\right]^2$
Hanning	$w_K(k) = 1/2 + 1/2\cos\frac{\pi k}{K}$	$\left[\frac{1}{4}W^{\mathrm{B}}\left(\omega - \frac{\pi}{K}\right) + \frac{1}{2}W^{\mathrm{B}}(\omega) + \frac{1}{4}W^{\mathrm{B}}\left(\omega + \frac{\pi}{K}\right)\right]^2$
Hamming	$w_K(k) = 0.54 + 0.46\cos\frac{\pi k}{K}$	$\left[0.23W^{\mathrm{B}}\left(\omega - \frac{\pi}{K}\right) + 0.54W^{\mathrm{B}}(\omega) + 0.23W^{\mathrm{B}}\left(\omega + \frac{\pi}{K}\right)\right]^2$

Table 2.2: Definition of various windows and their energy spectra (adapted from [Kay 1988, p. 71]). In all the windows $w_K(k) = 0$ for $|k| > K$ and the function $W^{\mathrm{B}}(\omega) = \frac{\sin\omega(K+1/2)}{\sin\omega/2}$ is the Fourier transform of the Boxcar window.

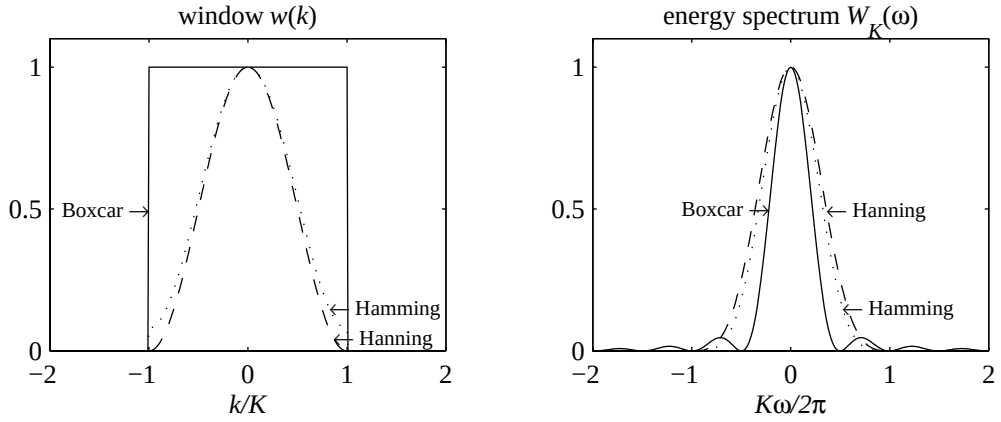

Figure 2.19: Graphical representation of various windows and their energy spectra.

2.4.3 Parametric methods

Spectral analysis based on the Fourier transform of time limited signals makes the fundamental assumption that the signal outside the data segment is zero. As a consequence, the estimated spectrum is broader than the spectrum of the original signal because it is convolved with the energy spectrum of the lime limited window. This is often referred as window broadening.

Model-based approaches also know as parametric models, make the assumption that the signal outside the data segment has the same statistical characteristics as that within. Based on *a priori* knowledge of the underlying process that generated the signal a mathematical model is chosen. Spectral estimation based on parametric model involves three different steps [Kay & Marple 1981]:

1. Selecting a times series model;

2. Estimating the parameters of the assumed model;

3. Obtaining the power spectral density by substituting the estimated parameters into the theoretical power spectral density implied by the model.

When modelling stationary random processes with parametric models, the signal is modelled as the output of a digital filter whose input is white noise.

A digital linear filter can be represented by the following expression:

$$y(n) = -\sum_{k=1}^{p} a_k\, y(n-k) + \sum_{k=0}^{q} b_k\, x(n-k) \qquad , a_p \neq 0 \tag{2.59}$$

where $y(n)$ is the output of the filter, $x(n)$ is the input signal, a zero mean white noise with variance σ^2 and a_k and b_k are the model parameters. This type of model is called an autoregressive-moving average model (ARMA).

The system transfer function, $H(z)$, between the input and output of the digital filter is:

$$H(z) = \frac{B(z)}{A(z)} \tag{2.60}$$

where $A(z)$ and $B(z)$ are z transforms given by,

$$A(z) = \sum_{k=0}^{p} a_k z^{-k} \qquad , a_0 = 1 \tag{2.61}$$

$$B(z) = \sum_{k=0}^{q} b_k z^{-k} \tag{2.62}$$

For the system to be stable all the zeros of $A(z)$ must lie inside the unit circle of the z-plane.

The white noise is filtered by the digital filter and the power spectral density of the output is [Kay 1988]:

$$\begin{aligned} S_{ARMA}(\omega) &= \sigma^2 H(z) H^*(1/z^*)\Big|_{z=e^{j\omega}} \\ &= \sigma^2 \left| \frac{B(e^{j\omega})}{A(e^{j\omega})} \right|^2 \end{aligned} \tag{2.63}$$

Two special cases of the ARMA model are the autoregressive model (AR) and the moving average model (MA). If all the $b_k = 0$ except $b_0 = 1$ the model is an AR model, and if all the $a_k = 0$ except $a_0 = 1$ the model is an MA model. The AR is the type of model most frequently used.

The power spectral density for the AR and MA are simply,

$$S_{AR}(\omega) = \sigma^2 \left| \frac{1}{A(e^{j\omega})} \right|^2 \tag{2.64}$$

$$S_{MA}(\omega) = \sigma^2 \left| B(e^{j\omega}) \right|^2 \tag{2.65}$$

Several methods exist to estimate the model parameters from the signal or from its autocorrelation. Some of the more frequently used are methods based on the Yule-Walker equations, Burg algorithm, modified covariance, least square estimation and the maximum likelihood estimation. The description of those methods is out of the scope of this work, it may be found in any standard textbook on spectral estimation, e.g. [Kay 1988, Porat 1994].

Parametric methods can improve the resolution of the spectral estimate and are immune to sidelobe spectral leakage, but there is still the assumption of signal stationarity and the quality of the spectral estimate depends very much on the correctness of the chosen model and its order.

A lot of work has been done on the estimation of the Doppler spectrum using parametric modelling. Some works studied the applicability of parametric modelling to Doppler signals and compared the performance of the parametric spectral estimators with other methods [David et al. 1991, Kaluzynski 1987, Kaluzynski 1989, Vaitkus & Cobbold 1988, Vaitkus et al. 1988]. Most of these works concluded that the spectral estimate provided by the parametric models offer an improved spectral resolution compared with the periodogram.

Schlindwein & Evans [1990] analysed the process of selecting the model order of AR models of the Doppler signal and concluded that overestimating the model order is better than underestimating it when estimating spectral shape. Fort et al. [1995] proposed a method for selecting optimum model orders for different parts of the cardiac cycle, but Fan & Evans [1994*a*] advert that AR modelling of narrow-band Doppler signals should be used with caution because the AR spectral estimate may not correctly represent the signal peak-power relationship.

A real-time implementation of AR spectral estimation was present by Schlindwein & Evans [1989]. When only some spectral parameters like the mean frequency, maximum frequency or the bandwidth are needed, low-order models can be used so that the computational complexity is reduced allowing their possible use in colour flow imaging [Loupas & McDicken 1990, Ruano & Fish 1993].

2.4.4 Time-frequency transforms

The periodogram and parametric modelling spectral estimation make the assumption that the signal is stationary. However, the Doppler signal may only be considered approximately stationary for periods up to 10–20 ms [Evans et al. 1989] depending on the phase of the cardiac cycle being analysed. Thus, better spectral estimation techniques suitable for nonstationary signals are needed for processing the Doppler signal.

The following sub-sections briefly describe some of the time-frequency transforms that have been applied to the Doppler signal: the spectrogram, the Wigner-Ville distribution, the Choi Williams distribution and the Bessel distribution. The description of the various time-frequency transforms is given here for completeness only.

More detailed studies of time-frequency transforms can be found in [Cohen 1989, Cohen 1995, Porat 1994].

The short-time Fourier transform and the spectrogram

The short-time Fourier transform (STFT) and the square of its magnitude, the spectrogram, are the most widely used methods for studying nonstationary signals [Cohen 1995]. In particular, the spectrogram is the time-frequency transform technique most frequently used to process the Doppler signal.

The purpose of the STFT is to find the time variation of the frequency of the signal. It does so by analysing small segments of the signal centred at time t.

The STFT of a signal $x(t)$ is:

$$S_{\mathrm{STFT}}(t,\omega) = \int_{-\infty}^{\infty} x(\tau) w(\tau - t) e^{-j\omega\tau}\, d\tau \tag{2.66}$$

where $w(t)$ is an even window.

The spectrogram is simply the square of the magnitude of the STFT,

$$\begin{aligned} S_{\mathrm{spec}}(t,\omega) &= |S_{\mathrm{STFT}}(t,\omega)|^2 \\ &= \left| \int_{-\infty}^{\infty} x(\tau) w(\tau - t) e^{-j\omega\tau}\, d\tau \right|^2 \end{aligned} \tag{2.67}$$

The width of the time window, $w(t)$ determines the time and frequency resolutions of the spectrogram. A long time window will result in poor time resolution and good frequency resolution; a short time window will have the opposite effect. The spectrogram may be conceived as a series of windowed periodograms evaluated sequentially in time.

Other time-frequency transforms used to process the Doppler signal

Other time-frequency transforms were used recently to estimate the frequency content of the Doppler spectrum. They all belong to Cohen's class of time-frequency transforms [Cohen 1989].

The first to be used was the Wigner-Ville distribution (WVD) which for a signal $x(t)$ is given by,

$$\mathrm{WVD}(t,\omega) = \int_{-\infty}^{\infty} x\left(t + \frac{\tau}{2}\right) x^*\left(t - \frac{\tau}{2}\right) e^{-j\omega\tau}\, d\tau \tag{2.68}$$

Fan & Evans [1994*b*] used the WVD distribution to estimate the instantaneous mean frequency of the Doppler signal. They concluded that the estimate produced by the WVD is not very reliable when the signal contains more than one frequency component. This is due to cross-terms between any two frequency components present in the signal resulting in

spurious terms in the time-frequency display.

[Zeira et al. 1994] compared the performance of the spectrogram with that of a smoothed WVD called pseudo Wigner distribution. They found that the pseudo Wigner distribution produces better results only for high signal to noise ratios.

Choi & Williams [1989] introduced a new distribution now called the Choi Williams distribution (CWD) that reduces the cross terms of the time-frequency representation. The CWD of a signal, $x(t)$, is:

$$\mathrm{CWD}(t,\omega) = \int_{-\infty}^{\infty}\int_{-\infty}^{\infty} \sqrt{\frac{\sigma}{4\pi\tau^2}}\, e^{-\frac{\sigma(\mu-t)^2}{4\tau^2}}\, x\Big(\mu+\frac{\tau}{2}\Big)\, x^*\Big(\mu-\frac{\tau}{2}\Big)\, e^{-j\omega\tau}\, d\mu d\tau \tag{2.69}$$

where $\sigma > 0$ is a scaling factor that influences the resolution of the auto-terms and cross terms in opposite directions; large σ results in high resolution of the auto-terms and a small ($\sigma < 1$) reduces the effect of the cross-terms [Choi & Williams 1989].

Recently Guo et al. [1994*b*] proposed a new time-frequency distribution capable of effectively suppressing the cross terms. It is called the Bessel distribution (BD) and is defined as:

$$\begin{aligned}\mathrm{BD}(t,\omega) = \int_{-\infty}^{\infty}\int_{-\infty}^{\infty} \frac{2}{\pi\alpha|\tau|}\sqrt{1-\left(\frac{\mu-t}{\alpha\tau}\right)^2}\,\mathrm{rect}\left(\frac{\mu-t}{\alpha\tau}\right) \\ \cdot\, x\Big(\mu+\frac{\tau}{2}\Big)\, x^*\Big(\mu-\frac{\tau}{2}\Big)\, e^{-j\omega\tau}\, d\mu d\tau\end{aligned} \tag{2.70}$$

where,

$$\mathrm{rect}(x) = \begin{cases} 1 & ,\ |x| \le 1 \\ 0 & ,\ |x| > 1 \end{cases} \tag{2.71}$$

Guo et al. [1994*a*] compared the performance of various spectral estimation techniques like the spectrogram, AR modelling, CWD and BD for estimating the mean frequency of simulated Doppler signals from the femoral artery. They concluded that the BD was the technique that performed the best and the CWD and AR modelling also provided good time-frequency estimates of the Doppler spectrum.

More recently Cardoso et al. [1996] analysed the performance of the spectrogram, WVD, CWD and BD to estimate the Doppler spectral width. They concluded that on overall the CWD gave the best performance. [Cardoso 1998] developed a real-time implementation of the CWD using parallel processing techniques.

2.5 Concluding remarks

This chapter presented some background knowledge on blood flow, Doppler ultrasound and spectral signal analysis.

Some of the most important components of the human circulation like the heart, the blood vessels, and the blood were described as well as the various types of blood flow usually found in the circulation; laminar, turbulent, and pulsatile flow. Various models of the blood flow in the arterial circulation were presented.

Some of the Doppler ultrasound instruments that have been used were described and the main factors that contribute to the broadening of the Doppler spectrum were discussed. Part of the spectral broadening arises from the physical characteristics of the measuring system (intrinsic spectral broadening) and the spectral techniques used to estimate the spectrum (window broadening), while the rest is inherent to the blood flow itself like the velocity profile and the existence vortices or turbulence.

Various models for the Doppler ultrasonic signal backscattered by the moving red blood cells were described.

The chapter ends with the description of several of the spectral estimation techniques that have been applied to the Doppler signal. Some of these techniques like the periodogram and the parametric methods assume that the signal is stationary. Since the Doppler signal is non-stationary they can only be used in short data segments where the assumption of the signal being stationary is reasonable. The more modern time-frequency methods are specific for non-stationary signals and some of them have been tried successfully with the Doppler signal.

Chapter 3

Model of blood flow in the human lower limb

3.1 Introduction

The time-varying blood velocity field at any site in the circulation varies significantly from person to person because of the different physical and physiological characteristics. Even when measured from the same person but at different times the blood velocity fields may change significantly.

The high variability of the blood flow makes the testing of new diagnostic techniques with *in vivo* measurements unreliable because the tests cannot be performed under controlled conditions.

It seemed then appropriate to develop a model of the blood flow in a section of the arterial tree to allow the generation of simulated time-varying blood velocity fields.

The 'correct' approach to model blood flow would be to solve the Navier-Stokes for the complete section of the circulation being modelled. This would be a very complex task and probably impossible because of the computer power needed and because the mechanical characteristics of all the blood vessels are usually not known. In order to reduce the complexity of the problem we have chosen to model blood flow using transmission lines. The electric model generated pressure and volumetric blood flow waveforms and the time-varying velocity profile was computed from the blood flow waveform and the characteristics of the artery at the measurement site. As was shown in Chapter 2, the propagation of pressure and flow perturbations in arteries is similar to the transmission of electrical signals in transmission lines under certain simplifying conditions.

Two of the conditions required for the transmission line model to be valid are that the arteries being modelled are long and straight, as a consequence we have chosen to model the blood flow in the lower limb. In fact, this lower limb is one of the regions where stenoses are more common.

The model of the human arterial blood flow in the lower limb described in this chapter generates simulated pressure and volumetric flow waveforms in the main human arteries from the iliac bifurcation down to the pedal arteries. The model is an electric analogue of the lower limb arterial tree in which electric voltage corresponds to blood pressure and electric current corresponds to volumetric blood flow. It is possible to establish other correspondences between hemodynamic and electric phenomena.

The electrical model of the lower limb arterial tree was implemented using the SPICE circuit simulator, an industry standard for the simulation of electric and electronic circuits. The use of the SPICE circuit simulator was significantly advantageous over the construction of an hardware circuit made of discrete electric components. For example, it is much easier to change a software circuit description than to actually change a hardware circuit and the results of the software simulation are insensitive to component aging and other external factors like the temperature.

3.2 Lower limb arterial bed

The main arteries of a human lower limb are represented in figure 3.1. Blood leaves the left ventricle through the aorta artery to feed the entire body. The lower end of the aorta artery is known as the abdominal aorta that divides into the left and right common iliac arteries before entering in the legs.

Each one of the common iliac arteries feeds one leg and divides into the internal iliac, also known as the hypogastric artery, that feeds the pelvic region and the external iliac that continues down to the lower periphery. The external iliac artery is the first section of the long artery that runs longitudinally in the lower limb down to the knee. The other sections are usually called the common femoral artery, the superficial femoral artery and the popliteal artery. The external iliac becomes the common femoral artery as soon as it enters the thigh passing through the inguinal ligament. Some centimetres below the inguinal ligament the common femoral artery divides into the profunda femoral and the superficial femoral arteries. The profunda femoral artery runs deep into the thigh to feed its major muscles, while the superficial femoral artery continues down until the popliteus where its name changes to popliteal.

Just after the knee the popliteal artery usually divides into three arteries, the anterior tibial, the posterior tibial and the peroneal arteries, although the anatomy varies from person to person [Gray 1973, p. 679] sometimes dividing only into two vessels the anterior and the posterior tibial arteries.

One major problem faced when modelling blood flow in humans is the difficulty in finding accurate and reliable data on the physical characteristics of the arterial bed. It is very difficult to make accurate *in vivo* measurements and there is a high degree of variability in the human population.

The physical characteristics of the lower limb arterial tree needed to implement the

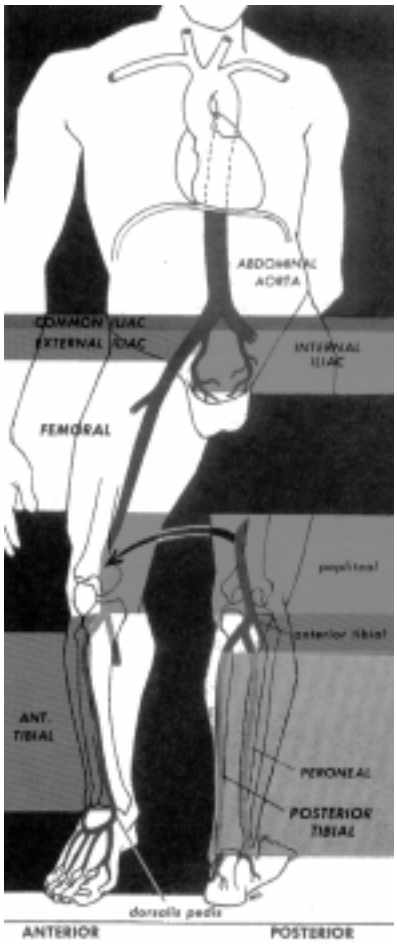

Figure 3.1: Major arteries of the lower limb (from [Reith et al. 1978]).

transmission line model (see section 2.2.4) were taken from two sources in the literature [Avolio 1980] and [Westerhof et al. 1969]. Table 3.1 presents a compilation of the length, radius and Young's modulus, E, found in the above mentioned references, for the main lower limb arteries in a male subject of 'normal height and weight'.

3.2.1 Some characteristics of the pressure and flow pulses in the lower limb

The flow waveform in the normal arterial circulation of the human limb is triphasic, it contains a forward systolic flow component, reverse flow and a second forward flow component during diastole [Jäger et al. 1985, Johnston et al. 1984]. A typical sonogram from a normal common femoral artery was shown in figure 2.13. The absence of the reverse flow component in the waveform is a strong indication of arterial occlusive disease.

In the human arterial circulation the amplitude of the pressure pulse increases as it travels to the periphery (see for example [Milnor 1989, p. 225]). This pressure pulse amplification is the result of the interaction of the incident wave with waves reflected from the peripheral

Artery	Length (cm)	Internal radius (mm)	Wall thickness (mm)	E 10^6 (dyn/cm^2)	Reference
Abdominal Aorta (a)		5.5	0.78	4	[Westerhof et al. 1969]
Common Iliac	5.8	3.7	0.63	4	[Westerhof et al. 1969]
Internal Iliac	5.0	2.0	0.40	16	[Avolio 1980]
External Iliac	8.3	2.9	0.55	4	[Westerhof et al. 1969]
Common Femoral	6.1	2.7	0.53	4	[Westerhof et al. 1969]
Profunda Femoral	12.6	2.3	0.49	16	[Avolio 1980]
Superficial Femoral	25.4	2.4	0.50	8	[Avolio 1980]
Popliteal	18.8	2.0	0.47	8	[Avolio 1980]
Posterior Tibial I (b)	2.5	1.3	0.39	16	[Avolio 1980]
Posterior Tibial II	30.0	1.0	0.20	16	[Avolio 1980]
Anterior Tibial	32.2	1.8	0.45	16	[Avolio 1980]
Peroneal	31.8	1.3	0.39	16	[Avolio 1980]

a) data refers to the distal end of the abdominal aorta artery.
b) small arterial segment between the peroneal and anterior tibial ramifications (see figure 3.1).

Table 3.1: Typical values for physical characteristics of the human lower limb arteries.

vascular beds and arterial bifurcations. The flow pulse behaves differently and decreases as it approaches the arterioles.

Table 3.2 shows values, published by Jäger et al. [1985], for the peak systolic and peak reverse velocities of some arteries of the lower limb.

Artery	V_{sys} (cm/s)	V_{rev} (cm/s)
External Iliac	119.3 ± 21.7	41.5 ± 10.7
Common Femoral	114.1 ± 24.9	40.6 ± 9.2
Superficial Femoral (proximal)	90.8 ± 13.6	38.8 ± 8.2
Superficial Femoral (distal)	93.6 ± 14.1	35.0 ± 9.8
Popliteal	68.8 ± 13.5	27.8 ± 9.2

Values given as mean ± standard deviation.
V_{sys}, peak systolic flow velocity.
V_{rev}, peak reverse flow velocity.

Table 3.2: Values of peak systolic and reverse blood velocity at five different sites in the normal lower limb (from [Jäger et al. 1985]).

Although the flow pulse decreases as it travels to the periphery the pulsatility of the velocity waveform increases as it approaches the foot [Johnston et al. 1978]. Usually, when an arterial segment of the lower limb has a stenosis, the pulsatility of the flow decreases distally to the obstruction site. This is probably the result of the dampening of the flow waveform at the stenosis and the local readjustment of the peripheral impedances in order to compensate for the otherwise reduced flow.

The Pulsatility Index (PI) defined as

$$\mathrm{PI} = \frac{\text{peak-to-peak velocity}}{\text{mean velocity}} \tag{3.1}$$

has been used for a long time as an estimator of the pulsatility of the velocity waveform and to predict diseased states (see for example: [Johnston et al. 1978, Johnston et al. 1983, Thompson & Trudinger 1990]).

3.3 Introduction to the SPICE circuit simulator

The simulation and testing of electric circuits before actually building them results normally in time saving and allows the discovery of design faults at an early stage. Another advantage of the use of circuit simulators is the ease with which individual components can be checked and fine-tuned at the design stage resulting in great savings of resources.

The SPICE program (Simulation Program with Integrated Circuit Emphasis) is the industry-standard for circuit analysis and simulation of electric circuits. SPICE was developed at the University of California, Berkeley in the late 60s and early 70s and in its original version is in the public domain. Over the years several commercial versions of the SPICE were developed with some added capabilities. Most of the commercial versions include support software programs that facilitate the interaction between the designer and the SPICE program, namely some allow the description of the circuit in schematic form and offer much improved graphical outputs.

In this work we have used PSPICE [1993] developed by MicroSim Corporation for personal computers. Two versions of the program were used, versions 4.04 and 5.3, during the development of this work.

A detailed description of how to use SPICE and how it performs the simulation is out of the scope of this thesis. Briefly, SPICE solves, numerically, the Kirchoff equations of the electric circuit until it converges to the solution.

Detailed information on SPICE may be found in various books, for example [Kundert 1995, Rashid 1990, Tuinenga 1988] and the software user manual [PSPICE 1993]. However, to illustrate its use a simple circuit simulation is described.

The input to the SPICE circuit simulator is a file, called the netlist, containing the description of all the components in the circuit and how they are connected with each other. The netlist also contains lines specifying the type of analysis and output to be generated.

In SPICE the circuit description is simply a list of the circuit elements with the nodes to which they are connected. Each circuit element is described in a separate line with the following format:

name 1st node 2nd node ... value

The type of the circuit elements is determined by the first letter of their name as shown

in table 3.3, note that the order of the nodes is important for circuit elements having polarity (eg., voltage sources, diodes) and for elements with more than two connections (e.g. bipolar transistors, transmission lines).

C	Capacitor
D	Diode
E	Voltage-controlled voltage source
F	Current-controlled current source
G	Voltage-controlled current source
H	Current-controlled voltage source
I	Independent current source
J	Junction FET
L	Inductor
M	MOSFET
Q	Bipolar transistor
R	Resistor
T	Transmission line
V	Independent voltage source

Table 3.3: Correspondence between the first letter of the name and the circuit element simulated by SPICE.

In order to illustrate how the circuit description is build from a circuit, figure 3.2 shows a simple RC circuit and the corresponding circuit description for SPICE.

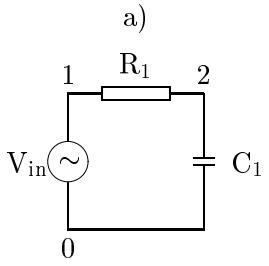

b)

```
Vin   1   0   SIN(0 0.1 1MEGHZ)
R1    1   2   5.6 kOHM
C1    2   0   1 uF
```

Figure 3.2: Example of the simulation of a simple RC circuit in SPICE: a) the circuit diagram; b) the SPICE circuit description. Resistor R1 connects nodes 1 and 2, capacitor C1 connects nodes 2 and 0, and the voltage source V_{in}, which connects nodes 1 and 0, generates a sine wave with 0 v off-set voltage, 0.1 v peak voltage and a frequency of 1 MHz.

The output of the circuit can be the voltage between any two nodes or alternatively the current passing through any of the components.

3.4 SPICE model

Blood flow in the circulation is very complex as we have seen in Chapter 2. Modelling such a complex system without some form of simplification would be very difficult. Thus, in order make the problem of modelling blood flow in the lower limb more tractable we assume that:

- the non-linear terms of the Navier-Stokes equations can be neglected;
- the artery is circular;
- the variation of the arterial radius due to the pressure perturbation is small compared to the radius of the artery;
- the artery is longitudinally constrained;
- the flow is laminar and axisymmetric;
- 'leakage' of flow through lateral branches and the arterial wall is directly proportional to pressure;
- the wavelength of the perturbations is large in relation to the radius of the arteries.

We also ignore inlet and branching point effects. The above assumptions are essentially those used by Westerhof et al. [1969].

Under these conditions the Navier-Stokes equations may be written in a simplified form analogous to the 'telegraph equations' (see section 2.2.4) and the transmission of flow and pressure perturbations in the arterial tree is similar to the transmission of electric signals in electrical transmission lines.

The analogy between hemodynamic phenomena and electric phenomena permits the use of electric models to simulate the blood flow in the human circulation. Various correspondences between the hemodynamic variables and the electric variables may be made. We have opted to use the one in which blood pressure corresponds to electric voltage and volumetric blood flow corresponds to electric current.

The centimetre-gram-second (cgs) system of units has been used here to express the values of the hemodynamic parameters of the model because it is the one usually used to express quantities related with blood flow in the human circulation. Another reason to chose the cgs system of units rather than the SI (Sistéme International d'Unités) is that when the cgs system is used the range of numbers used for model parameters is lower and the PSPICE algorithm converges to the solution more rapidly.

The values of the electric components of the model are expressed in the usual units of the SI. Table 3.4 shows the correspondence between the hemodynamic and the electrical quantities.

The model computes pressure in $\mathrm{dyn/cm^2}$ but whenever we refer to pressure values in the text or plot pressure waveforms we use millimetres of mercury (mm Hg) because it is

Hemodynamic		Electrical	
Variable (symbol)	Units	Variable (symbol)	Units
Pressure (p)	dyn/cm^2	Voltage (V)	volt
Flow (Q)	cm^3/s	Current (I)	ampere
Resistance (R_h)	dyn s/cm^5	Resistance (R)	ohm
Inertance (L_h)	g/cm^4	Inductance (L)	henry
Compliance (C_h)	cm^5/dyn	Capacitance (C)	farad
Leakage (G_h)	cm^5/dyn s	Conductance (G)	ohm^{-1}
Impedance (Z_h)	dyn s/cm^5	Impedance (Z)	ohm

Table 3.4: Correspondence between hydrodynamic units and electrical units (adapted from [Milnor 1989]).

the standard unit for blood pressure. At a temperature of 21° C, 1 mm Hg $\simeq$ 1329 dyn/cm^2 [Milnor 1989].

The model is divided in three main parts: the input generator, the arteries and the peripheral vascular beds. These parts of the model will be described in the following pages.

3.4.1 The input waveform

The systemic circulation above the iliac bifurcation is modelled in our circuit by a current generator in parallel with an output resistor (Norton equivalent of a current generator).

According to Milnor [1989, p. 157], the pressure and flow waveforms in the circulation are such that they may be represented, with a small error, by their first 10 harmonics. Thus, the input of the arterial model was implemented as a direct current source, I_0, in parallel with 10 sinusoidal current sources, I_1–I_{10}. Each one of the sinusoidal current sources corresponds to one of the harmonics of the waveform. The amplitudes of the current sources are set so that the current, I_{out}, driven to the model of the lower limb corresponds to the desired input waveform for the model. Figure 3.3 shows diagrammatically the generator that drives the blood flow model.

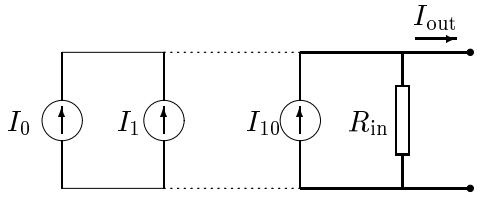

Figure 3.3: Schematic of the input generator.

It is difficult to obtain the value of the generator output resistor R_{in} from *in vivo* measurements and as it was not available in the literature, its value was considered to be equal

to the characteristic impedance of the abdominal aorta.

The input flow waveform was obtained by digitising the maximum frequency envelope of a typical sonogram [Burns 1988] of the flow in the abdominal aorta just before the iliac bifurcation. The harmonics of the digitised waveform were scaled to a mean flow of 900 ml/min (15 $cm^3\,s^{-1}$) [Raines et al. 1974]. It was further assumed that the heart rate is 60 beats per minute, this results in a fundamental frequency of 1 Hz.

Figure 3.4 shows the mean flow waveform used as the driving current of the model.

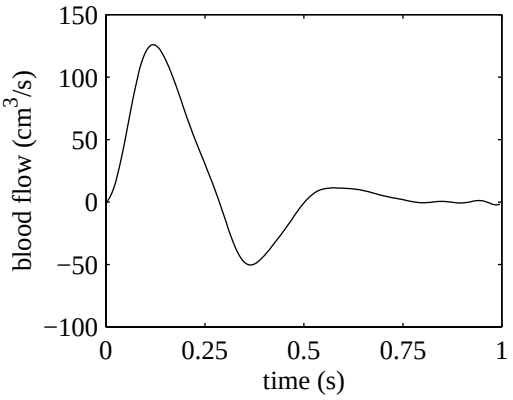

Figure 3.4: Input current waveform.

3.4.2 Arteries

As already mentioned in Chapter 2 the arterial wall is elastic and the propagation of the pressure and flow waveforms is, under some simplifying assumptions, similar to the propagation of electric perturbations in electric transmission lines.

In our model each artery is simulated by a lossy transmission line whose electrical characteristics are calculated from the corresponding physical characteristics presented in table 3.1 and some assumed values.

All the arteries except the small segment of 2.5 cm between the peroneal and anterior tibial ramifications are modelled by lossy transmission lines that include transverse losses to account for the 'leakage' of flow through smaller vessels and the vessel wall.

The versions of PSPICE available to implement the electrical model do not provide a direct implementation of lossy transmission lines. Thus, a lumped model was used.

Implementation of a lossy transmission line with a lumped circuit in SPICE

The SPICE circuit used to model lossy transmission lines was a variation of the one proposed by Gruodis [1979].

The model was implemented by substituting a lossy transmission line of length l by a cascade of N sections of ideal transmission line with length l/N interlaced by $N-1$ series resistors R_s and $N-1$ parallel resistors R_t, as shown in figure 3.5.

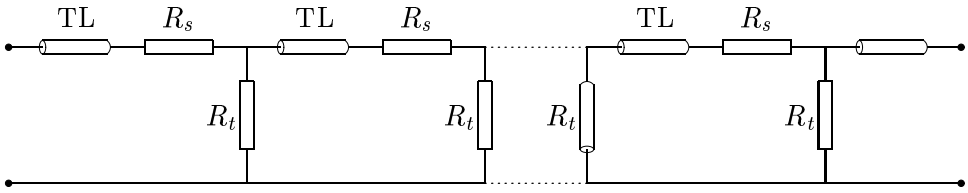

Figure 3.5: Schematic of the implementation of a lossy transmission line as a lumped circuit in SPICE; TL is a lossless transmission line, $R_s = R'l/(N-1)$, $R_t = (l/(G'\big(N-1\big))$, l is the length of the transmission line and N is the number of lossless transmission line segments used.

The number of sections of ideal transmission line that were used to simulate the lossy transmission lines influenced the accuracy of the simulation. Theoretically, as the number of sections increases the better the approximation. However, this comes at a price, the time taken by the SPICE algorithm to solve the equations of the circuit increases significantly and for very small sections the algorithm sometimes does not converge at all due to the accumulation of numerical errors.

In order to chose the number of transmission line sections to use in our model the voltage and current transfer functions and the input impedance of the lumped circuits were compared with the corresponding variables of continuous lossy transmission lines. The comparison was carried out using ABDC matrices techniques commonly used to analyse microwave circuits (see for example [Rizzi 1988]). From the results of the comparison for the various arteries in the lower limb we opted to use a lumped circuit with 5 sections of lossless transmission line because the maximum error in the current and voltage transfer functions was below 2% for the frequency range used in the model (0-10 Hz).

A lumped circuit with only 2 sections of ideal transmission line simulates the small segment of the posterior tibial artery between the ramifications of the peroneal and anterior tibial arteries. The circuit simulating this vessel has no parallel resistor because the vessel is so small that the leakage of flow may be neglected.

Computation of the transmission lines characteristics

For each artery the following parameters were computed, the characteristic impedance of the segments of lossless transmission line, Z_{0h}, the phase velocity, c_0, the longitudinal resistance per unit length, R'_h, and the conductance per unit length, G'_h. These haemodynamic quantities were then converted to electrical quantities using the equivalencies in table 3.4.

The characteristic impedance was computed using the *Water-Hammer* equation,

$$Z_{0h} = \frac{\rho c_0}{\pi R_0^2} \tag{3.2}$$

where ρ is the density of blood and R_0 is the radius of the vessel.

The phase velocity was computed with a simplified version [Nichols & O'Rourke 1990] of the correction to Moens-Korteweg equation introduced by Bergel [1961] to account for a 'thick' wall,

$$c_0 = \sqrt{\frac{E\,h}{2\rho\,R_0\,(1-\sigma^2)}} \tag{3.3}$$

where h is the thickness of the wall and σ is the Poisson ratio of the wall, which in arteries is very close to 0.5 [Nichols & O'Rourke 1990]. Assuming a Poisson ration of 0.5 for the arterial wall, (3.3) yields a value for c_0 which is higher than that predicted by the Moens-Korteweg equation (2.6) by a factor of $\sqrt{4/3}$. This 'corrected' value is closer to the values measured *in vivo* [Nichols & O'Rourke 1990].

The value of the resistor, R_{vh}, accounting for viscous losses in each artery was computed from Poiseuille's law (2.3)

$$R_{vh} = \frac{8\mu}{\pi R_0^4}\,l \tag{3.4}$$

note that $R'_h = R_{vh}/l$.

In the transmission line simulating each artery the value of the resistors R_s were given by $R_v/(N-1)$ (where R_v is the electrical equivalent of R_{vh}), which yields $R_v/4$ for all arteries except the 2.5 cm segment of the posterior tibial that has only one series resistor.

Since no consistent quantitative data on the volumetric flow for all the major vessels of the lower limb was, to the author's knowledge, available at the time when this work was carried out the 'leakage' of flow through the vessels had to be estimated. We assumed that the flow 'leakage' in the various arteries is the following:

- common iliac, external iliac and common femoral 10%
- superficial femoral, popliteal, internal iliac and profunda femoral 25%
- anterior tibial, posterior tibial and peroneal 50%

The percentage of 'leakage' of each artery was defined as,

$$\%\text{leakage} = \frac{I_{\text{in}} - I_{\text{out}}}{I_{\text{in}}} \times 100 \tag{3.5}$$

where I_{in} and I_{out} are the mean volumetric blood flow entering and leaving the artery as shown below.

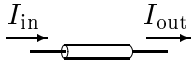

(proximal) (distal)

To chose the above values for the flow 'leakage' we have assumed that the 'leakage' increases towards the periphery as the arteries get closer to the capillary bed and we adjusted the percentage of 'leakage' in the model to obtain values for the PI similar to the ones measured *in vivo*.

Recently Holland et al. [1998] have measured the volumetric blood flow in some of the lower limb arteries and observed that only approximately 53% of the flow entering the common femoral artery reaches the superficial femoral and only 48% of superficial femoral artery inflow continues into the popliteal artery. Their findings suggest that we underestimated the flow 'leakage' in the arteries and future versions of the current blood flow model should take Holland et al.'s [1998] data into account.

Table 3.5 shows the values of the parameters computed for the transmission lines corresponding to each artery, note that the conductance of each artery, G_{leak}, was computed so that the flow at the end of the artery is reduced by the desired percentage. The parameters were computed using the following other characteristics, $\rho = 1.06$ g/cm^3, $\sigma = 0.5$ and $\mu = 0.035$ poise.

Artery	c_0 (cm/s)	Z_0 (ohm)	R_v (ohm)	G_{leak} (μohm^{-1})
Abdominal Aorta	597.3	666		
Common Iliac	654.5	1613	27.6	5.625
Internal Iliac	1418.7	11967	278.5	6.328
External Iliac	690.7	2771	104.6	2.531
Common Femoral	702.7	3252	102.3	2.278
Profunda Femoral	1464.2	9339	401.3	2.563
Superficial Femoral	1023.8	5997	682.3	2.563
Popliteal	1087.4	9172	1047.2	1.992
Posterior Tibial I (a)	1737.5	34689	780.1	
Posterior Tibial II	1418.7	47867	26738.0	1.586
Anterior Tibial	1586.1	16517	2733.8	0.548
Peroneal	1737.5	34689	9923.4	0.750

a) small arterial segment between the peroneal and anterior tibial ramifications (see figure 3.1).

Table 3.5: Electrical characteristics for the transmission lines that simulate the arteries in the lower limb.

3.4.3 Peripheral arterial beds

The peripheral impedances were modelled by a three-element *Windkessel* model also known as the *Westkessel* model [Noordergraaf 1978],which consists in one resistor in series with a resistor-capacitor parallel circuit. Figure 3.6 shows diagrammatically the *Westkessel* circuit.

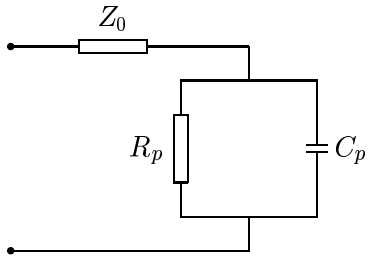

Figure 3.6: The *Westkessel* circuit used to model the impedance of the peripheral arterial beds.

The value of the series resistor is equal to the characteristic impedance, Z_0, of the artery feeding the peripheral bed, R_p represents the peripheral resistance of the vascular bed and C_p accounts for the vascular bed compliance.

To estimate values for R_p and C_p we followed the procedure outlined by Raines et al. [1974]. They cite some studies performed during surgery that suggest that the flow in the common iliac artery divides equally between the internal and external iliac artery. A similar division of flow occurs at the end of the common femoral artery.

At the knee trifurcation we have assumed that the division of flow between the three vessels is inversely proportional to the characteristic impedance of each vessel.

Raines et al. [1974] say that the compliance of the small vessels of a leg is 0.04 $\mathrm{cm}^3/\mathrm{mm\,Hg}$ ($\simeq 30\ \mu\mathrm{cm}^5/\mathrm{dyne}$). We then computed the vascular compliance for each branch by assuming that the compliance of one leg divides among the various branches in proportion to their mean flow.

The computed values for the peripheral resistance and compliance of the various peripheral beds are shown in table 3.6.

Artery	R_p (kohm)	C_p (μfarad)
Internal Iliac	52.7	15.0
Profunda Femoral	130.1	7.5
Posterior Tibial II	1825.0	1.4
Anterior Tibial	630.6	4.1
Peroneal	1334.0	2.0

Table 3.6: Values of the electric components of the peripheral vascular beds models.

3.4.4 Adjustment of model parameters

The description of the blood flow model made in the previous sections may convey the impression that the model parameters were immutable from the beginning of the development phase. That was not the case.

In fact various modifications and adjustments were made during the development of the

model. For example, at first the arteries were modelled with lossy transmission lines without shunt conductances but this resulted in flow waveforms whose PI was too low in the lower leg vessels. The inclusion of shunt losses, to account for flow leakage through small vessels and the vessel wall, increased the PI and as a consequence the model results mimicked the physiological waveforms more closely. The values for the shunt conductance were adjusted until the variation of PI along the leg resembled what had previously been published.

Another example of important adjustments that were made is the one concerning the peripheral impedances both in terms of values and circuits. Initially the peripheral impedances were modelled by a *Windkessel* circuit (one resistor in parallel with one capacitor) but that resulted in to high reflections and the pressure and flow waveforms were highly distorted. To circumvent this a *Westkessel* circuit was used and the reflection at the periphery decreased.

3.5 Assessment of model results

It is very difficult to measure *in vivo* all the parameters necessary to build this model. The values of the parameters were collected from various published sources and consequently the inputs of the model were obtained from various different persons.

Defining normality of blood flow in human circulation is rather difficult because clinical measurements show a high degree of variability between persons and even from the same person at different times. This differences are probably the result of biological variation, body size, vasomotor state and blood pressure [Milnor 1989].

As a consequence the pattern of normality is generally a broad one but with some characteristics being common to a large percentage of the persons with normal cardiovascular systems.

Since there is no person whose physiological characteristics correspond to those used to implement the model, it is not possible to make direct measurements in the system being modelled to compare with the outputs of the SPICE model. Thus, the validation of our model cannot be a direct quantitative one, it must, of necessity, be qualitative.

3.5.1 The complete model

The schematic of the complete model implemented in SPICE is shown in figure 3.7. Pressure and flow may be monitored at any point in the model. However, in order to validate the model four points for which published information on these variables is available were chosen. The pressure and flow waveforms measured in the model were also used to compute the input impedance and the PI index at any of the measuring points.

The positions of the four measuring sites used are marked in figure 3.7; AORT is at the distal end of the abdominal aorta artery, CFA is at the distal end of the common femoral artery, POP is at the distal end of the popliteal artery, and ATA is at the distal end of the anterior tibial artery.

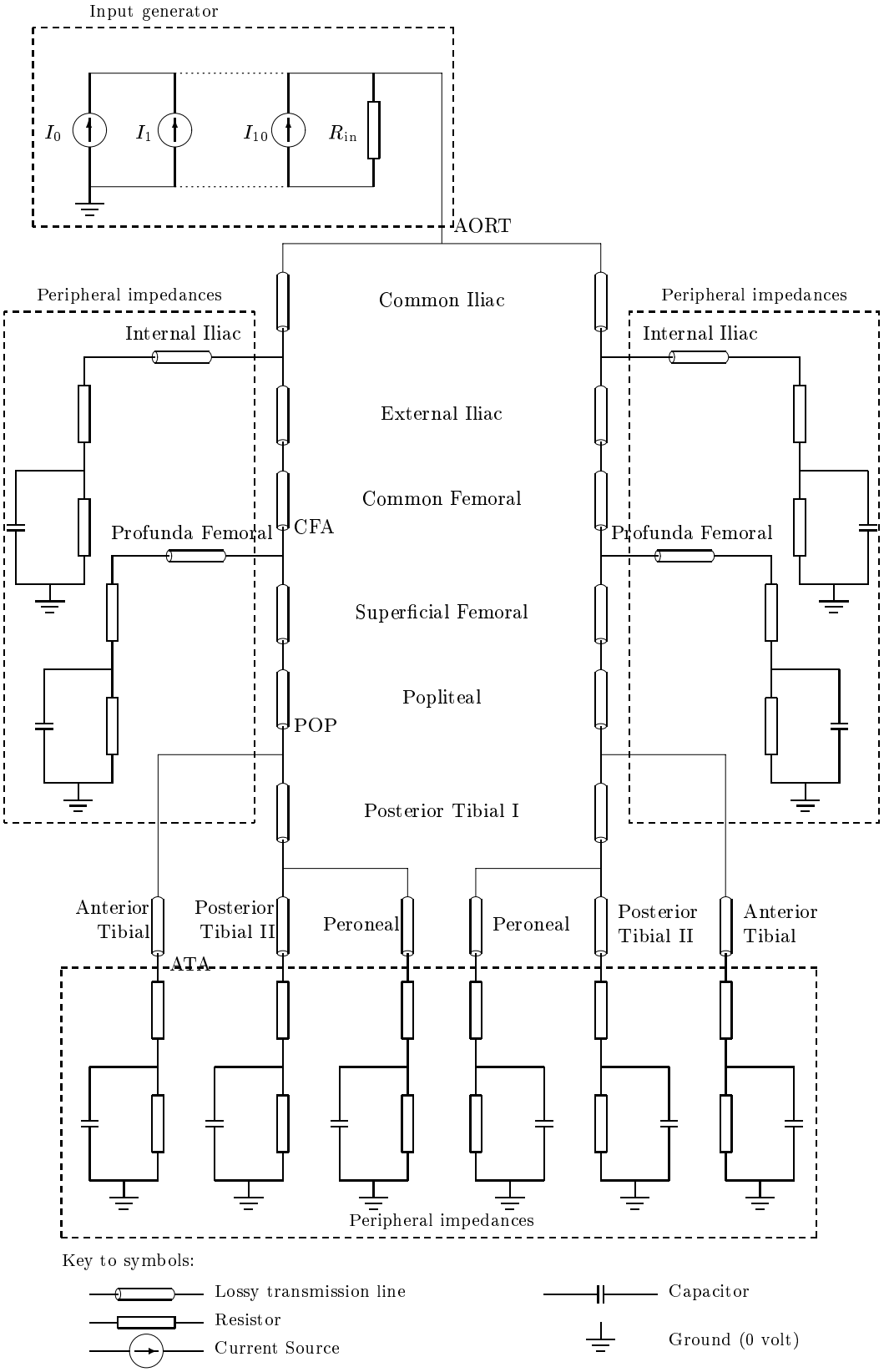

Figure 3.7: Schematic of the electric analogue of the lower limb arterial circulation. Four measuring sites used to monitor the model are marked as: AORT – distal end of abdominal aorta, CFA – distal end of common femoral artery, POP – distal end of popliteal artery, ATA – distal end of anterior tibial artery.

Note that all the arteries were modelled with a lossy transmission line that was implemented in SPICE using the lumped circuit shown in figure 3.5 with 5 sections of lossless transmission line. The only exceptions were the small vessel segments designated as *Posterior Tibial I* that were modelled with a circuit containing only 2 sections of lossless transmission line because the arterial segments are very small (2.5 cm).

3.5.2 Input impedance

Figure 3.8 shows the normalised magnitude and the phase of the femoral input impedance in the model against *in vivo* data [Patel et al. 1965].

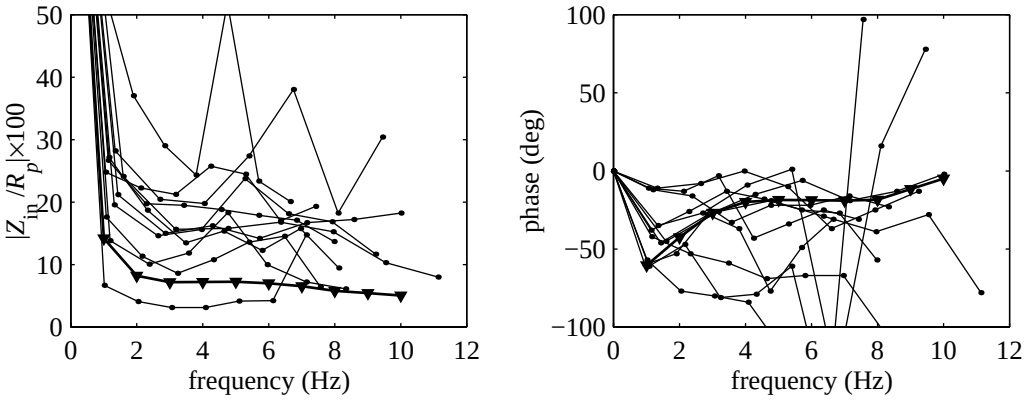

Figure 3.8: Input impedance (normalised magnitude and phase) at the level of the femoral artery in the model (bold line and *blacktriangledown*) and as measured *in vivo* by Patel et al. [1965] in 11 different patients. Z_{in} is the input impedance and R_p is the peripheral resistance, which has a value of 98.5×10^3 dyne s/cm^5 in the model.

The modulus of the femoral input impedance in the model is high for steady flow and decreases significantly to a low value up to 2 or 3 Hz and then remains almost constant for higher frequencies. This is consistent with clinical *in vivo* measurements and within the high variability of the measurements.

The phase of the impedance is negative up to 10 Hz, which is common in the input impedances measured in the leg [Patel et al. 1965] although in some cases the phase may cross the zero level and become positive as illustrated by the clinical data in figure 3.8.

3.5.3 Pressure and flow waveforms

It is known that the amplitude of the pressure pulse increases as it travels to the periphery [Milnor 1989]. The shape of the pressure wave also changes as it moves to the periphery, the pressure rises more steeply in the early stages of systole and the second peak becomes more prominent.

Figure 3.9 shows the pressure waveforms at 4 measuring sites in the lower limb. The 4 measuring sites are those marked in the model diagram shown in figure 3.7 with the acronyms AORT, CFA, POP and ATA.

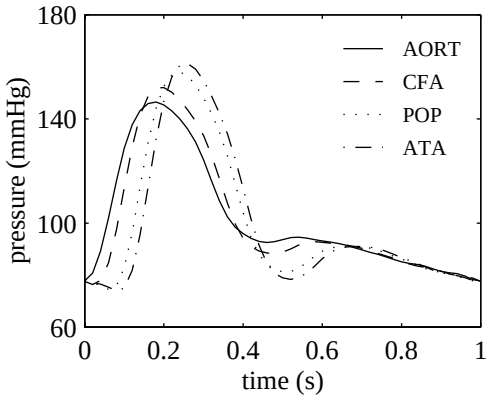

Figure 3.9: Pressure waveforms at the 4 measuring sites in the model; AORT - distal end of abdominal aorta, CFA – distal end of common femoral artery, POP – distal end of popliteal artery, ATA – distal end of anterior tibial artery.

As can be seen from figure 3.9 the amplitude of the pressure pulses generated by the model increases as it travels to the periphery and the second peak becomes more marked. This is similar to what has been observed *in vivo* [Milnor 1989].

Figure 3.10 shows the pressure waveforms measured in the femoral artery and distal end of the anterior tibial artery for a young adult [Kroecker & Wood 1955] as well as the corresponding curves in the model.

As can be seen from figure 3.10 the shape of the pressure waveform generated by the model is similar to those obtained *in vivo* from the corresponding arteries.

As blood travels to the periphery it divides between the various vessels and as a consequence the flow in more peripheral vessels is lower than in the more central ones.

Figure 3.11-a) shows the flow waveforms generated by the model at the 4 measuring sites and figure 3.11-b) shows the variation of the mean volumetric flow compared with clinical data [Holland et al. 1998].

As expected, the mean volumetric flow decreases as the blood moves to the periphery. The mean values for the flow generated by the model for the CFA and POP are in the lower end of the range of measurements made by Holland et al. [1998] , this probably means that the mean flow (15 cm^3/s) assumed for the input flow waveform was too small and/or the percentage (50%) of flow assumed to branch off at the iliac bifurcation was to high.

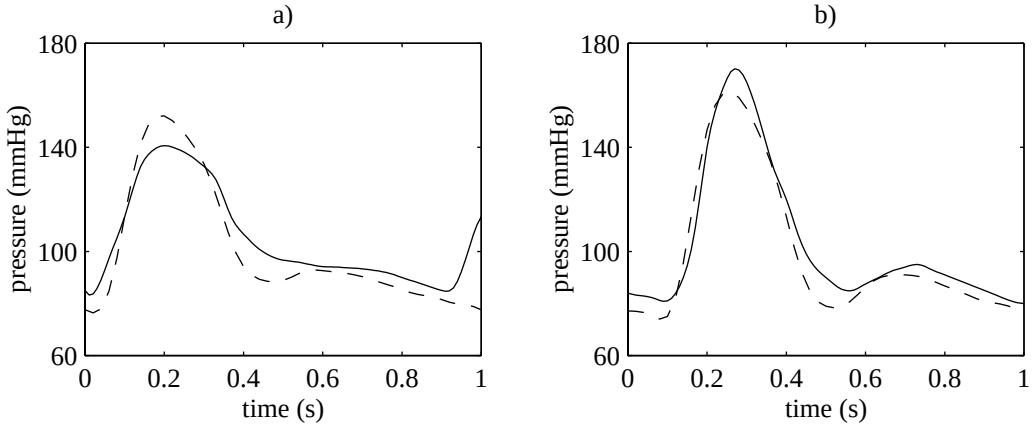

Figure 3.10: Comparison of the model pressure waveforms with pressure waveforms obtained in a normal young adult [Kroecker & Wood 1955]. The solid line represents the clinical data and the dashed line the model data; a) femoral pressure, b) pressure at the distal end of anterior tibial artery. Note that the heart rates corresponding to the model and the clinical data are different.

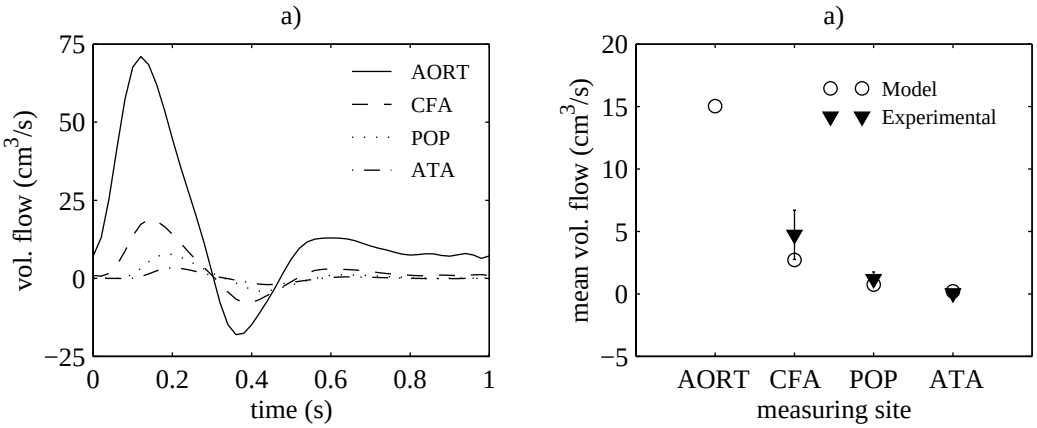

Figure 3.11: a) Volumetric flow waveforms at the 4 measuring sites in the model; AORT - distal end of abdominal aorta, CFA – distal end of common femoral artery, POP – distal end of popliteal artery, ATA – distal end of anterior tibial artery. b) Mean volumetric flow at the same sites. The experimental values were measured by Holland et al. [1998] and are represented by the sample mean, ▼, and the standard deviation of the measurements (vertical bars).

3.5.4 Pulsatility Index

The pulsatility index (PI) defined by (3.1) has been used for a long time as an aid in the diagnosis of arterial stenosis specially in the lower limb [Gosling 1976, Holland et al. 1998, Johnston et al. 1978, Johnston et al. 1984].

In persons with no arterial disease the PI usually increases toward the periphery being progressivly higher in the femoral, popliteal and pedal arteries [Johnston et al. 1978]. When a stenosis is present in an arterial segment of the lower limb the PI is usually reduced distally and sometimes even before the stenosis. This is the result of dampening of the flow waveform.

In our model for the normal hemodynamic state the PI increases as the flow waveform travels to the periphery. Figure 3.12-a) shows the mean velocity waveforms along the lower limb and figure 3.12-b) the variation of the model PI along the lower limb compared with experimental values [Holland et al. 1998].

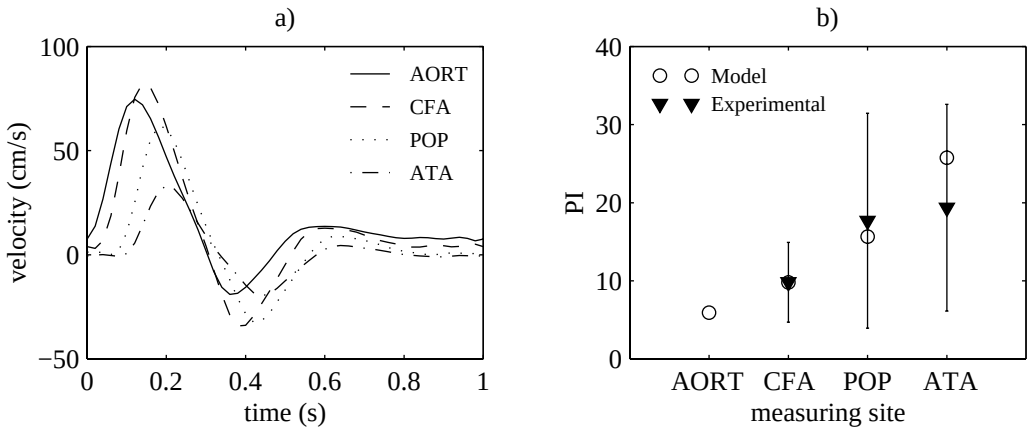

Figure 3.12: a) Mean blood velocity waveforms at the 4 measuring sites in the model; AORT - distal end of abdominal aorta, CFA – distal end of common femoral artery, POP – distal end of popliteal artery, ATA – distal end of anterior tibial artery. b) The pulsatility index at the same sites. The experimental values of PI are from [Holland et al. 1998] and are represented by the sample mean, ▼, and the standard deviation of the measurements (vertical bars).

As can be seen from figure 3.12-b) the PI obtained from the model is within one standard deviation of the mean of the values measured experimentally.

During the development of the model it was found that the PI in the lower limb vessels (specially in the more peripheral ones) depends heavily on the 'leakage' flow that leaves the arteries through the arterial wall and lateral branches. The 'leakage' conductance affects mainly the DC (Direct Current) component of the flow waveform because the peripheral resistance is much higher than the other frequency components of the peripheral impedance; in fact the peripheral impedances are almost matched loads for the transmission lines. Consequently, the mean value of the flow waveform decreases more than the pulsatile component and the PI increases.

3.6 Stenoses

The blood flow model described in this work generates simulated pressure and flow waveforms of a human being with a normal lower limb circulation. It would be interesting to include in

the model the possibility of modelling diseased states, in particular stenoses.

Although we did not implement a model for stenoses we would like to describe one possibility for modelling the blood pressure drop at a stenosis.

The pressure drop at a stenosis is higher than in the unobstructed vessel. Young and associates (see for example [Roth et al. 1976, Young & Tsai 1973*a*, Young & Tsai 1973*b*, Young 1979]) have investigated the flow characteristics in stenosis and found that the pressure drop, Δp, across a stenosis may be estimated with,

$$\Delta P = R_v\, Q + B_t\, |Q| Q + L_\mu \frac{\partial Q}{\partial t} \tag{3.6}$$

where Q is the blood flow in the unobstructed vessel and R_v, B_t and L_μ are parameters that depend on the geometry and severity of the stenosis. The first term on the right of (3.6) represents the pressure drop due to viscous effects, the second term represents the nonlinear effects associated with the convergence and divergence of the flow in stenosis and turbulence, and the third term represents the pressure differential needed to accelerate the fluid.

Equation (3.6) may be simulated in SPICE by an electric circuit as shown in figure 3.13.

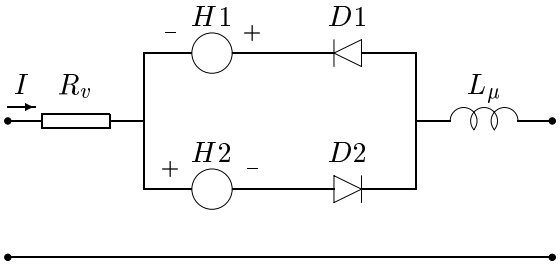

Figure 3.13: Electric schematic of a model for the pressure drop at a stenosis. R_v is a resistor, L_μ is an inductor, $D1$ and $D2$ are ideal diodes, and $H1$ and $H2$ are current controlled voltage sources whose voltage is $V = B_t\, |I| I$.

The diodes $D1$ and $D2$ select one of the voltage sources so that the pressure drop is in the correct direction.

3.7 Concluding remarks

In this Chapter we described the development of an electric analogue model for the flow of blood in the human lower limb circulation.

Due to the complexity of blood flow some simplifying approximations had to be made, examples of such approximations are considering the circulatory system as being linear and the blood flow as laminar and axysimmetric.

Another problem was the sparse data on the vascular tree characteristics available in

the literature and the numerous iterations needed to adjust the model parameters. This is common with models of biological systems, as Milnor [1989, p. 177] says referring to the development of mathematical models for vascular beds and to the comparison of model results with experimentally observed data, "Certain discrepancies usually appear, and the parameters of the model are then adjusted until it is consistent with as many of the experimentally known facts as possible. Most investigators would agree that reasonable guesses play a significant role in this final process of fine-tuning."

It is remarkable that in spite of all the approximations and assumptions made the pressure and flow waveforms resemble so closely the waveforms obtained in the arterial tree.

The model described in this Chapter is an important part of the overall model for the process of generation of the Doppler ultrasonic signal backscattered by blood cells. The model relates the vascular tree characteristics to the blood velocity field.

Chapter 4

Doppler ultrasound signal model

4.1 Introduction

The frequency content of the Doppler power spectrum is determined by several factors [Jones 1993]: blood scattering characteristics, blood velocity field, sample volume characteristics, range of velocities passing through the sample volume and spectral estimation method used. Some these factors are inherent to the Doppler signal generation process while others are introduced by the measuring system.

The Doppler ultrasound signal backscattered from moving blood is a very complex one as pointed out in chapter 2. The signal is pulsatile due to the pumping action of the heart and the signal is random because it results from the scattering of the ultrasonic field from a large number of red blood cells. Branching, curving and tapering of the blood vessels and the presence of disease induced turbulence only add to the signal's complexity. The variability of the Doppler signal obtained from different patients, or from the same patient at different times, greatly contributes to the difficulty in relating the signal characteristics to the blood flow.

In spite of the complexity of the Doppler signal Doppler ultrasound systems have successfully detected moderate to severe arterial stenoses. The lower limit of percentage of stenoses that can be detected depends on the sensitivity of the system to small blood flow disturbances. A better understanding of the Doppler process and quantification of the various factors determining the Doppler spectrum is needed to allow the development of more sensitive systems [Fish 1992].

In order to be able to study the influence of various factors on the spectrum of the Doppler signal we have developed a model of the Doppler signal backscattered from pulsatile laminar flow. The model described in this chapter considers the Doppler signal as resulting from the summation of the signals backscattered from small elemental volumes passing through the instrument's sample volume. The signal from each elemental volume arises from the fluctuations in local density and compressibility of blood.

The model improves our understanding of the Doppler signal generation process and allows the generation of simulated signals with known characteristics so that experiments can be carried out under controlled conditions.

As mentioned in Chapter 2 various models have been proposed for the Doppler ultrasound signal. Some of those models need *a priori* knowledge of the Doppler spectrum (for example [Mo & Cobbold 1989, van Leeuwen et al. 1986]) and do not directly relate the Doppler instrument characteristics to the simulated signal. Wendling et al. [1992] proposed a time-domain model for simulating Doppler signals from pulsatile nonuniform blood flow, their model provided additional insight into the effect of transit time broadening and allowed time-varying flow. It was difficult to use the model to study the effect of blood acceleration on the Doppler spectrum and the triangular shape of the sample volume reduced its usefulness.

Our model was based on previous models proposed by [Mo & Cobbold 1992] and [Wendling et al. 1992] and introduced a new formulation for the Doppler signal that allowed to study the effects of blood acceleration and sample volume shape on the Doppler spectrum. The new formulation allowed also the derivation of a simple formula for estimating the width of the Doppler spectrum. Previous models of the Doppler ultrasound signal are described in more detail in Chapter 2.

4.2 Model description

The Doppler signal can be conceived as the summation of the contribution of all scatterers passing through the sample volume [Fish 1986]. Since the exact movement of each scatterer is not know nor measurable it is impossible to simulate the Doppler signal without simplifying the problem.

To reduce the complexity of the problem we divided the blood vessel into small elemental volumes by making the following assumptions about the flow similar to those used by Fish [1986]:

- the blood velocity is parallel to the vessel wall;
- the blood vessel is a cylindrical rigid tube;
- neighbouring scatterers have similar velocities and can be grouped into an elemental volume;
- the pulse wave velocity of the blood velocity wave is sufficiently high such that at any time instant the instantaneous velocities of all the elemental volumes within an elemental tube and within the sample volume can be considered equal.

That this latter assumption is justified can be seen by considering elements at either extreme of the sample volume. The difference in blood velocity at these extremes is ad/c_0

where a is the local blood acceleration, d is the distance across the sample volume along the elemental tube and c_0 is the pulse wave velocity. This assumption is then:

$$ad/c_0 \ll v$$

where v is the blood velocity. For example an extreme case, with $c_0 = 10\ \mathrm{m\,s^{-1}}$, $a = 30\ \mathrm{m\,s^{-2}}$ and $d = 5$ mm the above inequality becomes $v \gg 1.5\ \mathrm{cm\,s^{-1}}$ and it is clear that the assumption is valid for most conditions in practice.

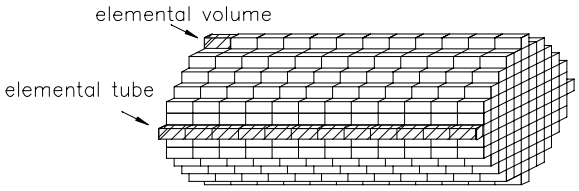

Figure 4.1: Subdivision of the vessel into elemental volumes and elemental tubes.

Figure 4.1 shows how the vessel was divided into elemental volumes and tubes. All the elemental volumes have the same size but the relative position of the elemental volumes of different tubes is not constant because different tubes may have different velocity waveforms. The division of the sample volume is similar to that used by Mo & Cobbold [1992] but in their model the elemental volumes are static while in this model the elemental volumes move across the sample volume.

4.2.1 Signal from a single scatterer

The Doppler signal backscattered by a single scatterer travelling along trajectory $\vec{r}(t)$ passing through a plane wave unit-amplitude infinite wide ultrasonic field is given by:

$$d_{id}(t) = \sqrt{\sigma_{bs}}\, e^{-j\left(2\,\vec{k}\cdot\vec{r}(t)+\phi\right)} \tag{4.1}$$

where d_{id} is the analytic Doppler signal (in phase and quadrature signals), σ_{bs} is the backscattering cross-section of the particle, $\vec{k}$ is the wave vector, t represents time, ϕ is a phase term that depends on the time origin, $\vec{k}\cdot\vec{r}(t)$ is the inner product between $\vec{k}$ and $\vec{r}(t)$, and j is the imaginary unit number. The minus sign in the exponent of e arises from the convention that scatterers travelling in the positive direction are moving away from the transducer and consequently produce negative frequency shifts.

Since infinite wide ultrasonic fields are not feasible in practice, the backscattered signal is amplitude modulated by the beam pattern across the scatterer's trajectory. So a better approximation to the Doppler signal from a single particle under plane wave conditions and

not taking attenuation into account is given by:

$$d(t) = d_{id}(t)G\big(\vec{r}(t)\big) \tag{4.2}$$

where $G\big(\vec{r}(t)\big)$ represents the sensitivity (combining transmitter and receiver sensitivities) of the ultrasonic beam across the scatterer's path, $\vec{r}(t)$, through the sample volume and includes the effect of the demodulator filter. Note that in general $G\big(\vec{r}(t)\big)$ is complex and incorporates a phase term describing the deviation from plane-wave conditions [Fish 1986].

Figure 4.2 shows an example of the Doppler signal generated by a single scatterer passing with constant velocity through an ultrasonic field whose sensitivity is Gaussian along the scatterer's trajectory.

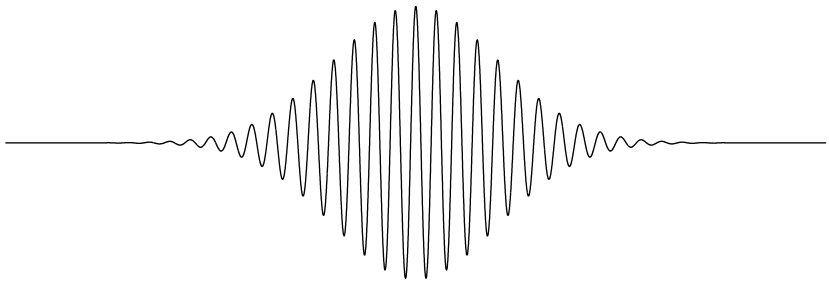

Figure 4.2: Doppler signal from a single scatterer travelling with constant velocity through an ultrasonic field with Gaussian sensitivity.

4.2.2 Signal from an elemental volume

To simulate the Doppler signal from an elemental volume we further assume that:

- multiple scattering does not contribute to the signal, i.e. only the signals scattered directly from the incident wave are considered;
- the amplitude and phase of the backscattered signal from an elemental volume are random and depend only on the random fluctuation in the local mass density and compressibility of the red blood cells [Angelsen 1980];
- the amplitude of the signal from an elemental volume is constant while travelling through the sample volume;
- the sample volume is in a region where the ultrasonic signal is approximately a plane wave.

The co-ordinate systems of the beam and vessel are defined in figure 4.3.

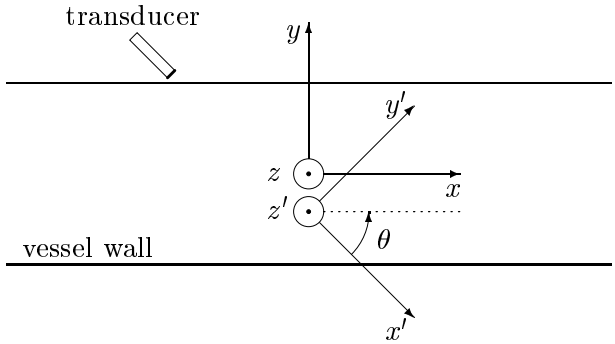

Figure 4.3: Geometry and coordinate systems for the beam/vessel arrangement (x, y, z for the vessel and x', y', z' for the beam), the origins O and O' are in a plane perpendicular to the vessel which includes the centre of the beam sample volume, the axes z and z' are parallel and point out of the diagram plane.

Under these assumptions the contribution to the Doppler signal from an elemental volume m in tube q is,

$$u_{qm}(t) = A_{qm}\, e^{-j(2\cos(\theta)kx_{qm}(t)+\phi_{qm})} G_{qm}(t) \tag{4.3}$$

where:

$$G_{qm}(t) = G\left(x_{qm}, y_{qm}, z_{qm}\right) \tag{4.4}$$

and where A_{qm} and $-\phi_{qm}$ represent respectively the random amplitude and initial phase, at $t = 0$, of the signal from elemental volume qm, k is the modulus of the wave vector, θ is the angle between this wave vector and the direction of movement, (x_{qm}, y_{qm}, z_{qm}) is the position of the elemental volume in the vessel coordinate system at any time and $G(.)$ is the variation in sensitivity within the instrument's sample volume. Note that for streamline flow x_{qm} (but not y_{qm} and z_{qm}) is a function of time.

If the flow is steady then:

$$x_{qm}(t) = v_{qm}t + x_{qm0} \tag{4.5}$$

where v_{qm} is the velocity of the elemental volume, x_{qm0} is the position at $t = 0$ and

$$u_{qm}(t) = A_{qm}e^{-j(\omega_d t+\phi_{1qm})} G_{qm}(t) \tag{4.6}$$

where $\phi_{1qm} = \phi_{qm} + 2\cos(\theta)kx_{qm0}$,

$$\omega_d = \frac{2v\cos(\theta)}{c}\,\omega_0 \tag{4.7}$$

is the angular Doppler frequency, ω_0 is the angular transmitted frequency and c is the ultrasound propagation speed. However, if the flow is time-varying then we should write:

$$x_{qm}(t) = x_{qm}(t_r) + \int_{t_r}^{t} v_{qm}(\tau)\, d\tau \tag{4.8}$$

where t_r is any fixed reference time, and calculate the Doppler signal from (4.3) and (4.8).

The Doppler signal $s_q(t)$ from an elemental tube, q, is obtained by adding the contribution from all its elemental volumes that pass through the sample volume,

$$s_q(t) = \sum_m A_{qm}\, e^{-j(2\cos(\theta)kx_{qm}(t)+\phi_{qm})} G_{qm}(t) \tag{4.9}$$

The Doppler signal from the complete sample volume is simply the summation of the signals from all its elemental tubes,

$$s(t) = \sum_q \sum_m A_{qm}\, e^{-j(2\cos(\theta)kx_{qm}(t)+\phi_{qm})} G_{qm}(t) \tag{4.10}$$

The implementation of the model described here uses planewave conditions throughout the sample volume (as is approximately true in the vicinity of the focus of a focused transducer, including one with Gaussian appodisation (see for example [Ata & Fish 1991, Filipczyński & Etienne 1972]) and a Rayleigh random variable (RV) for the signal amplitude with the initial phase given by a random variable uniformly distributed in the interval [0–2π). As a result, the signal received from an elemental volume is a Gaussian stochastic process.

Note that the results presented here will not be significantly affected by the assumption of particular element signal statistics as a result of the relatively large number of elemental volumes used to calculate Doppler signal and the Central Limit Theorem.

4.3 Ensemble averaged Doppler spectrum

We have seen that the Doppler signal from a single elemental tube is given by equation (4.9). In order to estimate the time-varying spectrum of the Doppler signal at a particular time we multiply the signal by a window function $w\,(t - t_w)$ centred at time t_w.

Assuming A_{qm} and ϕ_{qm} constants during the passage of the elemental volume through the sample volume, the expected energy spectrum of the windowed signal at time t_w from a single streamline is then:

$$S_q\,(\omega, t_w) = E\left\{ \left| \int_{-\infty}^{\infty} \sum_m A_{qm}\, e^{-j\,(2\cos(\theta)kx_{qm}(t)+\phi_{qm})} G_{qm}(t)\, w\,(t - t_w)\; e^{-j\,\omega t}\, dt \right|^2 \right\} \tag{4.11}$$

where $E\{.\}$ is the expectation operator.

Since A_{qm} and ϕ_{qm} do not depend on t we can re-write (4.11) by changing the order between the summation and the integral, giving:

$$S_q(\omega, t_w) = E\left\{ \left| \sum_m A_{qm}\, e^{-j\,\phi_{qm}} \overbrace{\int_{-\infty}^{\infty} e^{-j\,2\cos(\theta)kx_{qm}(t)}\, G_{qm}(t)\, w(t-t_w)\, e^{-j\,\omega t}\, dt}^{F_{qm}(\omega,t_w)} \right|^2 \right\} \quad (4.12)$$

if for each m the integral

$$F_{qm}(\omega, t_w) = \int_{-\infty}^{\infty} e^{-j\,2\cos(\theta)kx_{qm}(t)}\, G_{qm}(t)\, w(t-t_w)\, e^{-j\,\omega t}\, dt \quad (4.13)$$

exists, the corresponding power spectrum is:

$$\begin{aligned} S_q(\omega, t_w) &= E\left\{ \Big(\sum_m A_{qm}\, e^{-j\,\phi_{qm}} F_{qm}(\omega, t_w) \Big) \times \Big(\sum_r A_{qr}\, e^{-j\,\phi_{qr}} F_{qr}(\omega, t_w) \Big)^* \right\} \\ &= E\left\{ \Big(\sum_m A_{qm}\, e^{-j\,\phi_{qm}} F_{qm}(\omega, t_w) \Big) \times \Big(\sum_r A_{qr}\, e^{j\,\phi_{qr}} F^*_{qr}(\omega, t_w) \Big) \right\} \end{aligned} \quad (4.14)$$

which can be re-written as,

$$\begin{aligned} S_q(\omega, t_w) = E\Bigg\{ & \sum_m A^2_{qm} F_{qm}(\omega, t_w) F^*_{qm}(\omega, t_w) \\ & + \overbrace{\sum_{m,r} A_{qm}\, e^{-j\,\phi_{qm}} F_{qm}(\omega, t_w) \times A_{qr}\, e^{j\,\phi_{qr}} F^*_{qr}(\omega, t_w)}^{m \neq r} \Bigg\} \end{aligned} \quad (4.15)$$

Since the expectation of the product of uncorrelated zero mean random processes is zero [Papoulis 1991], the expected value is simply the expectation of the first right hand side term.

$$S_q(\omega, t_w) = E\left\{ \sum_m A^2_{qm} F_{qm}(\omega, t_w) F^*_{qm}(\omega, t_w) \right\} \quad (4.16)$$

which may be simplified to [Papoulis 1991]:

$$S_q(\omega, t_w) = \sum_m S_{qm}(\omega, t_w) E\{A^2_{qm}\} \quad (4.17)$$

and assuming that the statistics are invariant along an elemental volume,

$$S_q(\omega, t_w) = A^2_q \sum_m S_{qm}(\omega, t_w) \quad (4.18)$$

where $A^2_q = E\{A^2_{qm}\}$.

Since the signals from different elemental tubes are zero-mean uncorrelated random processes, the ensemble averaged power spectrum from the complete sample volume is simply

the summation of the power spectra from all the elemental tubes

$$S(\omega, t_w) = \sum_q A_q^2 \sum_m S_{qm}(\omega, t_w) \tag{4.19}$$

If we consider that the random fluctuations in local density and compressibility are independent of radial position then $A_q^2 (= A)$ is equal for all elemental tubes and the expected value for the ensemble averaged energy spectrum of the windowed Doppler signal may be expressed as:

$$S(\omega, t_w) = A^2 \sum_q \sum_m S_{qm}(\omega, t_w) \tag{4.20}$$

We note that A_q^2 does depend on flow conditions [Bascom et al. 1988, Cloutier & Shung 1993, Mo & Cobbold 1992, Wu & Shung 1996] and the approximation that this is constant may have to be revisited when more is known. Limiting the range of velocities within the sample volume (small sample volume and/or blunt profile) will increase the validity of the above assumption.

4.4 Time-varying blood velocity profiles

For pulsatile blood flow the calculation of the position function for each elemental tube involves the computation of the time varying velocity profile. If the spatial mean velocity waveform $\overline{v}(t)$ is assumed to be periodic then it can be expressed as a Fourier cosine series,

$$\overline{v}(t) = v_0 + \sum_{p=1}^{\infty} v_p \cos\left(p\,\omega_1 t + \epsilon_p\right) \tag{4.21}$$

where v_p and ϵ_p are the amplitude and phase of the pth harmonic of the fundamental angular frequency ω_1. Assuming that blood is a Newtonian incompressible fluid and that the flow is fully established, Evans [Evans 1982*a*] extended Womersley theory and showed that the velocity profile for pulsatile periodic flow in a cylindrical rigid tube is given by,

$$v(y_1, t) = 2v_0\left(1 - y_1^2\right) + \sum_{p=1}^{\infty} v_p \left|\Psi_p(y_1)\right| \cos\left(p\,\omega_1 t + \epsilon_p + \chi_p(y_1)\right) \tag{4.22}$$

$$\Psi_p(y_1) = \tau_p \frac{J_0(\tau_p) - J_1(y_1\tau_p)}{\tau_p J_0(\tau_p) - 2J_1(\tau_p)} \qquad , \tau_p = \alpha_p j^{3/2} \tag{4.23}$$

where $y_1 = r/R_0$, $\alpha_p = R_0\sqrt{p\,\omega_1/\nu}$ is the Womersley parameter, r is the radial co-ordinate, R is the vessel radius, ν is the kinematic viscosity of blood, J_0 and J_1 are Bessel functions of the first kind and orders 0 and 1, and χ_p is the phase of Ψ_p.

Expressions for the pulsatile periodic velocity profiles were already introduced in Chapter 2, (2.11) and (2.12). For rigid circular arteries the mean spatial velocity is equal to the

mean volumetric flow divided by the vessel area, πR_0^2.

The position function of any elemental volume, $x_{qm}(t)$, is computed by using (4.8) where the velocity waveform, $v_{qm}(t)$, is computed using (4.22) and y_1 is the distance of elemental tube q to the centre of the vessel.

Figure 4.4 shows the velocity profile of the blood flow in a common femoral artery in order to illustrate the time-varying nature of the velocity profile in pulsatile flow. The velocity profile was computed using equations (4.21–4.23) and the cosine series coefficients were taken from [Evans et al. 1989].

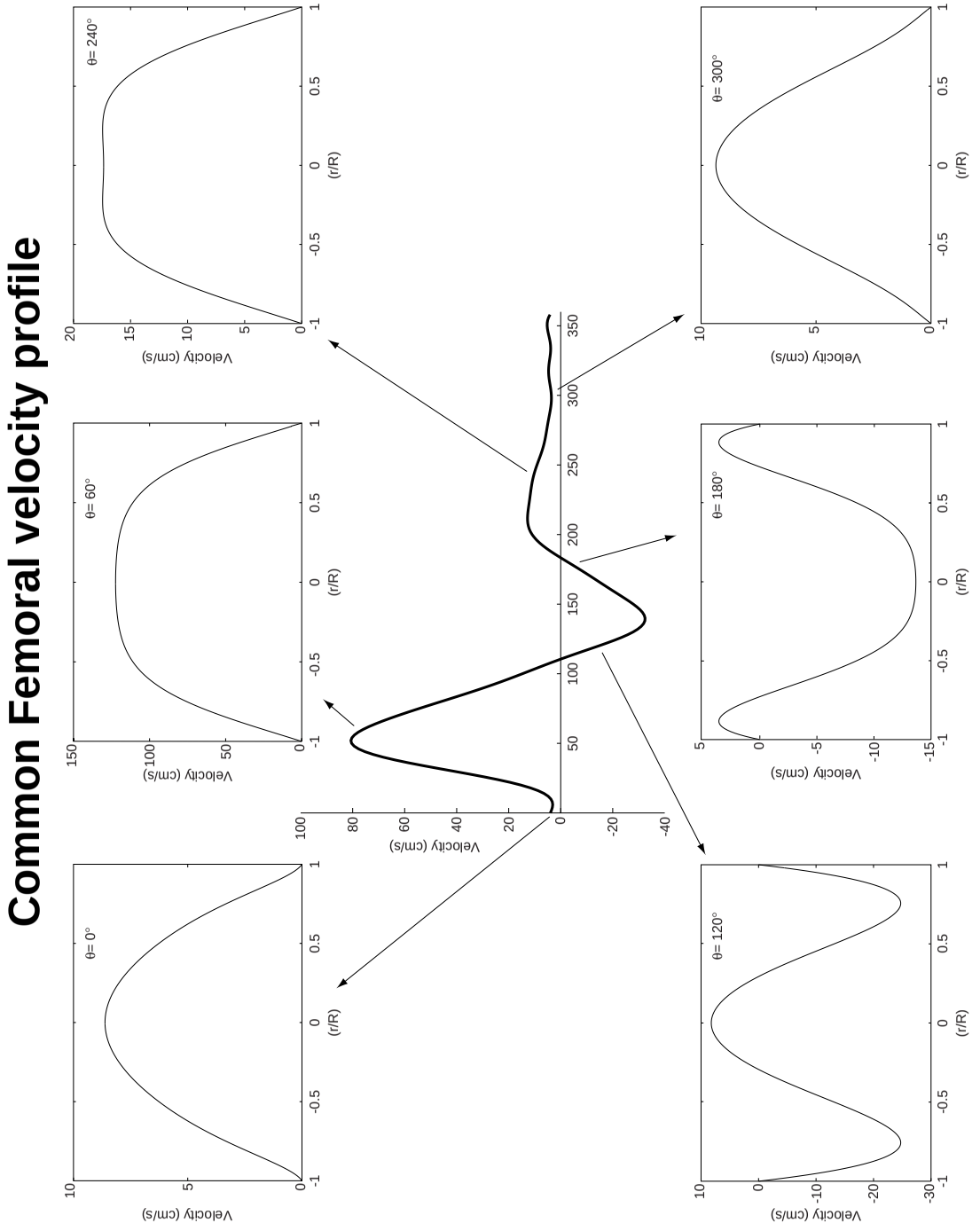

Figure 4.4: Velocity profile of blood flow from a normal common femoral artery evaluated at 60^{o} intervals.

4.5 Implementation issues

This section briefly describes how the model for the generation of simulated Doppler signals and spectra was implemented.

The model was implemented in software running on a Unix workstation computer. It was written using MATLAB [Mat 1998] and C [Kernighan & Ritchie 1988] to code the most demanding (in terms of execution time) parts of the model program. Much of the low level implementation details are deliberately omitted because they depend on the software language used and are not relevant for the work being described, a model for Doppler ultrasound signals.

A Gaussian shaped sample volume was implemented but other shapes could easily be implemented. The Gaussian shape was chosen because it is a reasonable approximation of the sample volumes commonly associated with pulsed wave systems [Bascom & Cobbold 1990]. The sensitivity of a Gaussian sample volume may be represented by

$$G'(x', y', z') = \exp\left(-\frac{x'^2}{2\,\sigma_{x'}^2} - \frac{y'^2}{2\,\sigma_{y'}^2} - \frac{z'^2}{2\,\sigma_{z'}^2}\right) \tag{4.24}$$

where $\sigma_{x'}, \sigma_{y'}$ and $\sigma_{z'}$ are the root mean square (rms) widths of the beam sensitivity along the x', y' and z' axes respectively (figure 4.3). The signal from an elemental volume was only considered for the positions, (x, y, z), where $G_{qm}(x, y, z) \geq \exp(-8)$.

Two basic modes of operation of the model were implemented; one to generate simulated Doppler signals and another mode to generate the expected power spectrum.

In the implementation of both modes of operation $v_{qm}(t)$, $x_{qm}(t)$ and $G_{qm}(t)$ were calculated in the same way. When the model was used to generate simulated signals from blood moving with a periodic velocity, the velocity of each flow streamline, $v_q(t)$, was computed using equations (4.21–4.23) and in other cases (e.g. parabolic blood flow) the velocity waveform of each streamline was computed using the equation of the velocity profile. The position of each elemental volume, $x_{qm}(t)$, was then computed from the velocity of the streamline and equation (4.8). $G_{qm}(t)$ was then computed from $x_{qm}(t)$ and the definition of the sample volume shape (equation 4.24 for a Gaussian sample volume).

The model then used $x_{qm}(t)$, $G_{qm}(t)$ and the other characteristics of the beam and the vessel to either generate simulated Doppler signals using equation (4.10) or the expected power spectrum using equations (4.12), (4.13), and (4.20)

Spatial and temporal sampling

In order to compute the simulated signals from each streamline the vessel cross-section was divided into streamlines with a square section. This type of spatial sampling of the vessel cross-section is illustrated in figure 4.5.

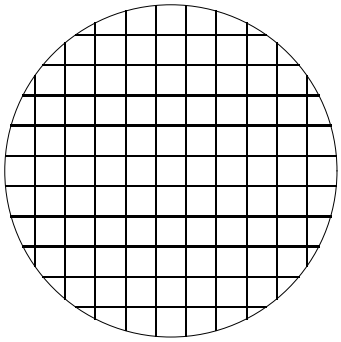

Figure 4.5: Division of the vessel cross-section with a grid of square sections.

For large sample volumes the use of a square grid to sample the vessel cross-section results in very long run times of the computer program due to the large number of streamlines. When both the sample volume and the velocity profile are axis-symmetric, a circular grid may be used in order to significantly reduce the execution time of the computer program. When the circular grid is used the signal from each flow shell is computed as the signal from a streamline in the shell multiplied by the area of the flow shell cross-section. The signal from the complete sample volume is computed simply as the sum of the signals from all the flow shells.

Figure 4.6 shows an example of the division of the vessel cross-section with a circular grid.

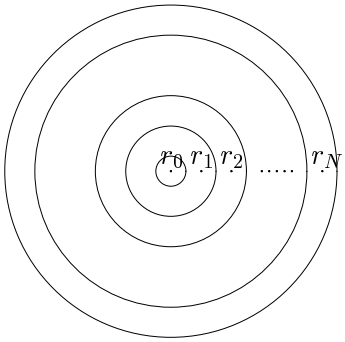

Figure 4.6: Division of the vessel cross-section with a circular grid when both the sample volume and the velocity profile are axis-symmetric.

The area of each flow shell in figure 4.6 is:

$$area_n = \begin{cases} \pi \left(\dfrac{\Delta r}{2} \right)^2 & , n = 0 \\ \\ 2\pi r_n \Delta r & , n = 1, 2, \ldots, N \end{cases} \tag{4.25}$$

where Δr is the constant distance between the centre of the consecutive flow shells; $\Delta r = r_n - r_{n-1}, 1 \leq n \leq N$.

The three dimensions (width and height) of the elemental volumes were set, following a recommendation by Angelsen [1980], to approximately $\lambda/10$ where λ is the wavelength of the transmitted ultrasonic wave. For a 5 MHz wave and assuming that the sound velocity in blood is 1540 m s^{-1} the wavelength is 308 μm and the dimensions of the elemental volumes were set to 30 μm.

The above spatial resolution was sufficient for most experimental simulations, but, as will be seen in the next section, when the sample volume is placed in a region of high velocity gradients the lateral resolution must be higher in order to sample the velocity profile at a sufficient rate.

As was mentioned in Chapter 2 the Doppler signals are normally sampled and processed in a digital computer. The sampling frequency must be at least 2 times the higher frequency of the sampled signal. For convenience a sampling frequency of 25.6 kHz was used so that a typical 10 ms data segment contains 256 samples. The FFT algorithm is significantly faster when the number of samples per data segment is a natural power of 2.

4.6 Simulation experiments

This section presents the results of some experiments that were carried out with the Doppler model described in the previous sections of this chapter. Some of the experiments were carried out to evaluate the quality of the model results, while others serve to show simulated Doppler signals from various places in the lower limb arterial circulation. In the future the model results should also be compared with signals obtained from *in vitro* experiments as a last check on the quality of the model.

4.6.1 Assessment of model results

Unless otherwise stated all the experiments described in this section were carried out with the parameters set above: $f_0 = 5$ MHz; $c = 1540$ m s^{-1}; sampling frequency, 25.6 kHz; elemental volumes with $30 \times 30 \times 30$ μm (length, width, height); and the angle between beam and vessel axis was $\theta = 60^{\circ}$.

Constant velocity

The first experiment carried out in order to assess the model results was the simulation of Doppler signals from a single streamline with constant velocity. Figure 4.7 shows 40 ms of the simulated signal from a single streamline moving at 1 m s^{-1} through a Gaussian sample volume with spherical symmetry, $\sigma'_x = \sigma'_y = \sigma'_z = \sigma_{\text{SV}}$. The sample volume used in this experiment had $\sigma_{\text{SV}} = 1$ mm.

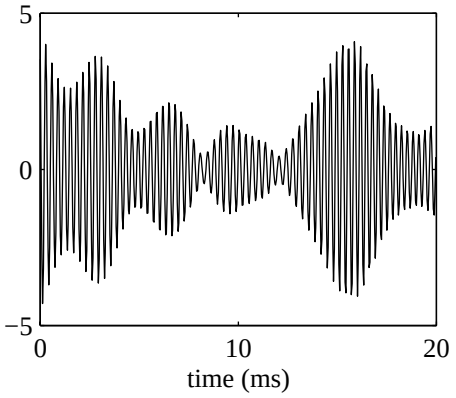

Figure 4.7: Example of 20 ms of the in-phase simulated signal from a single streamline with constant velocity of 1 m s^{-1} passing through the centre of a symmetric Gaussian sample volume with $\sigma_{\mathrm{sv}} = 1$ mm.

Figure 4.8 shows the expected and measured power spectra of the simulated signals from the same experiment that generated the signal shown in figure 4.7. In order to reduce spectral leakage and window broadening, the signal was multiplied by a 'long' (1.28 s) Hanning window.

The theoretically expected power spectrum in figure 4.8 was computed as the square of the Fourier transform of $G_{qm}(t)\, e^{j2\pi f_d t}$, which for a streamline with constant velocity passing

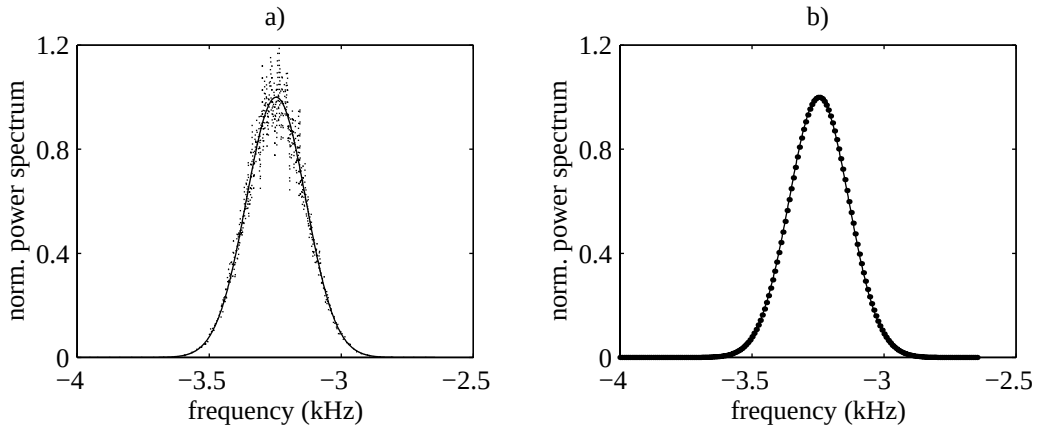

Figure 4.8: Normalised power spectra for the simulated Doppler signals from a single streamline with constant velocity of 1 m s^{-1} passing through the centre of a symmetric Gaussian sample volume with $\sigma_{\mathrm{sv}} = 1$ mm. The solid line represents the expected normalised spectrum in both plots and the dotted line represents: a) ensemble averaged spectrum (100 runs), and b) spectrum computed by the model in spectrum mode of operation (only 1 in every 10 samples of the power spectrum were plotted to allow the visualisation of the solid line).

through a Gaussian sample volume is given by:

$$S_{qm}(f) = K \exp\left(-\frac{(f - f_d)^2}{2\left(\frac{v}{2\sqrt{2}\pi\sigma_{sv}}\right)^2} \right) \tag{4.26}$$

where v is the velocity of the streamline, K is a constant, and f_d is the expected Doppler frequency shift computed with the Doppler equation, (2.37).

As can be seen from figure 4.8-b) the spectrum generated by the Doppler model, in the spectrum mode of operation, agrees very well with the theoretical spectrum. The ensemble averaged spectrum computed from the simulated Doppler signals is close to the theoretical spectrum but it shows some variance. If lower variance is required then a larger number of spectra must be averaged.

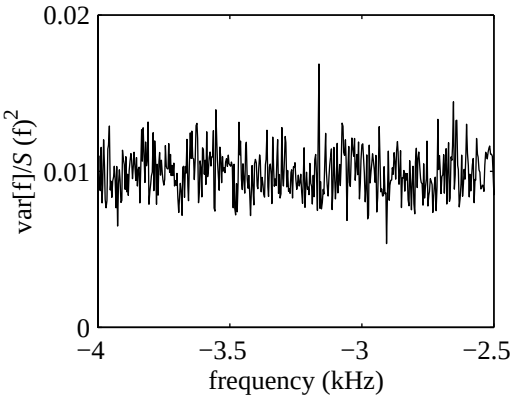

Figure 4.9: Fractional variance of the ensemble (100) averaged spectrum of figure 4.8-a).

Figure 4.9 shows the fractional variance of the 100 ensemble averaged spectrum to illustrate the reduction in spectral variance obtained by averaging the spectra. As expected (see equation 2.56) the fractional variance of the averaged spectrum fluctuates around 1/100. Recall from section 2.4.2 that the fractional variance of the periodogram of a Gaussian stochastic process fluctuates around unity.

Time-varying velocities

In order to assess the ability of the Doppler signal model to generate signals whose mean frequency follows a predetermined waveform two experiments were carried out. In one of the experiments the model was used to simulate signals corresponding to blood accelerating uniformly with time and in the other experiment a typical common femoral waveform was used to drive the model. The details and model parameters used in each experiment are presented below.

In the first of the experiments, the signal was simulated for a single streamline in a symmetric Gassian sample volume with $\sigma_{sv} = 1$ mm, and the velocity varying linearly with time ($v(t) = -0.1 - a\,t$ m s^{-1}) for three blood accelerations, $a = 5$, 10, and 15 m s^{-2}.

Figure 4.10-a) shows the spectrogram of the simulated signal for $a = 10$ m s^{-2}. The spectrogram was computed with 10 ms data segments (Hanning window) with 50% overlap. As expected, the frequency of the spectrogram increases almost linearly with time.

The mean frequency waveform was computed for each of the 10 ms data segments (no overlap) and averaged (100 spectra). The averaged and the expected mean frequency variations are shown in figure 4.10-b) for the three blood accelerations. The close agreement between the expected and measured mean frequency waveforms indicates that our model is capable of simulating Doppler signals whose mean frequency variation follow accurately the mean frequency variation expected for the Doppler signal from blood moving with constant acceleration. Plots comparing the spectral width of the simulated signal with that expected for Doppler signals from blood moving with constant acceleration are presented in section 6.4.1.

The second experiment to assess the ability of the model to simulate time-varying Doppler signal used a typical common femoral artery [Evans et al. 1989, pp. 16, 17] velocity waveform as the input velocity. This experiment also checked the ability of the model to simulate signals with forward and reverse flow.

Figure 4.11 shows the results of this experiment. Except for the velocity waveform and the time duration of the simulated signal all the other parameters of the experiment were the

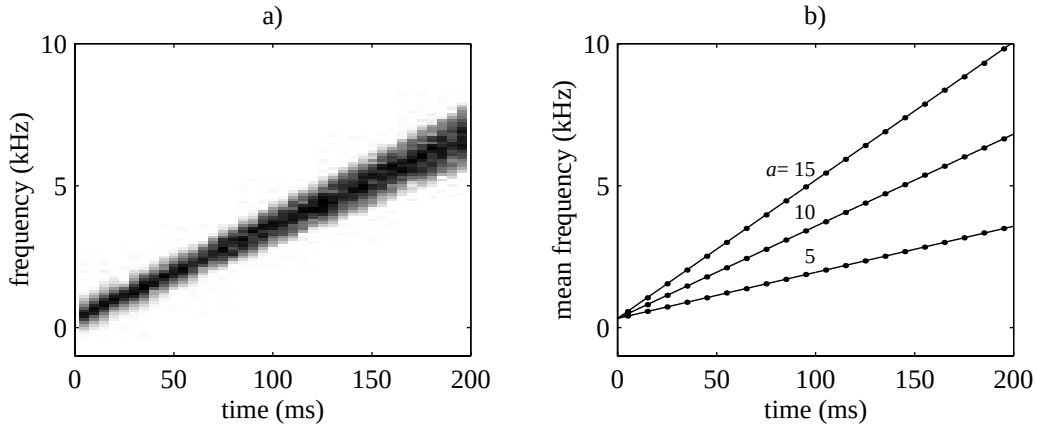

Figure 4.10: Spectrogram and mean frequency time variation of the simulated Doppler signal from a single streamline at the centre of a symmetric Gaussian sample volume, $\sigma_{sv} = 1$ mm and a velocity waveform, $v(t) = -0.1 - a\,t$ m s^{-1}: a) spectrogram of the simulated signal ($a = 10$ m s^{-2}) computed from 10 ms data segments (50% overlap) multiplied by a Hanning window; b) comparison between the expected, ——, and measured mean frequency variation, · · ·, for $a = 5$, 10, and 15 m s^{-2}.

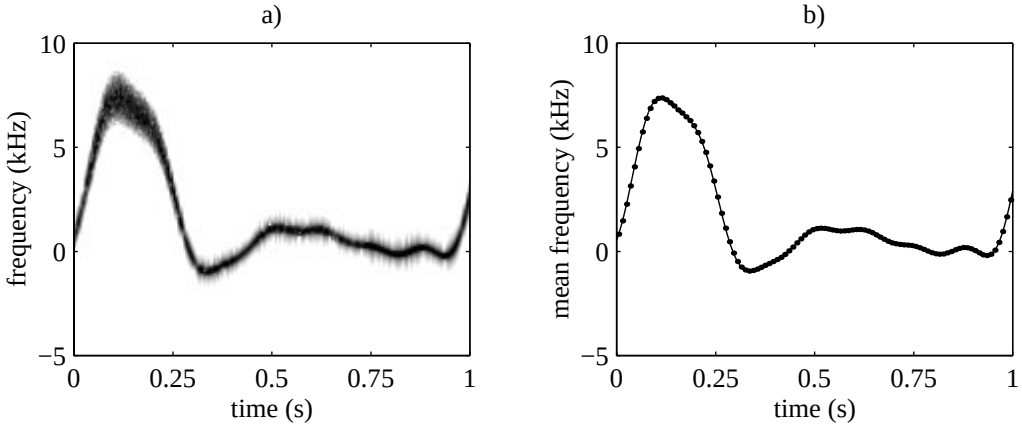

Figure 4.11: Spectrogram and mean frequency time variation of the simulated Doppler signal from a single streamline at the centre of a symmetric Gaussian sample volume, $\sigma_{sv} = 1$ mm, the velocity input was a typical common femoral artery velocity waveform: a) spectrogram of the simulated signal computed from 10 ms non-overlapping data segments multiplied by a Hanning window; b) comparison between the expected, ——, and measured mean frequency variation, · · · .

same as those used to generate figure 4.10.

Once again the average of the mean frequency variation of the simulated signal closely follows the expected mean Doppler frequency waveform.

Parabolic velocity profile under a wide uniform beam

The model results presented previously in this section were all obtained from a single streamline to avoid the influence of velocity profile shape. We present now results from two experiments that used blood flow with a parabolic velocity profile passing through a large Gaussian sample volume.

Figure 4.12 shows the normalised spectra for a parabolic velocity profile, $v(r) = v_0(1 - (r/R_0)^2)$ with $v_0 = 1\,\mathrm{m\,s^{-1}}$, passing through two symmetrical Gaussian sample volumes centred in a vessel with a radius of 4.2 mm. One of the sample volumes had $\sigma_{sv} = 8$ mm (figure 4.12-a) while in the other $\sigma_{sv} = 16$ mm. Large sample volumes were used to reduce the effect of transit time broadening so that the expected spectrum could be predicted using the expressions derived in Chapter 5. The signal was windowed with a 80 ms Hanning window and the vessel cross-section was sampled with a circular grid where each flow shell had a width of 2.5 μm.

The derivation of the theoretical Doppler power spectrum obtained from a power law velocity profile under a Gaussian sample volume is presented in Chapter 5. The expression for the normalised power spectrum from parabolic velocity profile under a symmetric Gaussian

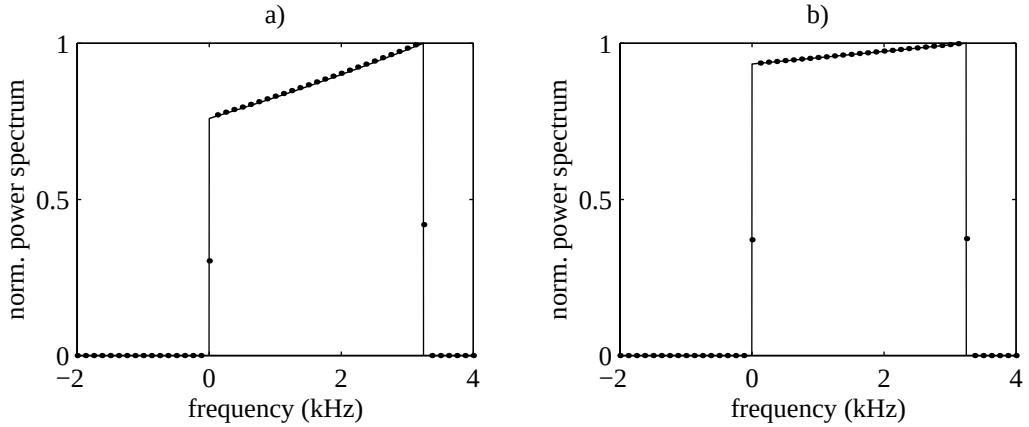

Figure 4.12: Normalised power spectra for parabolic velocity profile, $v(r) = \left(1-(r/R_0)^2\right)$ m s^{-1}, for a vessel with $R_0 = 4.2$ mm. The solid lines represent the theoretical spectra, (4.27), and the dotted lines represent the simulated spectra: a) $\sigma_{sv} = 8$ mm, b) $\sigma_{sv} = 16$ mm. Only 1 in every 10 samples of the simulated spectra is displayed to allow the visualisation of the solid lines. The width of each flow shell is 2.5 μm.

sample volume centred in the vessel is

$$S_{\text{norm}}(\omega) = \exp\left(-\frac{R_0^2}{\sigma_{\text{sv}}^2}\left(1-\frac{\omega}{\omega_{d0}}\right)\right) \tag{4.27}$$

where ω_{d0} is the angular Doppler frequency shift corresponding to the central streamline travelling with velocity v_0. Expression (4.27) was obtained from (5.35) by making the substitution, $n = 2$, and by normalising the spectrum. The experimental spectra were obtained with the model running in the spectrum mode of operation.

As can be seen from figure 4.12 the model generates spectra identical to the theoretical ones for parabolic profiles for large symmetric Gaussian sample volumes.

It is worth mentioning that when simulating spectra from flow with high velocity gradients like those plotted in figure 4.12 the spatial resolution has to be high so that the simulated spectrum does not contain large frequency gaps which result in ripple.

As an example, figure 4.13 shows the simulated spectrum for the same parameters as figure 4.12-b) but with a lower spatial resolution of the sampling grid. The width of each flow shell in this case was 15 μm.

In order to make sure that the spectrum generated by the model has no ripple it is sufficient that the maximum frequency gap between adjacent flow shells is less than the frequency resolution of the spectrum, being the reciprocal of the window duration.

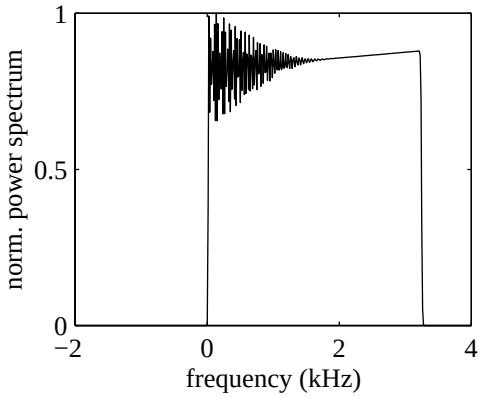

Figure 4.13: Normalised power spectrum for parabolic velocity profile, $v(r) = \left(1-(r/R_0)^2\right)$ m s^{-1}, for a vessel with $R_0 = 4.2$ mm illuminated by a symmetric Gaussian sample volume with $\sigma_{sv} = 16$ mm. The width of the circular grid flow shells is 15 μm.

4.7 Concluding remarks

Due to the complex nature of the Doppler ultrasound signal backscattered by blood, it was necessary to develop a model capable of simulating Doppler signals.

The Doppler signal model described in this chapter uses a new formulation for modelling the Doppler spectrum, which enables to study the effect of the characteristics of the blood velocity measuring system on the Doppler spectrum. One such study is presented in Chapter 6 where the influence of blood acceleration, data window duration and sample volume size on the root mean square width of the Doppler spectrum is analysed.

Since the model generates signals whose characteristics are easily controlled and repeated, its output can be used to carry out experiments under controlled conditions. Thus, the model may be very useful in the development and testing of new signal processing techniques for the Doppler ultrasound signal.

The software implementation of the model has two modes of operation, one to generate simulated random Doppler signals and another to generate the ensemble averaged Doppler spectrum.

In order to assess the model results, the model was used to generate simulated Doppler signals for situations in which its characteristics could be predicted. The model outputs were very similar to those expected.

Although the model results agreed well with the theoretical predictions, it is recognised that the model should be validated experimentally in the future.

In future the model may evolve to simulate Doppler signals from non laminar flow, for example helical flow. The current software implementation may be improved in the future by permitting the simulation of other sample volume shapes and by reducing the execution times.

Chapter 5

Doppler power spectrum due solely to the range of blood velocities passing through a Gaussian sample volume

5.1 Introduction

Under ideal conditions, the Doppler power spectrum would be determined solely by the range of blood velocities passing through the sample volume of the flow detector and the frequency of the emitted ultrasonic beam. Unfortunately that is not generally the case and factors like the size and shape of the sample volume, the spectral estimation technique used and the time variation of the velocity field also affect the Doppler spectrum. Thus, the measured spectrum results from the contributions of all these factors and the effect of the velocity field on the spectrum cannot, in general, be isolated from the rest.

In order to use our model described in the previous chapter to study the individual effect of the various factors to the resulting Doppler spectrum we need to calculate the spectrum due solely to the range of velocities passing through a sample volume of known form.

We describe in this chapter the derivation of a closed-form expression for the Doppler spectrum due solely to the range of velocities passing through a Gaussian sample volume placed anywhere in a vessel where the flow is steady and axisymmetric with a power law velocity profile.

We also present closed form expressions for the mean frequency and root mean square (rms) width of the Doppler spectrum for the special case of a symmetric Gaussian sample volume placed in the centre of the vessel.

This work extends the range of beam/flow conditions for which closed-form expressions for the Doppler spectrum are known.

5.2 Derivation of the Doppler spectrum

The following analyses make use of the coordinate system defined in figure 5.1. The vessel cartesian coordinate system is (x, y, z) and the beam coordinate system (x', y', z'). The axes z and z' are parallel. The origins of both systems, O' and O, are in the plane perpendicular to the vessel which includes the centre of the beam sample volume, $O' = (0, y_0, z_0)$. The angle between the beam and vessel axis is θ. It is convenient, in some places, to make use of axial symmetry and use the cylindrical coordinates r, ϕ defined in figure 5.1b. Axisymmetric flow, uniform backscatter, negligible intrinsic spectral broadening are assumed. The sample volume sensitivity variation is that measured in situ.

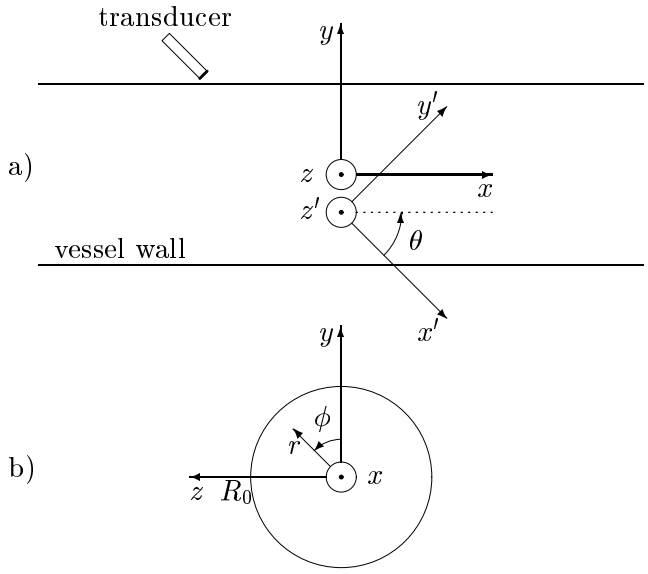

Figure 5.1: Geometry and coordinate systems: a) cartesian coordinate systems for the beam/vessel arrangement (x, y, z for the vessel and x', y', z' for the beam), the origins O and O' are in a plane perpendicular to the vessel which includes the centre of the beam sample volume, the axes z and z' are parallel and point out of the diagram plane; b) cross-section showing the vessel cartesian and cylindrical coordinate systems.

For uniform blood flow moving through a wide (negligible transit time broadening) ultrasound beam each streamline contributes with a single frequency to the Doppler power spectrum which is [Fish 1986, p. 368]:

$$S(\omega) = \int \delta(\omega - \omega_d(y, z)) W(y, z)\, dydz \tag{5.1}$$

where ω is the angular frequency, δ is the Delta function, $\omega_d(y, z)$ is the Doppler frequency for the streamline at position y, z, and $W(y, z)$ is the power received from the streamline.

Assuming that the backscatter from blood does not depend on the flow conditions and is constant over the entire vessel, the power from a streamline is proportional to the integral of the square of the beam sensitivity, $G(x, y, z)$, along the streamline [Fish 1986, p. 360]

$$W(y, z) = C \int G^2(x, y, z)\, dx \tag{5.2}$$

where C is a constant incorporating blood backscatter and other factors not dependent on the beam sensitivity.

Changing (5.1) to cylindrical coordinates:

$$S(\omega) = \int_0^{2\pi} \int_0^{R_0} \delta(\omega - \omega_d'(r, \phi))\, W'(r, \phi)\, r\, dr d\phi \tag{5.3}$$

where r is the radial coordinate, ϕ is the angle coordinate, R_0 is the radius of the vessel and $\omega_d'(r, \phi)$ and $W'(r, \phi)$ are $\omega_d(y, z)$ and $W(y, z)$ in the cylindrical coordinate system.

For axisymmetric flow $\omega_d'(r, \phi)$ depends only on r and (5.3) can be rewritten as:

$$S(\omega) = \int_0^{R_0} \delta(\omega - \omega_d'(r))\, W_{sh}(r)\, r\, dr \tag{5.4}$$

where

$$W_{\mathrm{sh}}(r) = \int_0^{2\pi} W'(r, \phi)\, d\phi \tag{5.5}$$

is the power returned by a shell at a distance r from the centre of the vessel.

If the velocity profile is a monotonic function of r then the inverse function, $r(\omega_d')$, exists and (5.4) can be simplified by changing the integration variable to ω_d' and making use of the filtering property of the δ function:

$$\begin{aligned} S(\omega) &= \int_0^{\omega_{d0}} \delta(\omega - \omega_d')\, W_{sh}(r(\omega_d'))\, r(\omega_d')\, \frac{dr(\omega_d')}{d\omega_d'}\, d\omega_d' \\ &= W_{sh}(r(\omega))\, r(\omega) \left| \frac{dr}{d\omega_d'} \right|_{\omega_d' = \omega} \end{aligned} \tag{5.6}$$

for $0 \leq \omega \leq \omega_{d0}$ and zero otherwise, ω_{d0} is the angular Doppler frequency corresponding to the velocity of the central streamline. All the following expressions for $S(\omega)$ are for the interval $0 \leq \omega \leq \omega_{d0}$ although no explicit mention of this is made in the text.

In this study we present results for the Doppler spectrum from blood flow with monotonic velocity profiles of the form:

$$v(r) = v_0 \left(1 - \frac{r^n}{R_0^n}\right) \tag{5.7}$$

which give rise to a Doppler frequency shift:

$$\omega'_d(r) = \omega_{d0}\left(1 - \frac{r^n}{R_0^n}\right) \tag{5.8}$$

where ω_{d0} is the angular frequency of the shifted signal and is given by the Doppler equation, $\omega_{d0} = -2v_0\cos(\theta)\omega_0/c$. The minus sign arises from the convention that positive velocities correspond to moving away from the transducer (negative frequency shift), ω_0 represents the angular frequency of the transmitted signal and c is the speed of sound.

For these velocity profiles the inverse function of $\omega'_d(r)$ is:

$$r(\omega'_d) = R_0\left(1 - \frac{\omega'_d}{\omega_{d0}}\right)^{\frac{1}{n}} \tag{5.9}$$

and the derivative of $r(\omega'_d)$ with respect to ω'_d is:

$$\frac{dr(\omega'_d)}{d\omega'_d} = -\frac{R_0}{n\omega_{d0}}\left(1 - \frac{\omega'_d}{\omega_{d0}}\right)^{\frac{1}{n}-1} \tag{5.10}$$

Thus from equations (5.6),(5.9) and (5.10) the Doppler power spectrum is:

$$S(\omega) = \frac{R_0^2}{n|\omega_{d0}|}\left(1 - \frac{\omega}{\omega_{d0}}\right)^{\frac{2}{n}-1} W_{\text{sh}}\left(R_0\left(1 - \frac{\omega}{\omega_{d0}}\right)^{\frac{1}{n}}\right) \tag{5.11}$$

In order to compute the Doppler power spectrum for different sample volumes we need only calculate the power from each flow shell, $W_{sh}(r)$.

5.2.1 Wide uniform beam

For a uniform beam wider than the vessel the power from each streamline is constant, $W'(r,\phi) = W$, and the Doppler power spectrum is given by:

$$S(w) = 2\pi\frac{WR_0^2}{n|\omega_{d0}|}\left(1 - \frac{\omega}{\omega_{d0}}\right)^{\frac{2}{n}-1} \tag{5.12}$$

which is equivalent to expressions derived previously by others [Aldis & Thompson 1992, Bascom & Cobbold 1990, Fish 1986].

5.2.2 Gaussian sample volume

The square of a Gaussian beam sensitivity function in the beam coordinate system is:

$$G'^2(x',y',z') = \exp\left(-\frac{x'^2}{2\,\sigma_{x'}^2} - \frac{y'^2}{2\,\sigma_{y'}^2} - \frac{z'^2}{2\,\sigma_{z'}^2}\right)^2 \tag{5.13}$$

where $\sigma_{x'}, \sigma_{y'}$ and $\sigma_{z'}$ are the rms widths of the beam sensitivity along the x', y' and z' axes respectively. Equation (5.13) can be transformed into the vessel coordinate system by the transformations:

$$x' = x\,\cos(\theta) - (y - y_0)\,\sin(\theta) \tag{5.14}$$

$$y' = x\,\sin(\theta) + (y - y_0)\,\cos(\theta) \tag{5.15}$$

$$z' = z - z_0 \tag{5.16}$$

which gives:

$$G^2(x,y,z) = \exp\left(-\frac{(z-z_0)^2}{\sigma_{z'}^2} - \frac{((y-y_0)\,\cos(\theta) + x\,\sin(\theta))^2}{{\sigma_{y'}}^2} - \frac{(x\,\cos(\theta) - (y-y_0)\,\sin(\theta))^2}{{\sigma_{x'}}^2}\right) \tag{5.17}$$

Expressing the argument of the exponential as a second order polynomial in x leads to:

$$G^2(x,y,z) = \exp\left(p_2 + p_1\,x + p_0\,x^2\right) \tag{5.18}$$

with polynomial coefficients given by:

$$p_0 = -\frac{\cos^2(\theta)}{\sigma_{x'}^2} - \frac{\sin^2(\theta)}{\sigma_{y'}^2} \tag{5.19}$$

$$p_1 = 2\,\cos(\theta)\,\sin(\theta)\left(\frac{1}{\sigma_{x'}^2} - \frac{1}{\sigma_{y'}^2}\right)\,(y - y_0) \tag{5.20}$$

$$p_2 = -\frac{(z-z_0)^2}{\sigma_{z'}^2} - \left(\frac{\cos^2(\theta)}{\sigma_{y'}^2} + \frac{\sin^2(\theta)}{\sigma_{x'}^2}\right)\,(y - y_0)^2 \tag{5.21}$$

The power received from each streamline can be evaluated from (5.2) using the standard result [Gradshtein & Ryzhik 1980, p. 307]:

$$\int_{-\infty}^{\infty} \exp\left(-p^2\,x^2 \pm q\,x\right)\,dx = \frac{\sqrt{\pi}}{p}\exp\left(\frac{q^2}{4p^2}\right) \qquad p > 0 \tag{5.22}$$

giving,

$$W(y,z) = \frac{C\sqrt{\pi}}{\sqrt{-p_0}}\exp\left(\frac{-{p_1}^2}{4\,p_0} + p_2\right) \qquad p_0 < 0 \tag{5.23}$$

which, after substitution of the p coefficients and some algebraic simplifications is:

$$W(y,z) = K\,\exp\left(-\frac{(z-z_0)^2}{\sigma_{z'}^2} - \frac{(y-y_0)^2}{\sigma_{y'}^2\cos^2(\theta) + \sigma_{x'}^2\sin^2(\theta)}\right) \tag{5.24}$$

where K is a constant given by,

$$K = \frac{C\sqrt{\pi}\,\sigma_{x'}\,\sigma_{y'}}{\sqrt{\sigma_{y'}^2\cos^2(\theta) + \sigma_{x'}^2\sin^2(\theta)}} \tag{5.25}$$

Equation (5.24) is a two dimensional Gaussian function which can be re-written, for simplicity, as:

$$W(y,z) = K\,\exp\left(-\frac{(z-z_0)^2}{\sigma_z^2} - \frac{(y-y_0)^2}{\sigma_y^2}\right) \tag{5.26}$$

$$\sigma_z = \sigma_{z'} \tag{5.27}$$

$$\sigma_y = \sqrt{\sigma_{y'}^2\cos^2(\theta) + \sigma_{x'}^2\sin^2(\theta)} \tag{5.28}$$

Changing now to cylindrical coordinates using the transformations $y = r\cos(\phi)$, $z = r\sin(\phi)$ and making use of standard trigonometric identities gives:

$$\begin{aligned} W'(r,\phi) = K\,\exp\left(-\frac{z_0^2}{\sigma_z^2} - \frac{y_0^2}{\sigma_y^2}\right)\,\exp\left(-r^2\,\frac{\sigma_z^2+\sigma_y^2}{2\,\sigma_z^2\,\sigma_y^2}\right) \\ \times\,\exp\left(-r^2\,\frac{\sigma_z^2-\sigma_y^2}{2\,\sigma_z^2\sigma_y^2}\cos(2\phi) + 2\,r\,\frac{\sqrt{\sigma_y^4 z_0^2 + \sigma_z^4 y_0^2}}{\sigma_z^2\sigma_y^2}\cos(\phi-\beta)\right) \end{aligned} \tag{5.29}$$

where $\beta = \arctan(z_0\,\sigma_y^2/y_0\,\sigma_z^2)$ and $\beta = 0$ if $y_0 = z_0 = 0$.

The power from each flow shell is:

$$\begin{aligned} W_{\rm sh}(r) &= \int_0^{2\pi} W'(r,\phi)\,d\phi \\ &= K\,\exp\left(-\frac{z_0^2}{\sigma_z^2} - \frac{y_0^2}{\sigma_y^2}\right)\,\exp\left(-r^2\,\frac{\sigma_z^2+\sigma_y^2}{2\,\sigma_z^2\,\sigma_y^2}\right) \\ &\qquad \times\,\mathrm{M}\left(2\,r\,\frac{\sqrt{\sigma_y^4 z_0^2 + \sigma_z^4 y_0^2}}{\sigma_z^2\sigma_y^2},\; -r^2\,\frac{\sigma_z^2-\sigma_y^2}{2\,\sigma_z^2\sigma_y^2},\; \beta\right) \end{aligned} \tag{5.30}$$

where $\mathrm{M}(a,b,\beta)$ is given by:

$$\begin{aligned} \mathrm{M}(a,b,\beta) &= \int_0^{2\pi} \exp\left(a\cos(\phi-\beta) + b\cos(2\phi)\right)\,d\phi \\ &= 2\pi\left[\mathrm{I}_0(a)\mathrm{I}_0(b) + 2\sum_{k=1}^{\infty}\mathrm{I}_{2k}(a)\mathrm{I}_k(b)\cos(2k\beta)\right] \end{aligned} \tag{5.31}$$

where the I_k are modified Bessel functions of order k. See appendix A for the derivation of the above result.

The Doppler power spectrum can then be calculated from (5.11) and (5.30) giving,

$$S(\omega) = \frac{K\,R_0^2}{n|\omega_{d0}|}\exp\left(-\frac{z_0^2}{\sigma_z^2}-\frac{y_0^2}{\sigma_y^2}\right)\left(1-\frac{\omega}{\omega_{d0}}\right)^{\frac{2}{n}-1}\exp\left(-R_0^2\frac{\sigma_z^2+\sigma_y^2}{2\,\sigma_z^2\,\sigma_y^2}\left(1-\frac{\omega}{\omega_{d0}}\right)^{\frac{2}{n}}\right)$$
$$\times\,\mathrm{M}\left(2\,R_0\frac{\sqrt{\sigma_y^4 z_0^2+\sigma_z^4 y_0^2}}{\sigma_z^2\sigma_y^2}\left(1-\frac{\omega}{\omega_{d0}}\right)^{\frac{1}{n}},\,-R_0^2\,\frac{\sigma_z^2-\sigma_y^2}{2\,\sigma_z^2\,\sigma_y^2}\left(1-\frac{\omega}{\omega_{d0}}\right)^{\frac{2}{n}},\,\beta\right) \quad (5.32)$$

For the specific case [$\theta = 90^{\mathrm{o}}$; $\sigma_{y'}, \sigma_{z'} \ll \sigma_{x'}$; $z_0 = y_0 = 0$] expression (5.32) for the Doppler power spectrum is the same as those derived previously by [Aldis & Thompson 1992, Bascom & Cobbold 1990]. For these conditions, note that the values of $\sigma_{x'}, \sigma_{y'}, \sigma_{z'}$ here are greater, by a factor of $\sqrt{2}$, than the corresponding variables used by the cited authors.

In the general case the Doppler spectrum can be calculated using (5.32), but when the sample volume/vessel arrangement exhibits symmetry, $\sigma_y = \sigma_z$, or the sample volume is placed at the centre of the vessel, $y_0 = z_0 = 0$, the expression can be simplified. Moreover, when the sample volume is symmetric and centred in the vessel, analytical expressions for the Doppler spectral width and mean frequency can be derived.

5.2.3 Symmetric sample volume

When $\sigma_y = \sigma_z = \sigma_{sv}$ the power from the streamlines, $W(y, z)$, is symmetric in relation to the centre of the sample volume, the second argument of $\mathrm{M}(a, b, \beta)$ in equation (5.32) is zero and the Doppler spectrum is given by,

$$S(\omega) = \frac{2\,\pi\,K\,R_0^2}{n|\omega_{d0}|}\exp\left(-\frac{z_0^2+y_0^2}{\sigma_{sv}^2}\right)\left(1-\frac{\omega}{\omega_{d0}}\right)^{\frac{2}{n}-1}$$
$$\times\exp\left(-\frac{R_0^2}{\sigma_{sv}^2}\left(1-\frac{\omega}{\omega_{d0}}\right)^{\frac{2}{n}}\right)\mathrm{I}_0\left(2\,R_0\frac{\sqrt{z_0^2+y_0^2}}{\sigma_{sv}^2}\left(1-\frac{\omega}{\omega_{d0}}\right)^{\frac{1}{n}}\right) \quad (5.33)$$

5.2.4 Sample volume centred in the vessel

When the sample volume is centred in the vessel ($y_0 = z_0 = 0$), the first argument of $\mathrm{M}(a, b, \beta)$ in equation (5.32) is zero and the Doppler spectrum is:

$$S(\omega) = \frac{2\pi\,K\,R_0^2}{n|\omega_{d0}|}\left(1-\frac{\omega}{\omega_{d0}}\right)^{\frac{2}{n}-1}\exp\left(-R_0^2\frac{\sigma_z^2+\sigma_y^2}{2\,\sigma_z^2\,\sigma_y^2}\left(1-\frac{\omega}{\omega_{d0}}\right)^{\frac{2}{n}}\right)$$
$$\times\,\mathrm{I}_0\left(-R_0^2\,\frac{\sigma_z^2-\sigma_y^2}{2\,\sigma_z^2\,\sigma_y^2}\left(1-\frac{\omega}{\omega_{d0}}\right)^{\frac{2}{n}}\right) \quad (5.34)$$

5.2.5 Symmetric sample volume centred in the vessel

If the sample volume is centred in the vessel ($y_0 = z_0 = 0$) and the power from each streamline is a Gaussian function symmetric in relation to the centre of the sample volume ($\sigma_y = \sigma_z =$

σ_{sv}), the first and second arguments of function M are zero and (5.32) can be significantly simplified because $\mathrm{M}(0,0,\beta) = 2\,\pi$. The expression for the Doppler spectrum can then be re-written as:

$$S(\omega) = \frac{2\,\pi\,K\,R_0^2}{n|\omega_{d0}|}\left(1-\frac{\omega}{\omega_{d0}}\right)^{\frac{2}{n}-1}\exp\left(-\frac{R_0^2}{\sigma_{sv}^2}\left(1-\frac{\omega}{\omega_{d0}}\right)^{\frac{2}{n}}\right) \tag{5.35}$$

For this special case with maximum symmetry we can derive analytical expressions for the Doppler mean frequency and rms spectral width as functions of the velocity profile and sample volume size.

Mean frequency and rms spectral width

As already mentioned in Chapter 2, we use the rms width, σ, as the measure of spectral width. It is defined as,

$$\sigma = \frac{1}{2\pi}\sqrt{\frac{\int(\omega-\overline{\omega})^2\,S(\omega)\,d\omega}{\int S(\omega)\,d\omega}} \tag{5.36}$$

where $\overline{\omega}$ is the mean angular frequency,

$$\overline{\omega} = \frac{\int \omega S(\omega)\,d\omega}{\int S(\omega)\,d\omega} \tag{5.37}$$

and the mean frequency is:

$$\overline{f} = \frac{\overline{\omega}}{2\,\pi} \tag{5.38}$$

The expressions for the mean frequency and rms spectral width may be re-written as:

$$\overline{f} = \frac{1}{2\pi}\times\frac{\Omega_1}{\Omega_0} \tag{5.39}$$

$$\begin{aligned}\sigma &= \frac{1}{2\pi}\sqrt{\frac{\int\omega^2 S(\omega)\,d\omega}{\int S(\omega)\,d\omega}-\overline{\omega}^2} \\ &= \frac{1}{2\pi}\sqrt{\frac{\Omega_2}{\Omega_0}-\left(\frac{\Omega_1}{\Omega_0}\right)^2}\end{aligned} \tag{5.40}$$

where Ω_m represents the moment of $S(\omega)$ of order m,

$$\Omega_m = \int \omega^m S(\omega)\,d\omega \tag{5.41}$$

To evaluate the moments for the power spectrum defined by equation (5.35) we make the substitution $u = (1-\omega/\omega_{d0})^{1/n}$ and note that the spectrum is only not zero for $0 \le \omega \le \omega_{d0}$.

Thus:

$$\begin{aligned}\Omega_m &= \int_0^{\omega_{d0}} \omega^m S(\omega)\, d\omega \\ &= nK'\omega_{d0}^{m+1} \int_0^1 (1-u^n)^m\, u\, e^{-(\alpha u)^2}\, du\end{aligned} \tag{5.42}$$

where K' and α are constants defined by:

$$K' = \frac{2\,\pi\,K\,R_0^2}{n|\omega_{d0}|} \tag{5.43}$$

$$\alpha = \frac{R_0}{\sigma_{sv}} \tag{5.44}$$

The Ω_m can be expressed as a sum of integrals of the form

$$\begin{aligned}X_p(\alpha) &= \int_0^1 u^p e^{-(\alpha u)^2}\, du \\ &= \begin{cases} \dfrac{\gamma\left(\frac{1+p}{2}, \alpha^2\right)}{2\,\alpha^{p+1}} & ,\ \alpha > 0 \\ \dfrac{1}{p+1} & ,\ \alpha = 0 \end{cases}\end{aligned} \tag{5.45}$$

where $\gamma(a,x)$ is the incomplete gamma function defined by [Abramowitz & Stegun 1972, p. 260] as:

$$\gamma(a,x) = \int_0^x t^{a-1} e^{-t}\, dt \tag{5.46}$$

The first three moments of $S(\omega)$ are,

$$\begin{aligned}\Omega_0 &= nK'\omega_{d0} \int_0^1 u e^{-(\alpha u)^2}\, du \\ &= nK'\omega_{d0} X_1(\alpha)\end{aligned} \tag{5.47}$$

$$\begin{aligned}\Omega_1 &= nK'\omega_{d0}^2 \int_0^1 (1-u^n)\, u e^{-(\alpha u)^2}\, du \\ &= nK'\omega_{d0}^2 \left[X_1(\alpha) - X_{n+1}(\alpha)\right]\end{aligned} \tag{5.48}$$

$$\begin{aligned}\Omega_2 &= nK'\omega_{d0}^3 \int_0^1 (1-u^n)^2\, u e^{-(\alpha u)^2}\, du \\ &= nK'\omega_{d0}^3 \left[X_1(\alpha) - 2X_{n+1}(\alpha) + X_{2n+1}(\alpha)\right]\end{aligned} \tag{5.49}$$

The mean frequency may be computed by substituting Ω_0 and Ω_1 in equation (5.39):

$$\overline{f}(n,\alpha) = \frac{\omega_{d0}}{2\,\pi} \times \begin{cases} 1 - \dfrac{\gamma\left(n/2+1,\alpha^2\right)}{\alpha^{n+2}\left(1-e^{-\alpha^2}\right)} & , \alpha > 0 \\ \\ \dfrac{n}{n+2} & , \alpha = 0 \end{cases} \tag{5.50}$$

and the rms width is from equation (5.40):

$$\begin{aligned} \sigma(n,\alpha) &= \frac{|\omega_{d0}|}{2\pi}\sqrt{\frac{X_1(\alpha) - 2X_{n+1}(\alpha) + X_{2n+1}(\alpha)}{X_1(\alpha)} - \left(\frac{X_1(\alpha) - X_{n+1}(\alpha)}{X_1(\alpha)}\right)^2} \\ &= \frac{|\omega_{d0}|}{2\pi}\sqrt{\frac{X_1(\alpha)X_{2n+1}(\alpha) - X_{n+1}^2(\alpha)}{X_1^2(\alpha)}} \\ &= \frac{|\omega_{d0}|}{2\,\pi} \times \begin{cases} \dfrac{\sqrt{\left(1-e^{-\alpha^2}\right)\gamma(n+1,\alpha^2) - \gamma^2(n/2+1,\alpha^2)}}{\alpha^n\left(1-e^{-\alpha^2}\right)} & , \alpha > 0 \\ \\ \dfrac{n}{n+2}\sqrt{\dfrac{1}{n+1}} & , \alpha = 0 \end{cases} \end{aligned} \tag{5.51}$$

5.3 Experiments

In order to study the effect of the dimensions and position of a Gaussian sample volume on the mean frequency and width of the Doppler spectrum, the expressions derived in the previous section were used to compute the Doppler spectrum for various beam/vessel arrangements.

The mean Doppler frequency and the spectral width were computed using expressions (5.36) to (5.38), the only exception being the case of a symmetrical sample volume centred in the vessel for which expressions (5.50) and (5.51) were used.

Data was computed for three velocity profiles corresponding to $n = 2$, $n = 5$ and $n = 9$. Data for other velocity profiles with a power law could have been computed but a large number of plots would make the diagrams difficult to read and interpret.

Firstly, the general case of a Gaussian sample volume placed at various positions in the vessel was studied. Next, other cases in which the sample volume is either symmetric or centred in the vessel were considered, and finally the special case of a symmetric sample volume centred in the vessel.

5.4 Results

5.4.1 Non-symmetric sample volumes

Figure 5.2 shows, as an example, the Doppler power spectra normalised to a maximum of unity for a parabolic velocity profile. The spectra were obtained using equation (5.32) for three Gaussian sample volumes with centres placed at nine different locations as defined in figure 5.3. The three sample volumes have constant $\sigma_z = 0.25 R_0$ and $\sigma_y = \sigma_z, 3\sigma_z$ and $5\sigma_z$.

As the sample volume centre moves from the vessel centre to the vessel wall the spectra widen and the peak frequency moves to lower frequencies. For the elongated sample volumes this peak frequency shift is more sensitive to movement of the sample volume centre along the z direction than along the y direction. Elongation of the sample volume leads to an increase in spectral width.

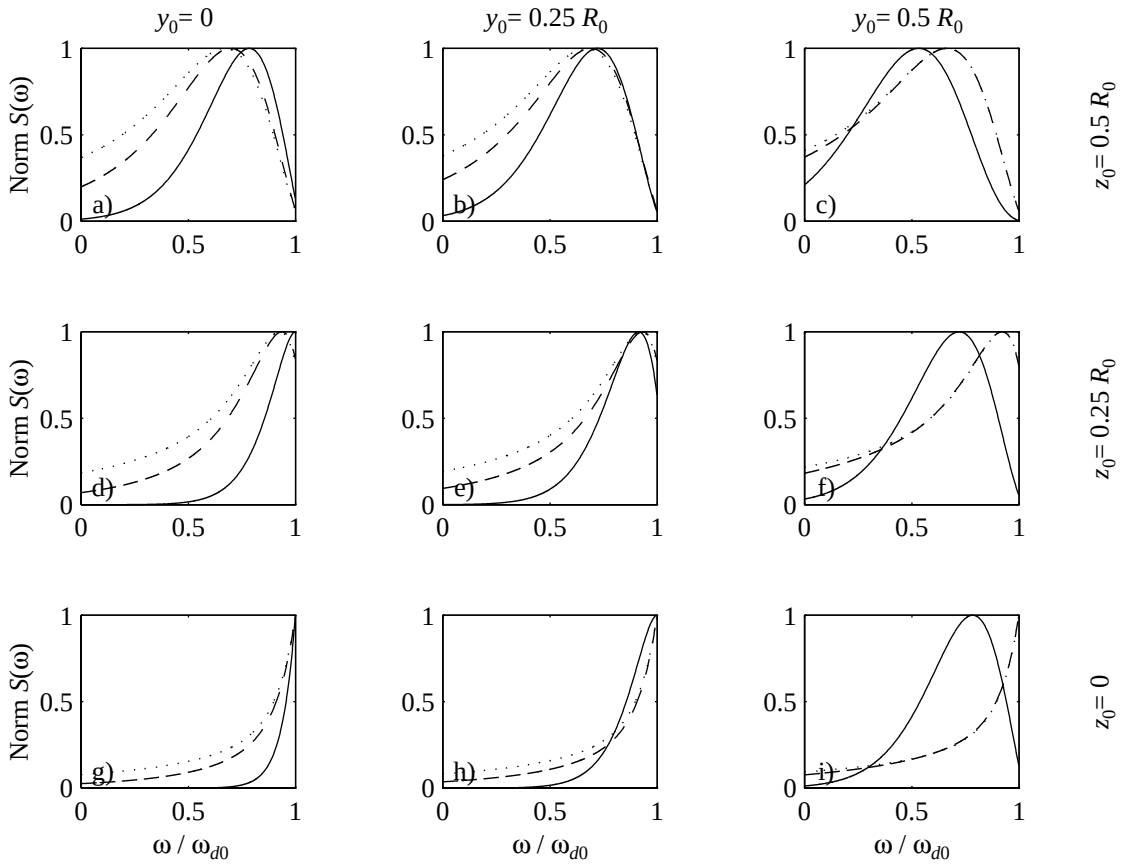

Figure 5.2: Normalised Doppler spectra from parabolic velocity profile using Gaussian sample volumes placed at the positions set in figure 5.3: $\sigma_z = 0.25\, R_0$; ——, $\sigma_y = \sigma_z$; – – –, $\sigma_y = 3\,\sigma_z$; · · ·, $\sigma_y = 5\,\sigma_z$.

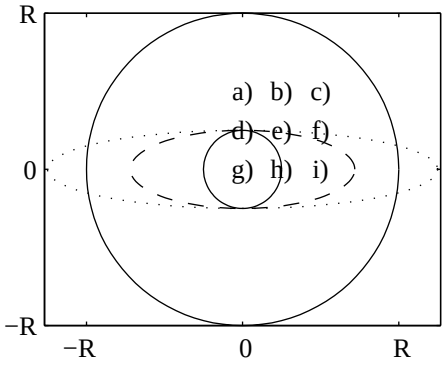

Figure 5.3: Locations of the sample volume in the vessel for computing the results shown in figures 5.2, 5.4 and 5.5. The lines in the centre of the vessel are iso-sensitivity curves for $G^2(y,z) = \exp(-1/2)$: $\sigma_z = 0.25\,R_0$; ——, $\sigma_y = \sigma_z$; - - -, $\sigma_y = 3\,\sigma_z$; · · ·, $\sigma_y = 5\,\sigma_z$.

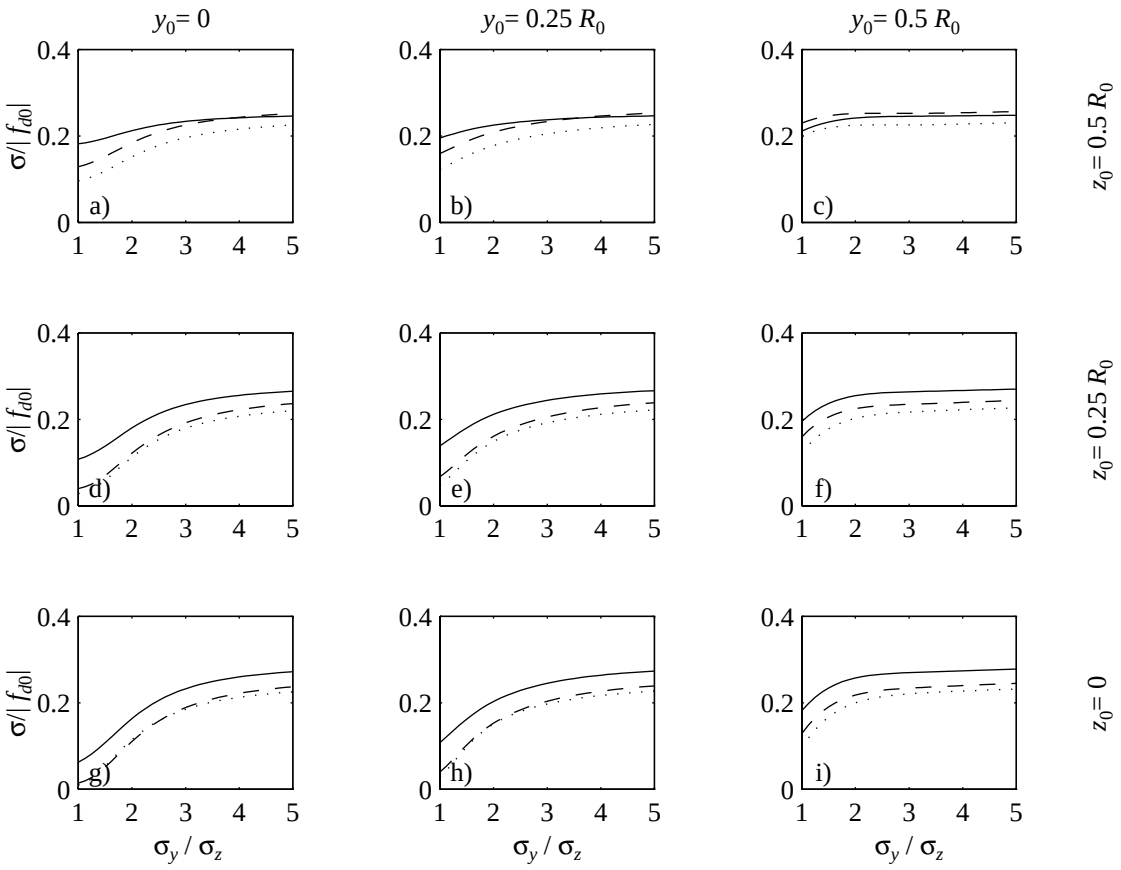

Figure 5.4: Normalised Doppler spectral width from Gaussian sample volumes centred on the positions set in figure 5.3: $\sigma_z = 0.25\,R_0$; ——, $n = 2$; - - -, $n = 5$; · · ·, $n = 9$.

Figures 5.4 and 5.5 present the normalised spectral width and normalised Doppler mean frequency for Doppler signals generated by three velocity profiles, $n = 2, 5$ and 9. The sample volumes have the same characteristics as those used to compute the power spectra displayed in figure 5.2 and were placed at the same positions in the vessel. The normalisation of the plots is performed by dividing the spectral width and mean frequency values by f_{d0} ($= \omega_{d0}/(2\pi)$), the Doppler frequency shift for the mid-stream velocity.

The spectral width increases with sample volume size and with decreasing n value as the range of velocities involved increases. As expected, $\sigma/|f_{d0}|$ is more sensitive to the position of the smaller sample volumes than to the position of the larger ones.

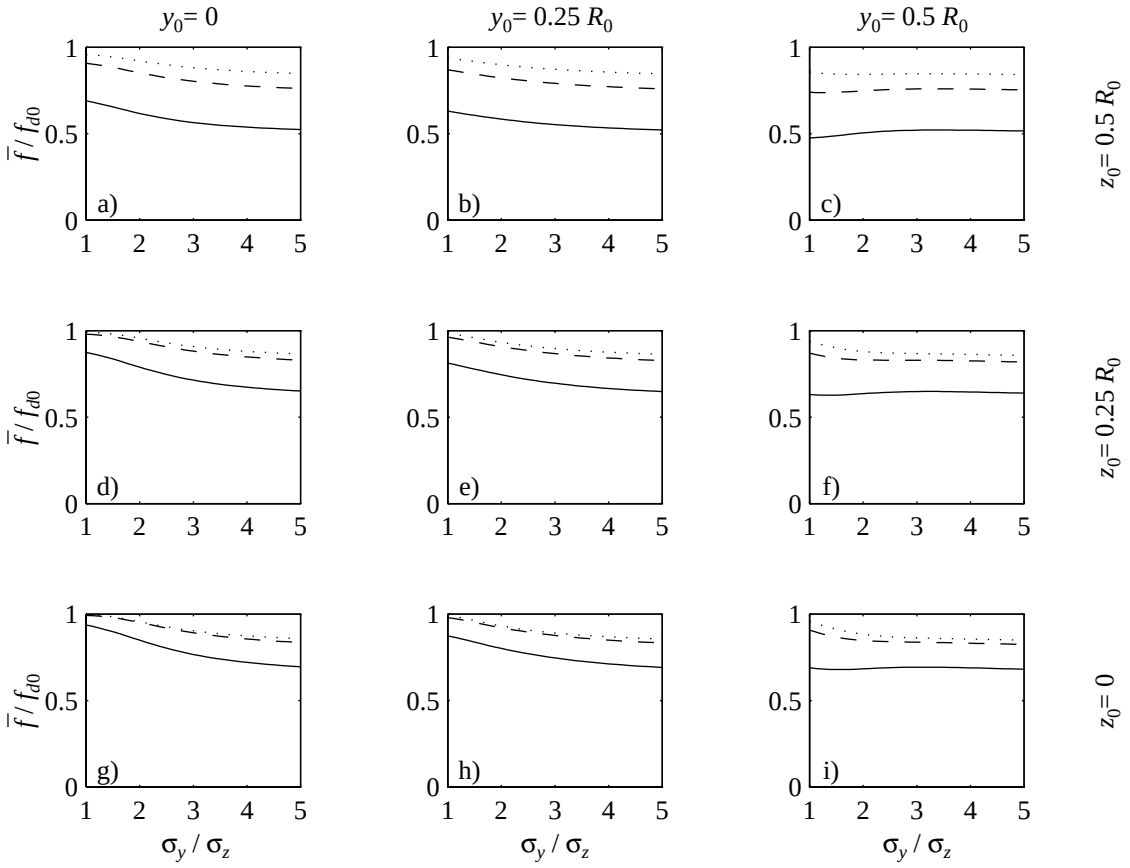

Figure 5.5: Normalised mean frequency for the Doppler signal from Gaussian sample volumes centred on the positions set in figure 5.3: $\sigma_z = 0.25\,R_0$; ——, $n = 2$; – – –, $n = 5$; · · ·, $n = 9$.

As can be seen from figure 5.5 the mean frequency generally decreases as the size of the sample volume increases. This decrease is more noticeable for the parabolic velocity profile than for the higher order velocity profiles because the later are much flatter than the former. In the positions where $y_0 = 0.5R_0$ the mean frequency is almost constant, even for the parabolic profile case, over the range of sample volume sizes studied. Probably the increased range of velocities due to the larger sample volume compensates the higher weighting of the slow moving flow shells.

5.4.2 Sample volumes with some symmetry

Symmetric sample volume

Figure 5.6 shows the normalised spectral width and normalised mean frequency of three symmetric Gaussian sample volumes as a function of the distance between the centre of the sample volume and the centre of the vessel. In this case the spectra were calculated using equation (5.33).

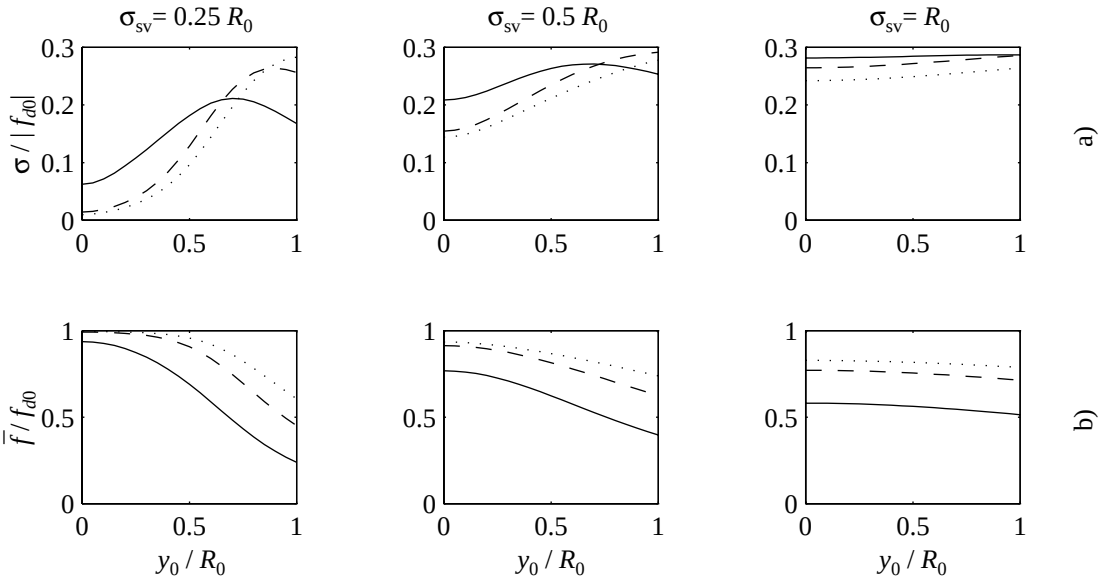

Figure 5.6: Normalised Doppler spectral width a) and normalised Doppler mean frequency b) from symmetric Gaussian sample volumes not centred in the vessel: ——, $n = 2$; – – –, $n = 5$; · · ·, $n = 9$.

Neither the spectral width nor the mean frequency depend significantly on the position of the sample volume within the vessel when using large symmetric sample volumes since the vessel can be considered 'spanned' by the sample volume in all the positions considered.

For the smaller sample volumes the mean frequency decreases as the distance between the centre of the vessel and the centre of the sample volume increases and the velocities within the sample volume shift to lower values. On the other hand the spectral width increases with an increase in the range of velocities but only up to a maximum that depends on the velocity profile and the size of the sample volume. After this maximum the velocity range within the sample volume decreases as part of the sample volume moves out of the vessel.

Sample volume centred in the vessel

Figure 5.7 shows the normalised spectral width and mean frequency of centred Gaussian sample volumes as a function of sample volume size. The spectra were calculated using equation (5.34).

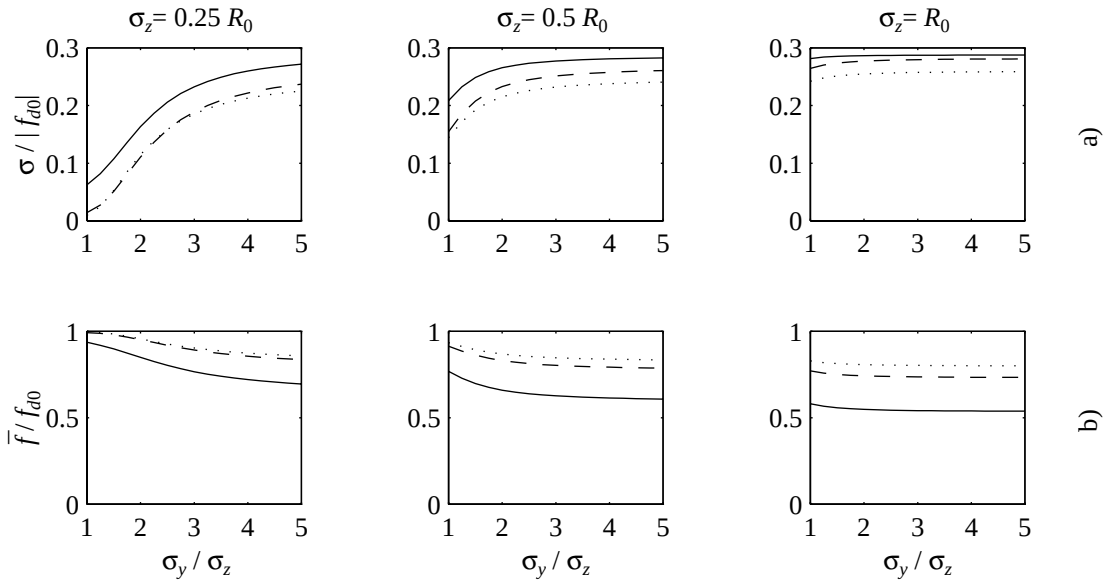

Figure 5.7: Normalised Doppler spectral width a) and normalised Doppler mean frequency b) from non-symmetric Gaussian sample volumes centred in the vessel: ——, $n = 2$; – – –, $n = 5$; · · ·, $n = 9$.

The plots show, as expected, an increase of the Doppler spectral width and a decrease of the mean frequency with increasing sample volume size as a result of an increasing range of velocities passing through the sample volume. The mean frequency and spectral width are largely independent of sample volume size provided it is sufficiently large to span the vessel.

Symmetric sample volume centred in the vessel

Figure 5.8 shows the normalised spectral width and the normalised mean frequency for the Doppler spectrum described by (5.35). In this case these quantities can be calculated using equations (5.50) and (5.51).

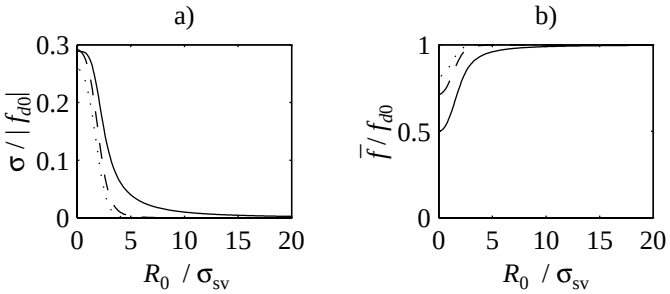

Figure 5.8: Normalised Doppler spectral width a) and normalised Doppler mean frequency b) as a function of $\alpha = R_0/\sigma_{sv}$ from symmetric Gaussian sample volumes centred in the vessel: ——, $n = 2$; – – –, $n = 5$; · · ·, $n = 9$.

As expected, the spectral width decreases with decreasing sample volume size (increasing α) and decreasing range of velocities within the sample volume (increasing n). The mean frequency approaches f_{d0} as the sample volume decreases in size. When the ultrasonic beam is uniform and infinitely wide, $\alpha = 0$, the normalised rms spectral width reaches its maximum value and the mean frequency its minimum value determined by the average velocity within the vessel.

5.5 Concluding remarks

Previous investigations into closed-form expressions relating Doppler spectra to ultrasound beam characteristics [Aldis & Thompson 1992, Bascom & Cobbold 1990] were valid only for very long sample volumes (continuous wave Doppler systems) and assumed that the centre of the sample volume was aligned with the centre of the vessel. We have derived an analytical expression for the Doppler power spectrum due solely to the range of velocities passing through a Gaussian sample volume placed anywhere within axisymmetric flow thereby extending the range of conditions for which closed-form expressions are available. Our formulation allows the specification of the sample volume position and the independent specification of its width in the three dimensions and should enable simpler estimations of spectral shape for pulsed wave systems.

In order to derive the Doppler spectrum we have computed the power received from each flow shell by integrating the contribution of each streamline at a constant distance from the centre of the vessel. Although our method is valid for steady axisymmetric flow with monotonic (in r) velocity profiles we have presented only expressions for the Doppler spectrum from blood flow with a simple power law which is the most common description for physiologic velocity profiles.

For sample volume/vessel arrangements with some symmetry (sample volumes centred in the vessel and/or sample volumes symmetric with respect to its centre) several simpler expressions were derived for the Doppler power spectrum. These simpler expressions allow the study of the influence of the position and shape of a Gaussian sample volume on the Doppler power spectrum.

The expressions derived ignore the effects of intrinsic spectral broadening, finite spectral estimator resolution and unsteady flow and are limited to Gaussian sample volumes and axisymmetric flow. However, in many situations the range of blood velocities within the sample volume is the dominant factor in determining spectral shape and width and in these cases it should be possible to express the effect of deviations from a Gaussian shape and the factors tending to broaden the spectrum as perturbations on the spectra derived using the techniques described in this work.

Chapter 6

Spectral broadening in the Doppler signal—a model based study

6.1 Introduction

The measured spectrum of the Doppler signal depends on the spatial and temporal variation of velocity, sensitivity variation within the sample volume, deviations from plane-wave conditions and window type and length. Clearly if the sample volume is very small, intrinsic broadening will dominate and the other factors will have a negligible effect. If the blood experiences a large acceleration for a long data window, the sample volume is large and the range of velocities passing through the sample volume is small, the spectrum will be dominated by nonstationarity broadening.

A better knowledge of the effect of all these contributory factors may allow for partial correction of the Doppler spectrum and an increase in the accuracy of velocity estimation, lesion detection and lesion size quantification. In order to make these corrections, simple but accurate methods of estimating the spectral shape from knowledge of the time-varying velocity profile, sample volume and spectral estimator characteristics would be useful in order to develop solutions to the inverse problem.

In this chapter we present a study showing the influence of blood acceleration, sample volume size and window length on the rms width of the Doppler power spectrum. We also present a simple estimation formula for the rms spectral width of Doppler spectra.

We use the rms spectral width to measure the width of the Doppler spectrum because, as mentioned in Chapter 2, this measure potentially allows correction for two spectral broadening mechanisms, window and non-stationarity broadening [Wang & Fish 1997].

6.2 Separation of factors affecting the Doppler spectrum

Various spectral estimation techniques currently in use to estimate the Doppler spectrum were introduced in Chapter 2. Although, various authors have suggested that some of the more recent time-frequency distributions, like the BD [Guo et al. 1994*a*] and the CWD [Cardoso et al. 1996], give better spectral estimates than the more traditional ones (spectrogram, ARMA modelling), we opted to use the spectrogram because it is the spectral estimation technique most frequently used in clinical applications.

In order to see the effect of the various components on spectral width it is useful to return to the time signal in (4.10) and to attempt to separate out these components.

We start with the Doppler signal given by (4.10),

$$s(t) = \sum_q \sum_m A_{qm}\, e^{-j(2\cos(\theta)k x_{qm}(t)+\phi_{qm})} G_{qm}(t)$$

The signal during the window centred on time t_w is:

$$s_w(t,t_w) = w(t-t_w) \sum_q \sum_m A_{qm}\, e^{-j(2\cos(\theta)k x_{qm}(t)+\phi_{qm})} G(x_{qm}, y_{qm}, z_{qm}) \tag{6.1}$$

Substituting x_{qm} from (4.8), putting $t_r = t_w$,

$$\phi_{1qm} = \phi_{qm} + 2\cos(\theta) k\, x_{qm}(t_w) \tag{6.2}$$

and

$$v_{qm}(t) = v_{qm}(t_w) + v_{dqm}(t) \tag{6.3}$$

where $v_{dqm}(t)$ is the difference between the velocity of the elemental volume and the mid-window velocity ($v_{qm}(t_w)$). We then obtain:

$$\begin{aligned} s_w(t,t_w) = w(t-t_w) \sum_q \sum_m & A_{qm}\, e^{-j\left(2\cos(\theta)k\left(v_{qm}(t_w)(t-t_w)+\int_{t_w}^{t} v_{dqm}(\tau)\,d\tau\right)+\phi_{1qm}\right)} \\ & \cdot G\left(x_{qm}(t_w) + v_{qm}(t_w)(t-t_w) + \int_{t_w}^{t} v_{dqm}(\tau)\,d\tau, y_{qm}, z_{qm}\right) \end{aligned} \tag{6.4}$$

Extracting a factor $e^{-j\overline{\omega}(t_w)(t-t_w)} e^{-j\int_{t_w}^{t} \overline{\omega}_d(\tau)\,d\tau}$ where $\overline{\omega}(t_w)$ is the mid-window mean Doppler frequency and $\overline{\omega}_d(t_w)$ is the deviation from this during the window period, we can write:

$$s(t,t_w) = s_{mod}(t,t_w) w_1(t,t_w) s_b(t,t_w) \tag{6.5}$$

where

$$s_{mod}(t,t_w) = e^{-j\overline{\omega}(t_w)(t-t_w)} \tag{6.6}$$

$$w_1(t,t_w) = w(t-t_w)\, e^{-j\int_{t_w}^{t}\overline{\omega}_d(\tau)\,d\tau} \tag{6.7}$$

$$\begin{aligned} s_b(t,t_w) = \sum_q \sum_m A_{qm}\, e^{-j\left(2\cos(\theta)k\left((v_{qm}(t_w)-\overline{v}(t_w))(t-t_w)+\int_{t_w}^{t}\left(v_{dqm}(\tau)-\overline{v}_d(\tau)\right)d\tau\right)+\phi_{1qm}\right)} \\ \cdot\, G\left(x_{qm}(t_w)+v_{qm}(t_w)(t-t_w)+\int_{t_w}^{t} v_{dqm}(\tau)\,d\tau, y_{qm}, z_{qm}\right) \end{aligned} \tag{6.8}$$

and

$$\overline{v}(t) = \overline{v}(t_w) + \overline{v}_d(t) \tag{6.9}$$

is the spatial mean blood velocity within the sample volume, $\overline{v}_d(t)$ is the difference between this and the mid-window velocity $\overline{v}(t_w)$. The corresponding Doppler frequencies are $\overline{\omega}(t)$ and $\overline{\omega}_d(t)$; (i.e. $\overline{\omega}(t) = 2\cos(\theta)k\,\overline{v}(t)$).

The first term in (6.5), $s_{mod}(t,t_w)$, is a modulation at the mean Doppler shift frequency calculated from the spectrum at time t_w. In the frequency domain this is a shift to frequency $\overline{\omega}(t_w)$ which means that the remainder of the signal is base-band (centred on zero frequency).

The term $w_1(t,t_w)$ is a complex chirp with an envelope equal to the window function and a frequency variation given by the acceleration-induced change in spatial mean frequency during the window.

The remaining term $s_b(t,t_w)$ describes the effect of the beam ($G(.)$) - intrinsic spectral broadening - and the velocity variation within the sample volume. The modulation term $e^{-j2\cos(\theta)k(v_{qm}(t_w)-\overline{v}(t_w))(t-t_w)}$ supplying a frequency component to the base-band spectrum determined by the deviation of the element velocity from the spatial mean velocity of the blood within the sample volume at time t_w and the chirp term $e^{-j2\cos(\theta)k\int_{t_w}^{t}\left(v_{dqm}(\tau)-\overline{v}_d(\tau)\right)d\tau}$ broadening each component according to the deviation of the time-variation of the element velocity from the time-variation of the spatial mean blood velocity within the window duration.

6.2.1 Effect of window and acceleration

If the temporal variation of the blood velocity within the window duration is zero ($\overline{v}_d(t) = v_{qm} = 0$) or negligible then the windowed signal (6.5) is:

$$s(t,t_w) = e^{-j\overline{\omega}(t_w)(t-t_w)}\, w(t-t_w) s_b(t,t_w) \tag{6.10}$$

where $w(t)$ is the window function. The energy spectrum of the windowed signal is [Papoulis 1991]

$$S(\omega) = S_b(\omega - \overline{\omega}(t_w)) * |W(\omega)|^2 \tag{6.11}$$

where $W(\omega)$ is the Fourier transform of $w(t)$, $S_b(\omega)$ is the unwindowed signal base-band signal spectrum, and $*$ denotes convolution. Since variances add during convolution [Bracewell 1986],

$$\sigma = \sqrt{\sigma_b^2 + \sigma_w^2} \tag{6.12}$$

where σ_b and σ_w are the rms width of $S_b(\omega)$ and $|W(\omega)|^2$ respectively. The width σ_w of the window spectrum is inversely proportional to the time duration, T_D, of the window function. For the case of the Hanning window, for example, σ_w is given by,

$$\sigma_w(Hanning) = \frac{1}{\sqrt{3}T_D} \tag{6.13}$$

Note that σ_w is finite, and therefore the rms spectral width usable, only if the second moment of $|W(\omega)|^2$ is convergent (that is $|W(\omega)|^2$ decreases faster than $1/\omega^2$ as $\omega \to \infty$). This is true for the Hanning and Bartlett windows, for example, but not for the Boxcar and Hamming [Papoulis 1988].

In accelerating or decelerating flow equations (6.11) and (6.12) are replaced by:

$$S(\omega) = S_b(\omega - \overline{\omega}(t_w)) * |W_1(\omega)|^2 \tag{6.14}$$

$$\sigma = \sqrt{\sigma_b^2 + \sigma_1^2} \tag{6.15}$$

where $W_1(\omega)$ is the Fourier transform of $w_1(t, t_w)$ [Fish 1991] and incorporates the change in spatial mean velocity during the window period, and σ_1 is the rms width of $|W_1(\omega)|^2$.

This change also leads to an increase in spectral width [Fish 1991] and in this case this non-stationarity broadening increases with an increase in window duration T_D. Fish [1992] and Wang & Fish [1997] discuss two methods of correcting for this combined window and non-stationarity broadening.

A closed form expression for $|W_1(\omega)|^2$ and σ_1 exists if the mean frequency of the signal varies at a constant rate, β (constant acceleration) during the window period, the window is an even function with a long duration and intrinsic broadening is small - that is $|W_1(\omega)|^2$ is dominated by the effect of mean frequency variation. Under these conditions the stationary phase method can be used to compute $|W_1(\omega)|^2$ [Skolnik 1970, Papoulis 1988, Fish 1991], giving:

$$|W_1(\omega)|^2 \approx \frac{w^2\left(\omega/2\pi\beta\right)}{2\pi\beta} \tag{6.16}$$

and:

$$\sigma_1 = \beta\sigma_t = \frac{\omega_0 \cos(\theta) a \sigma_t}{\pi c} \tag{6.17}$$

where ω_0 is the angular frequency of the transmitted ultrasonic wave, c is the speed of sound in blood and σ_t is the rms width of $w^2(t)$ and we have related β to the acceleration a using the standard Doppler equation. For the case of the Hanning window σ_t is given by,

$$\sigma_t(Hanning) = \frac{T_D}{2\pi}\sqrt{\frac{2\pi^2 - 15}{6}} \tag{6.18}$$

Thus, when the Doppler spectrum width is dominated by nonstationarity broadening the spectral width is proportional to the rate of frequency variation and to the width of the squared window function.

Although it has been shown [Fish 1991] that in the case of the Gaussian window and constant acceleration, non-stationarity ($\beta\sigma_t$) and window broadening (σ_w) can be combined to give:

$$\sigma_1 = \sqrt{\sigma_w^2 + \beta^2\sigma_t^2} \tag{6.19}$$

this is also a very good approximation for the Bartlett and Hanning windows. Comparison of this approximate formula with a rms width calculated from $|W_1|^2$ shows that it gives an error of less than 1% over a β range of 0–0.2 kHz/ms and window duration T_D of 1–40 ms.

Note, however, that the above addresses only the effect on the spectral width due to mean frequency variation. Blood acceleration also has an effect on the base band signal $s_b(t, t_w)$ spectrum (see (6.8)) by means of the spread of blood acceleration within the sample volume and distorting the shape of $G(.)$ as a function of time.

The effect of acceleration on intrinsic spectral broadening cannot be simply expressed in the general case. However, limiting the consideration to constant acceleration a_{qm} the term governing intrinsic broadening becomes:

$$G\Big(x_{qm}(t_w) + v_{qm}(t_w)(t - t_w) + \int_{t_w}^{t} v_{dqm}(\tau)\, d\tau, y_{qm}, z_{qm}\Big) = G\Big(x_{qm}(t_w) + v_{qm}(t_w)(t - t_w) + \frac{a_{qm}\left(t^2 - t_w^2\right)}{2}, y_{qm}, z_{qm}\Big) \tag{6.20}$$

For a Gaussian $G(.)$, taking the position origin to be the centre of the beam, putting $x_{qm}(t_w) = 0$ and $t_w = 0$ (these conditions merely simplify the expression, they do not affect the shape of $G(.)$ or its spectrum) and dropping the subscripts, we have:

$$G\Big(x_{qm}(t_w) + v_{qm}(t_w)(t - t_w) + \int_{t_w}^{t} v_{dqm}(\tau)\, d\tau, y_{qm}, z_{qm}\Big) = \exp\Big(-\frac{\left(v(0)t + at^2/2\right)^2}{2\sigma_{\mathrm{sv}}^2}\Big) \tag{6.21}$$

The width of the energy spectrum of this signal determines the degree of intrinsic broad-

ening but no simple expression for this or its width (except for the $a = 0$ case) has been found. However, it is possible to derive an index which determines the degree to which acceleration distorts the shape of $G(.)$ and therefore the width of its spectrum.

The degree of distortion is clearly governed by the ratio of the term $at^2/2$ to $v(0)t$. At a time given by $v(0)t = \sigma_{\rm sv}$ this ratio is:

$$I_d = \frac{a\sigma_{\rm sv}}{2v(0)^2} \tag{6.22}$$

Considering an extreme case of $\sigma_{\rm sv} = 2$ mm and $a = 50$ m s^{-2} a scatterer starting at rest at the 'edge' of the beam ($3\sigma_{\rm sv}$ from the centre) will have a velocity of 0.775 m s^{-1} at the centre giving $I_d = 0.083$. The plot of $G(.)$ for this case compared with that for the same beam width and mid-beam velocity but zero acceleration is shown in figure 6.1a.

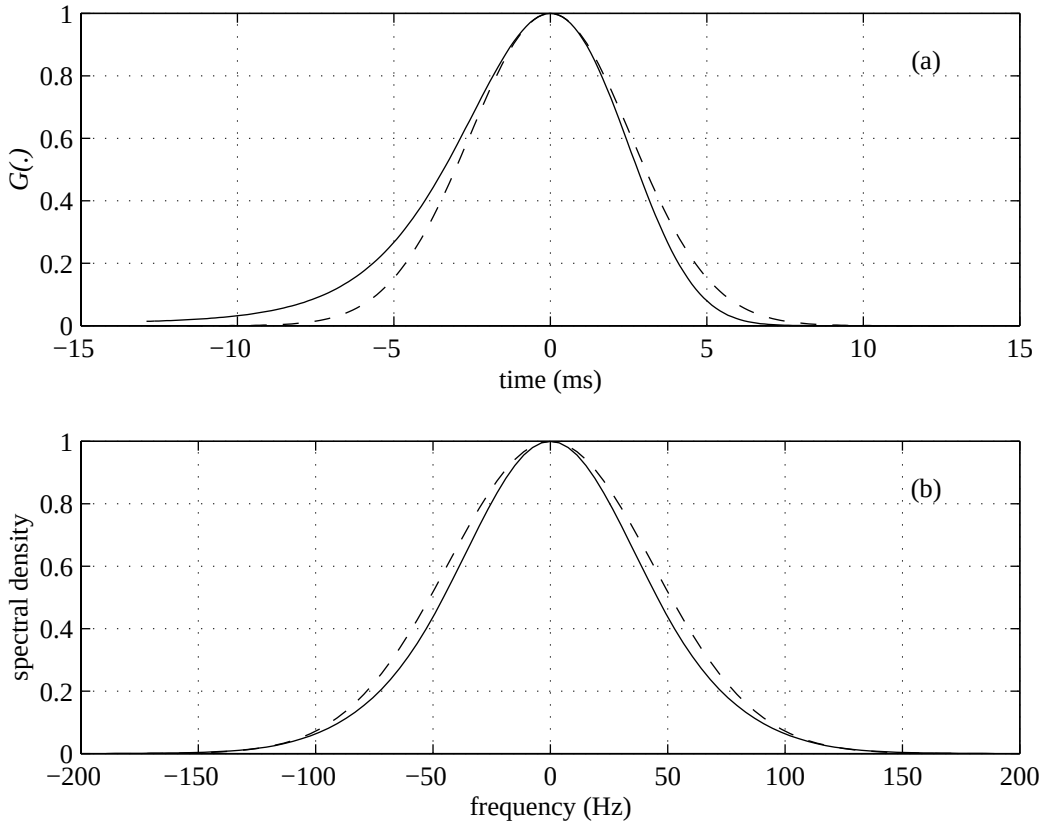

Figure 6.1: Effect of acceleration on (a) $G = \exp\left(\frac{-\left(v(0)t+at^2/2\right)^2}{2\,\sigma_{\rm sv}^2}\right)$ and (b) its spectrum. $v(0) = 0.775$ m s^{-1}, $\sigma_{\rm sv} = 2$ mm. Dashed line - $a = 0$ m s^{-2}, continuous line - $a = 50$ m s^{-2}.

Their normalised energy spectra are shown in figure 6.1b. The rms width of the $a = 0$ m s^{-2} and $a = 50$ m s^{-2} spectra are 43.6 Hz and 42.6 Hz respectively. Note that the difference (1 Hz) is negligibly small. For flow conditions giving I_d values of 0.083 or less it is clear that the effect of acceleration on intrinsic spectral broadening may be neglected.

6.2.2 Effect of velocity profile and sample volume size.

In steady flow the spectrum is unchanging, the window can be sufficiently large to have a negligible broadening effect and there is clearly no non-stationarity broadening. The spectrum shape and width are determined solely by the sensitivity variation within the sample volume and the velocity profile.

In general there is no closed form expression for the spectrum shape and width and these are found only for particular cases.

Uniform sensitivity and n^{th} power profile

One of these cases, uniform sensitivity over the vessel cross-section with a sample volume width in the direction of flow sufficiently wide such that intrinsic broadening is negligible, together with a velocity profile of the form:

$$v_q = v_0 \left(1 - (r_q/R_0)^n\right) \tag{6.23}$$

where r_q is the distance of the elemental tube q from the centre of the vessel and v_0 is the velocity at the centre of the vessel, is well known (see for example [Fish 1986]). In this case:

$$S(\omega) = \frac{C2\pi R_0^2}{n\,|\omega_{d0}|\,(1-\omega/\omega_{d0})^{(1-2/n)}}\left(U(\omega) - U(\omega-\omega_{d0})\right) \tag{6.24}$$

where $U(\omega)$ is the unit step function and C is a constant depending on instrument sensitivity and blood backscatter.

For a parabolic profile ($n = 2$) the spectrum is constant from zero to ω_{d0}. The rms width, from (2.39) and (6.24) is:

$$\sigma = \frac{|\omega_{d0}|}{2\pi}\frac{n}{n+2}\sqrt{\frac{1}{n+1}} \tag{6.25}$$

Figure 6.2 shows the power law velocity profile and the normalised Doppler spectrum for $n = 2, 4$ and 8.

Gaussian sample volume and n^{th} power profile

Another case for which closed form expressions exist is the one of a Gaussian sample volume in a power law velocity profile (6.23).

An analytical expression (5.32) for the Doppler spectrum from a generic Gaussian sample volume placed anywhere in a vessel with a power law velocity profile was derived in Chapter 5. Plots of the Doppler spectrum for Gaussian sample volumes of various sizes placed at different positions in a blood vessel can also be found in Chapter 5 (figure 5.2).

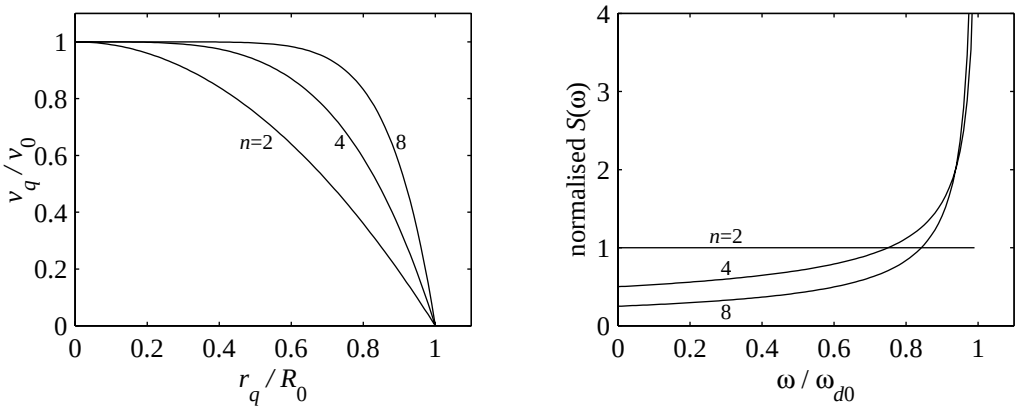

Figure 6.2: Velocity profile and normalised Doppler spectrum for $n = 2, 4$ and 8. The spectra were normalised to have a unit area below the curve.

6.2.3 Intrinsic spectral broadening.

It is not easy to see how the effect of intrinsic spectral broadening on the spectrum as a whole rather than the components arising from individual streamlines can be calculated. The difficulty arises because the width of $G(.)$ as a function of time depends on the velocity of the streamline as well as the sensitivity variation ($G(.)$ as a function of distance) along the streamline. It is therefore not possible to separate this factor out from (6.8). However, if we restrict attention to the case when the range of velocities within the sample volume is small (small sample volume and/or sample volume centred in blunt profile flow) then $v_{qm}(t_w)$ and $v_{dqm}(t)$ may be replaced by the spatial mean velocities within the argument of $G(.)$. If, further, we restrict attention to the case where the shape of $G(.)$ and width (as a function of x or t) is approximately independent of y and z (or q) and changes only in amplitude between streamlines, then the signal from each element in (6.8) is multiplied by a time function having the form:

$$G\left(x_{qm}(t_w) + \overline{v}(t_w)(t - t_w) + \int_{t_w}^{t} \overline{v}_d(\tau)\, d\tau, y_0, z_0\right) \tag{6.26}$$

where y_0 and z_0 are the y and z coordinates of the sample volume centre. Thus the base-band spectrum $S_b(\omega)$ can be written:

$$S_b(\omega) = S_{b_1}(\omega) * S_G(\omega) \tag{6.27}$$

where $S_{b1}(\omega)$ and $S_G(\omega)$ are the baseband spectrum without intrinsic broadening and the energy spectrum of $G\left(\overline{v}(t_w)(t - t_w) + \int_{t_w}^{t} \overline{v}_d(\tau)\, d\tau, \overline{y}, \overline{z}\right)$ respectively (note that the constant

$x_{qm}(t_w)$ does not affect the spectrum). In this case we can also write:

$$\sigma_b = \sqrt{\sigma_{b1}^2 + \sigma_G^2} \tag{6.28}$$

where σ_{b1} and σ_G are the rms widths of $S_{b1}(\omega)$ and $S_G(\omega)$ respectively.

Although we have derived this result under the condition of small velocity range we expect to be able to use (6.28) more widely since an increasing velocity range leads to a higher σ_{b1}, thereby dominating σ_G and making inaccuracy in this irrelevant.

6.2.4 Variation of acceleration

Note that, referring back to (6.8), σ_{b1} is determined not only by the mid-window range of velocities $v_{qm}(t_w) - \overline{v}(t_w)$ within the sample volume but also by the variation of acceleration within the sample volume and window - determined by the term $\int_{t_w}^{t} (v_{dqm}(\tau) - \overline{v}_d(\tau))d\tau$. It is not easy to see how to separate the effect of these terms without *a priori* knowledge of the time-varying profile. In an attempt to overcome this problem we briefly explore the effect of assuming that σ_{b1} is dominated by the effect of the mid-window velocity variation and that the effect of acceleration variation is negligible.

If the acceleration for each streamline is approximately constant in time and the range of accelerations within the sample volume is Δa then the error in the spectral width σ_{b1} arising from the assumption that Δa is negligible will be $\epsilon_r \simeq \sigma_t \omega_0 \Delta a \cos(\theta)/(\pi c)$.

The magnitude of this error can be estimated for typical flow patterns by using equations (4.21) to (4.23). For example, using a velocity waveform typical of that found in the femoral artery, a transmitted frequency of 5 MHz, a centred sample volume with a width of 0.5 of the vessel diameter and $\sigma_t = 5.66$ ms (corresponding to a Hanning window width of 40 ms), the velocity, acceleration range and ϵ_r have been calculated and shown in figure 6.3.

The maximum error, within the accelerative phase of systole is approximately 40 Hz. It will be lower for smaller sample volumes and window durations.

6.2.5 Approximate spectral width.

It follows from the above that, under the conditions specified, (6.15), (6.19) and (6.28) may be combined to give:

$$\sigma = \sqrt{\sigma_{b1}^2 + \sigma_G^2 + \sigma_w^2 + \beta^2 \sigma_t^2} \tag{6.29}$$

noting that acceleration may be neglected in calculating σ_G and that, if the range of acceleration within the sample volume may be neglected and the sample volume is symmetrical Gaussian and centred on the vessel carrying blood with a power-law profile, closed form expressions exist for all the terms in (6.29). Specifically, σ_{b1} is given by (5.51), σ_G is the rms width of the energy spectrum of $\exp\left(-\frac{\overline{v}_d^2 t^2}{2\sigma_{\rm sv}^2}\right)$, $\left(\sigma_G = \frac{\overline{v}_d}{2\pi\sigma_{\rm sv}\sqrt{2}}\right)$, σ_w is the rms width of the energy spectrum of the window (given by (6.13) for the Hanning window), $\beta\sigma_t$ is given by

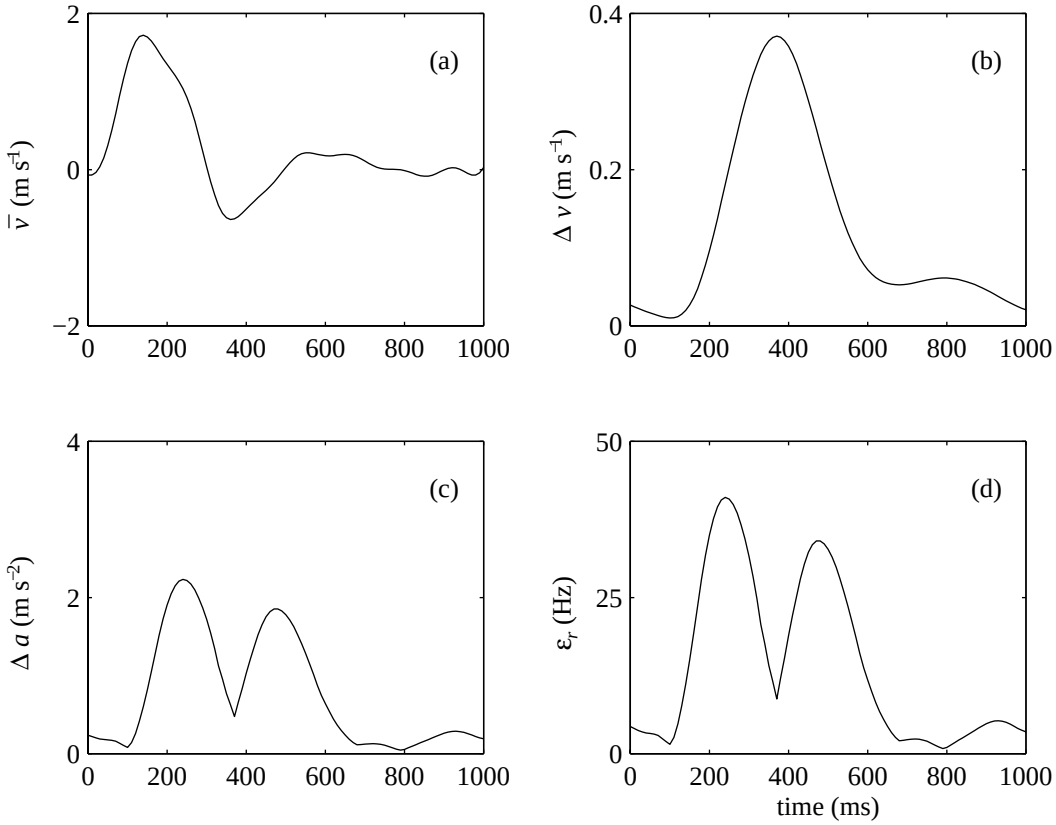

Figure 6.3: Derivation of typical error in spectral width assuming acceleration range in sample volume is negligible. (a) Mean velocity waveform $\bar{v}(t)$ (m s^{-1}). (b) Maximum-minimum velocity Δv (m s^{-1}) in radius range 0–0.5R_0. (c) Maximum-minimum acceleration Δa (m s^{-2}) in radius range 0–0.5R_0. (d) Acceleration related error in spectral width ϵ_r (Hz).

(6.17) and σ_t (the rms width of the window function squared) is given by (6.18) for a Hanning window.

Figure 6.4 shows the expected spectral broadening due to each of the factors considered separately: window broadening, nonstationarity broadening, transit time broadening and the spectral width due to the range of velocities passing through the sample volume.

The plot for the transit time broadening is computed for a streamline velocity of 1 m s^{-1}. For a given sample volume σ_G is proportional to velocity. It can be seen that for nonstationary Doppler signals an increase of the window duration affects the spectral width in two opposite directions; it decreases window broadening but increases the nonstationary broadening. The sample volume size also affects the spectral width in two ways; for a specific velocity profile a larger sample volume reduces transit time broadening but increases the spectral width as a result of the velocity range increase. Note that this will only be true if we consider sample volume change without shape change since the spatial velocity variation is in a plane orthogonal to the axis along which transit-time broadening is determined.

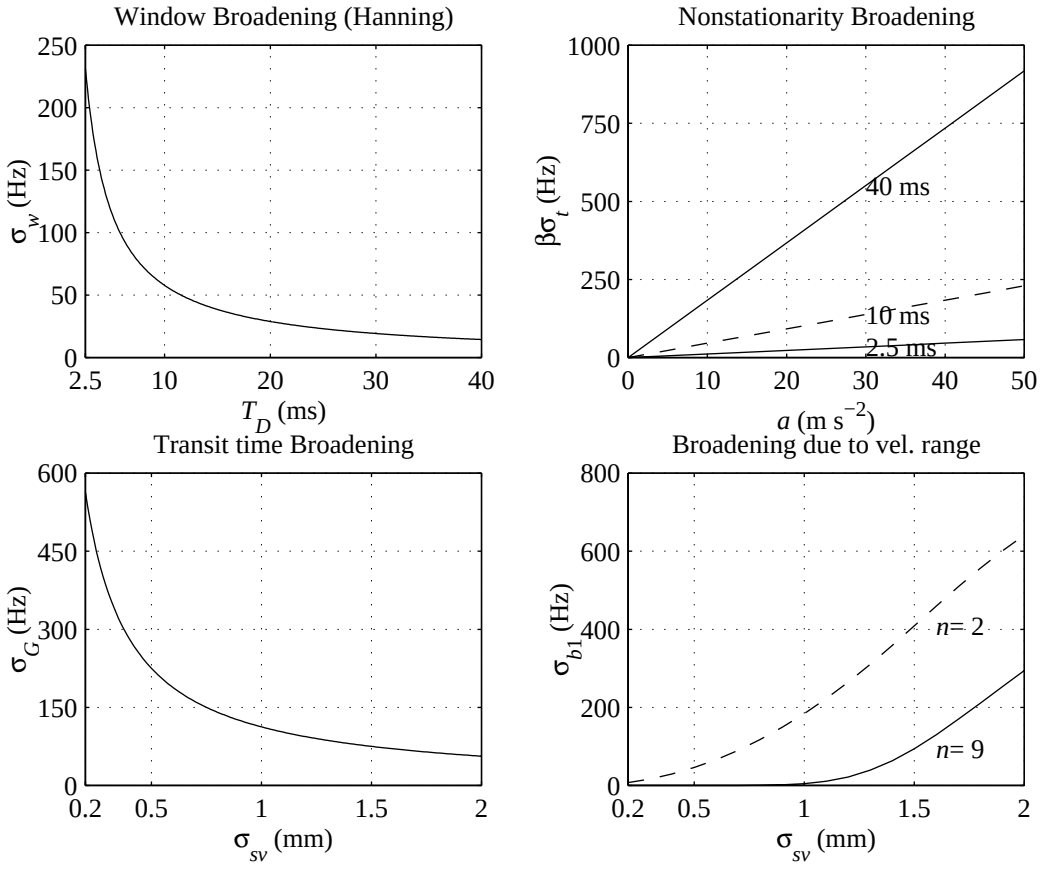

Figure 6.4: Spectral width due to each of the broadening factors. The data was obtained with the following parameters: transmitted frequency, 5 MHz; $\theta = 60^{\circ}$; $c = 1540$ m s^{-1} and $R_0 = 4.2$ mm. The transit time broadening displayed is for a single streamline in the centre of the vessel with $v_0 = 1$ m s^{-1}.

6.3 Simulation experiments

Unfortunately, in the general case when the spectral width is dependent on the range of velocities within a non-centred sample volume and/or having a non-Gaussian sensitivity function together with window and acceleration-induced broadening a simple expression is not available and it is necessary to find the spectrum from numerical calculations. However, it is possible to use the theoretical results of the preceding sections to calculate the spectral width in limited circumstances and it is the purpose of the following experiments to compare the results of the spectral width estimation given by the approximate formula (6.29) with those given by the computer signal model in order to gauge its accuracy over a range of flow and measurement conditions.

The experiments were carried out with the same parameters as used in Chapter 4 (page 89), the sample volume was Gaussian with spherical symmetry and with a sensitivity variation

given by

$$G(x, y, z) = e^{-\frac{x^2+y^2+z^2}{2\sigma_{\mathrm{sv}}^2}} \tag{6.30}$$

where σ_{sv} is the rms width of the sample volume that was varied from 0.2 mm to 2.0 mm and the model computed the signal from elemental volumes within $-4\sigma_{\mathrm{sv}}$ and $+4\sigma_{\mathrm{sv}}$.

The blood acceleration was varied from 0 to 50 m s^{-2}. Kikkawa et al. [1987] in their study used an acceleration of 42 m s^{-2} for the blood flow in the ascending aorta of the dog and Milnor [1989] says that the maximum blood acceleration in the dog is in the range 50–80 m s^{-2} and that the acceleration in man is somewhat lower.

The simulated Doppler signals were windowed with Hanning windows of duration: 2.5 ms, 10 ms and 40 ms. The expected ensemble averaged power spectra were computed by adding the power spectra of each elemental volume as described in section 4.3.

Firstly, the spectrum from a single streamline was calculated for steady and accelerating flow to check the agreement between model and theoretical predictions at this level. Next the spectral width for a range of sample volume sizes, accelerations, window durations and velocity ranges for a vessel-centred Gaussian sample volume in power-law flow for a range of measurement conditions was calculated using the Doppler signal model and the error between these calculations and the estimate using (6.29) was calculated.

6.4 Results

6.4.1 Single streamline

Intrinsic broadening dominant

Figure 6.5 presents the variation of the Doppler spectral width when it is dominated by intrinsic spectral broadening. The spectra were generated for a single streamline with constant velocity of 1 m s^{-1} and the simulated signals were multiplied by a 1 s Hanning window, sufficiently long to reduce window broadening to a negligible level. The expected spectral width, which is $v/\left(2\sqrt{2}\pi\sigma_{\mathrm{sv}}\right)$, was computed from the theoretical Doppler spectrum for a Gaussian sample volume from a single streamline (4.26).

Non-stationarity broadening dominant

With a combination of relatively long window duration and high acceleration we expect the width of the Doppler spectrum to be dominated by nonstationarity broadening. Figure 6.6 shows the variation of the spectral width with acceleration for a single streamline of velocity $v(t) = 1 + at$ m s^{-1} passing through a sample volume with $\sigma_{\mathrm{sv}} = 2.0$ mm (large sample volume to reduce intrinsic broadening), the signal was windowed by a 40 ms Hanning window. The straight line was computed from (6.17).

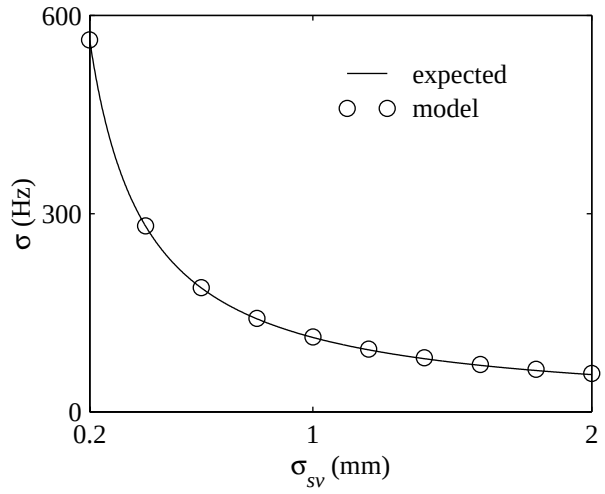

Figure 6.5: Variation of rms spectral width of the simulated signal from a streamline as a function of sample volume size, $v(t) = 1$ m s^{-1} and $T_D = 1$ s.

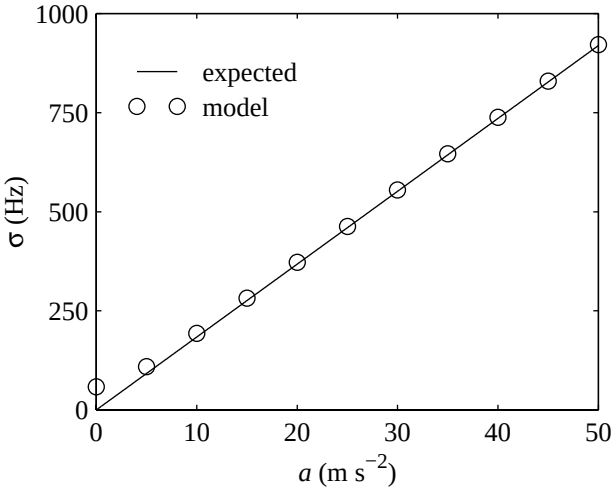

Figure 6.6: Variation of rms spectral width of the simulated signal from a single streamline as a function of blood acceleration, $\sigma_{\rm sv} = 2.0$ mm and $T_D = 40$ ms. The straight line represents the spectral width due solely to nonstationarity broadening.

The deviation, at low accelerations, of the model results from the expected straight line results from transit time broadening becoming important as the acceleration approaches zero.

From figures 6.5 and 6.7 we see that the model generates signals with spectral characteristics similar to those expected. For very specific cases where the intrinsic and nonstationarity broadening effects can be individually evaluated, the width of the spectra computed with the model is very close to the expected values.

6.4.2 Velocity profile

It is not possible to investigate every possible combination of flow and measurement condition. So, in order to find a suitable profile shape for testing equations (4.21–4.23 were used to compute the time-varying velocity profile for the CFA velocity waveform used to simulate the signal whose sonogram is displayed in figure 4.11. The velocity profile in the mid systolic accelerative phase of the CFA velocity waveform was found to be approximately $v_0\left(1-(r/R_0)^9\right)$ and this profile has been used as the basis of the next test.

Figure 6.7 shows the expected ensemble averaged spectra for a range of blood acceleration, sample volume size and window duration. The blood velocity was:

$$v(r,t) = (v_0 + a(t-t_w))\left(1-\left(\frac{r}{R_0}\right)^n\right), \qquad -T_D/2 < (t-t_w) < T_D/2 \tag{6.31}$$

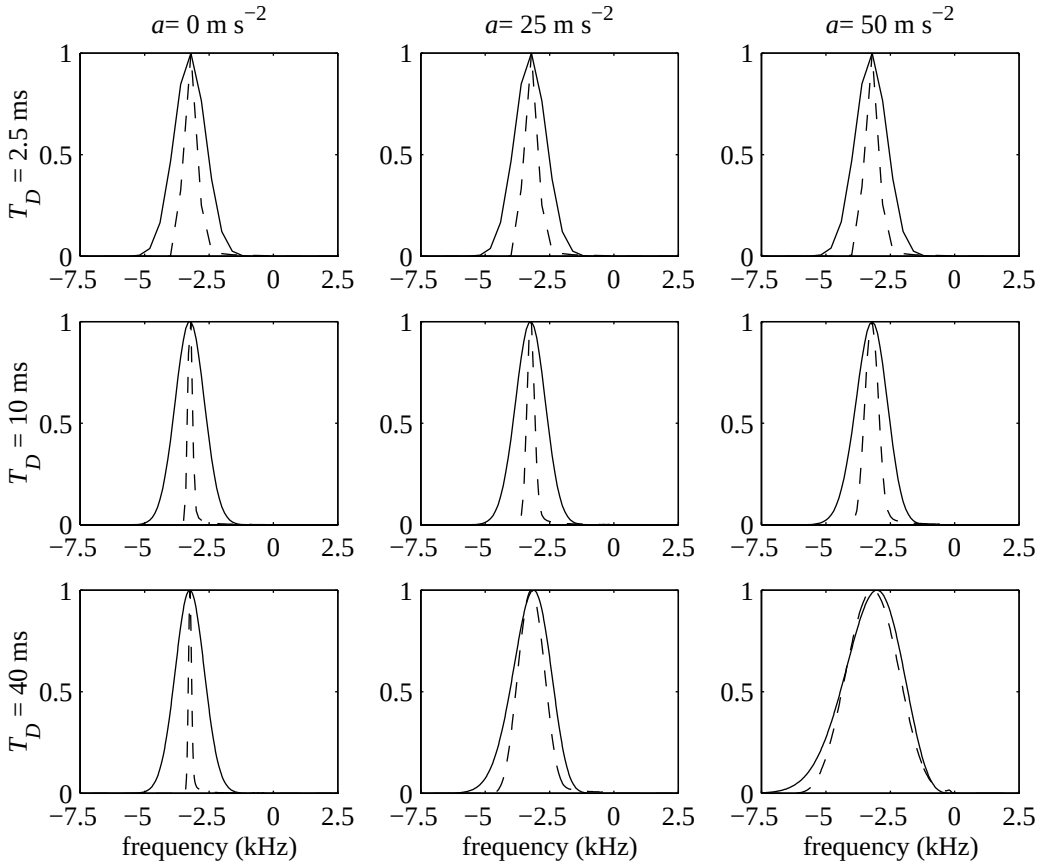

Figure 6.7: Normalised power spectrum of the simulated signal from a 4.2 mm radius vessel. The velocity profile is $v(r,t) = (1+a(t-t_w))\left(1-(r/R_0)^9\right)$ m s^{-1}. Each signal was windowed by a Hanning window with time duration T_D, the sample volumes are Gaussian with σ_{sv}: —— 0.2 mm and · · · 2.0 mm. The spectra were normalised by dividing by their maximum power.

with $v_0 = 1$ m s^{-1} and $n = 9$ and all the sample volumes were spherically symmetric Gaussian and centred in a vessel of radius 4.2 mm.

The widths of the spectra are shown plotted against window duration and acceleration for sample volume widths 0.2, 1.0 and 2.0 mm in figure 6.8a and against sample volume width and acceleration for window durations 2.5, 10 and 40 ms in figure 6.8c. In each case investigated the approximate spectral width given by (6.29) was calculated and the % error in this width compared with that calculated from the model plotted in figures 6.8b and d respectively.

It is clear from figures 6.7, 6.8a and 6.8c that, as expected, acceleration has little impact on the spectral shape and width when the window duration is small, only becoming noticeable for window durations greater than 10 ms. For high duration windows and high accelerations the effect is clearly dominant. Spectral shape skewing [Cloutier et al. 1993] is also only really noticeable at the high window duration-acceleration combinations (figure 6.7). Window broadening, as expected from consideration of figure 6.4, only becomes significant for window durations well below 10 ms and is dominant (figure 6.8c) for mid-range sample volume sizes ($\sigma_{\rm sv}/R_0 \sim 1/4$). The opposing effects of sample volume size are clearly shown in figure 6.8c where the spectral width increases at low $\sigma_{\rm sv}$ as a result of increasing intrinsic spectral broadening and at high $\sigma_{\rm sv}$ as a result of the increased velocity range.

As can be seen from figure 6.8b and d the estimation of spectral width using (6.29) is good over the whole range of conditions studied for this blunt profile.

Although unlikely to be found in practice it is useful to consider an accelerating parabolic profile as an extreme case. Therefore the above test was repeated with $n = 2$ in equation (6.31) and the corresponding results are shown in figure 6.9. As expected the errors are greater, particularly at high acceleration, window duration, and sample volume size combinations. Nevertheless, (6.29) still leads to a reasonable approximation as long as the extremes are avoided.

The increased error is expected as a result of the increased range of acceleration in the $n = 2$ case because of our inability to separate the effects of spatial velocity and acceleration variation and the neglect, in deriving (6.29), of the effect of acceleration variation. As has been shown the magnitude of the resulting error is dependent on $\epsilon_r = \sigma_t \omega_0 \Delta a \cos(\theta)/(\pi c)$ where Δa is the range of acceleration within the sample volume. Identifying the range $r = 0 \rightarrow \sigma_{\rm sv}$ over which Δa is calculated then, from (6.31):

$$\Delta a = \frac{\partial v}{\partial t}(0, t_w) - \frac{\partial v}{\partial t}(\sigma_{\rm sv}, t_w) = a \left(\frac{\sigma_{\rm sv}}{R_0}\right)^n \tag{6.32}$$

and

$$\epsilon_r = \frac{\sigma_t a\, \omega_0 \cos(\theta)}{\pi c} \left(\frac{\sigma_{\rm sv}}{R_0}\right)^n \tag{6.33}$$

It should be noted that this error estimate is fairly crude and should be taken only as a guide

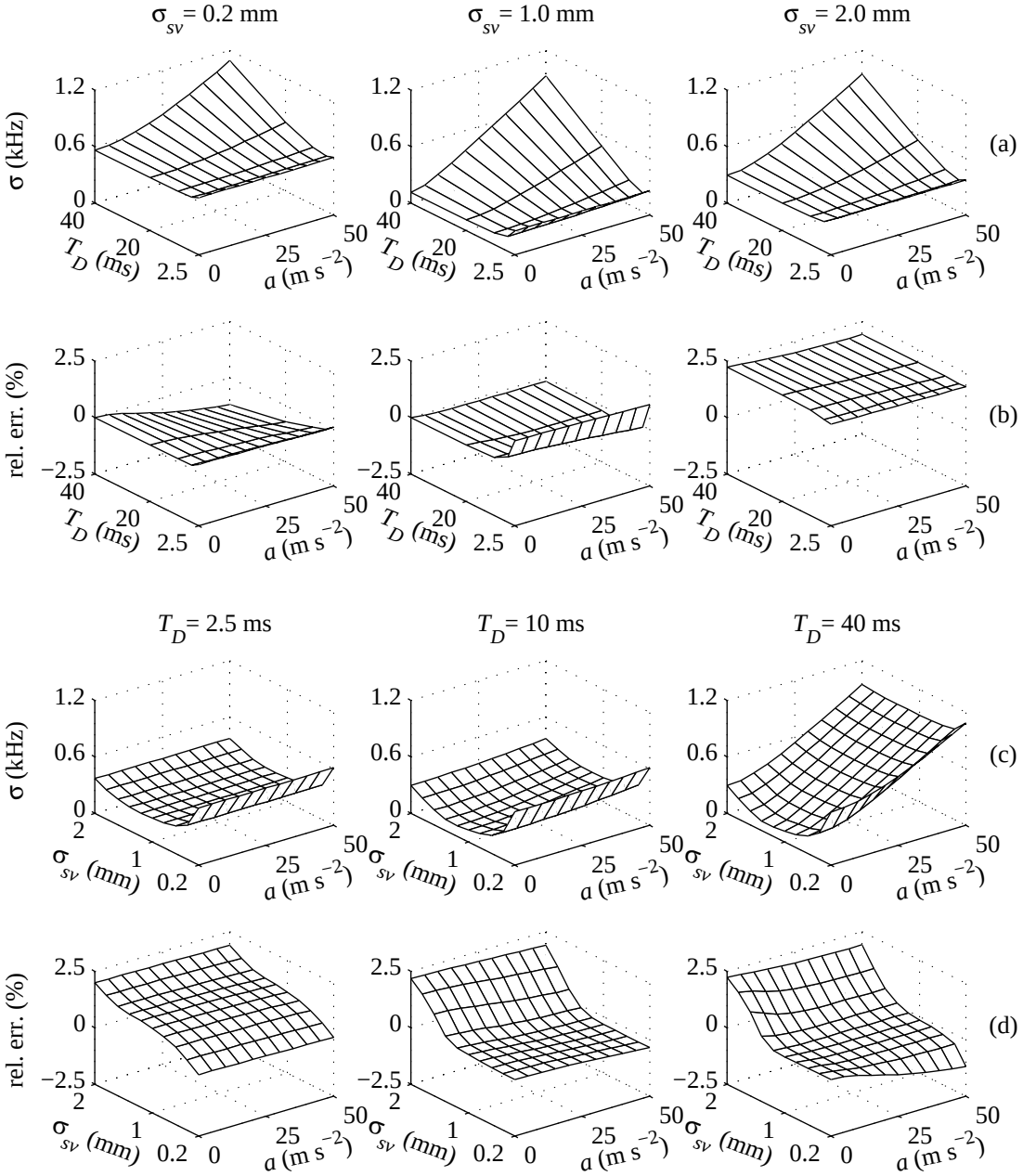

Figure 6.8: RMS spectral width calculated using model and difference between this and simple width estimation formula (6.29) for $n = 9$ profile. (a) spectral width *versus* window duration and acceleration for three sample volume widths. (b) Percentage error in width calculated using (6.29) compared with width from model. (c) spectral width *versus* sample volume width and acceleration for three window durations. (d) Percentage error in width calculated using (6.29) compared with width from model.

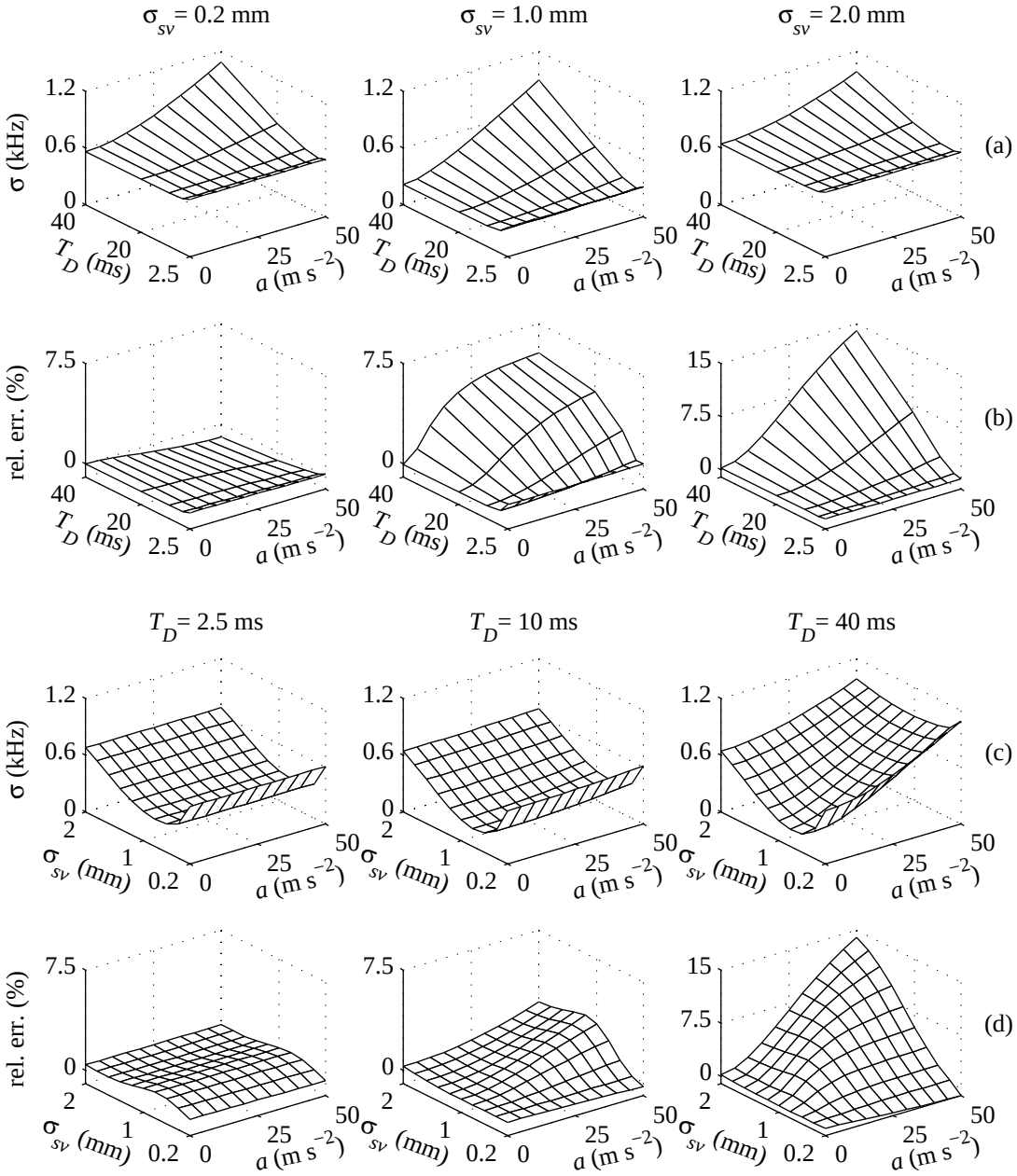

Figure 6.9: RMS spectral width calculated using model and difference between this and simple width estimation formula (6.29) for $n = 2$ profile. (a) spectral width *versus* window duration and acceleration for three sample volume widths. (b) Percentage error in width calculated using (6.29) compared with width from model. (c) spectral width *versus* sample volume width and acceleration for three window durations. (d) Percentage error in width calculated using (6.29) compared with width from model.

to the combination of σ_t, a and σ_{sv}/R_0 at which (6.29) becomes inaccurate.

The maximum ϵ_r within model range occurs when $T_D = 40$ ms ($\sigma_t = 5.66$ ms), $\sigma_{sv} = 2$ mm and $a = 50$ m s^{-2}. Then, $\epsilon_r = 208$ Hz for $n = 2$ and 1.2 Hz for $n = 9$. It can be seen that this is a fair agreement with the error shown in figure 6.9. The higher error than expected in the $\sigma_{sv} = 2.0$ mm, $n = 9$ case (figures 6.8b, d) is probably due to the assumption that intrinsic broadening is governed by the mid-sample volume streamline - an assumption that will begin to break down as the sample volume increases in size. This effect will be swamped by the increase in velocity range in the $n = 2$ case.

Overall it is reasonable to assume that as long as ϵ_r is small then we can expect (6.29) to give good estimations of rms spectral width. We have already seen that ϵ_r can be expected to be reasonably low for a typical femoral artery waveform.

6.5 Concluding remarks

A new formulation for the Doppler signal generation process in pulsatile flow has been developed enabling easier identification and quantification of the mechanisms involved in spectral broadening and the development of simple estimation formula for the measured rms spectral width. The accuracy of the estimation formula was tested by comparing it with the spectral widths found by using conventional spectral estimation on simulated Doppler signals generated using our model described in chapter 4.

The model assumes nonturbulent pulsatile flow parallel to the vessel wall and considers that neighbour red blood cells have similar velocities so that their signals can be considered as if arising from an elemental volume. Elemental volumes at a constant distance from the vessel axis are grouped into an elemental tube. These assumptions are acceptable for slow varying laminar velocity profiles and away from regions of high velocity gradient (dv/dr).

It is shown that when the spectral width is dominated by any of the spectral broadening effects studied here, our Doppler signal model generates simulated signals whose spectral width agrees very well with the predicted values. Therefore, it is reasonable to extrapolate the validity of the results for situations where none of the spectral broadening effects dominates over the others.

The influence of acceleration, sample volume size and time window duration on the Doppler spectral width was investigated for a blunt velocity profile passing through spherically symmetric Gaussian shaped sample volumes. This represents a somewhat idealised sample volume shape for investigating these influences but is, nevertheless, a useful starting point.

Our results show that for short duration windows, the spectral width is dominated by window broadening and that acceleration has a small effect on the spectral width. For long duration windows the effect of acceleration must be taken into account.

The size of the sample volume affects the spectral width of the Doppler signal in two ways; by intrinsic broadening and by the range of velocities passing through it. Since these

effects act in opposite directions it is reasonable to say that for each velocity field there must exist a sample volume size that minimises the spectral broadening.

The simple spectral width estimation formula was shown to have excellent agreement with widths calculated using the model and indicates the potential for correcting not only for window and non-stationarity broadening but also for intrinsic broadening.

It should be emphasised that the spectral width results indicate that a relatively simple method of estimation is accurate only in as much as the assumptions of the underlying model are valid. More realistic models are being developed by our research group and by other investigators and the findings here will need to be updated. In particular the dependence of local backscatter cross-section on the local time-varying velocity field will have to be incorporated when work in this area is more advanced.

In addition it is recognised that the theoretical results presented here require experimental validation.

Chapter 7

Conclusion

7.1 General conclusions

The Doppler ultrasonic flow detector has been extensively used in the last forty year to assess the cardiovascular system. It is a non-invasive technique that uses ultrasonic waves, which are non-ionising, and the Doppler effect to measure the velocity of blood in vessels of human beings. The Doppler ultrasonic flow detector estimates the blood velocity by measuring the shift in frequency between the transmitted and the received waves.

The Doppler signal, which is the output of the flow detector, is stochastic because it is the sum of the signals backscattered by a random distribution of blood cells. The Doppler signal is also pulsatile due to the pumping action of the heart and as a consequence the signal is not a stationary stochastic process, it is approximately cyclo-stationary. Both the shape and the width of the time-varying Doppler spectrum are of clinical interest; usually an altered shape or an increased spectral width is a sign of a diseased blood vessel.

The random pulsatile nature of the Doppler signal and its high variability from person to person and with time (in the same person) make *in vivo* signals not particularly suitable for testing signal processing methods. The characteristics of *in vivo* Doppler signals cannot be controlled and because of the randomness usually only estimates of the characteristics are available. Simulated signals generated by a model are normally used as test signals.

Besides providing us with test signals with controllable characteristics, models usually contribute to improve our knowledge of the process being modelled. Since models are so valuable we developed a model for generating simulated Doppler signal.

The Doppler signal model inputs are the characteristics of the lower limb arterial tree and the characteristics of the ultrasonic sample volume and it outputs simulated Doppler signals with characteristics similar to those measured *in vivo*. The model developed is particularly suited for studying Doppler signals from accelerative and decelerative blood flow.

The model for the Doppler signal that we developed was divided in two sub-models, one for simulating blood flow in the lower limb and another to simulate the inter-action between

the velocity and ultrasonic fields.

The blood flow model is an electric analogue of the lower limb circulation and generates flow and pressure waveforms whose shapes are similar to those expected. The amplitude of the flow waveform decreases as it moves to the periphery while the pulsatility index increases as usually happens in the normal lower limb. The amplitude of the pressure waveform is amplified by the reflections at the branches and other impedance mismatches.

For modelling the inter-action between the velocity and ultrasonic fields we divided the vessel into small elemental volumes and added the contributions of all the elemental volumes passing through the sample volume. The characteristics of the simulated Doppler signals are similar to those predicted on theoretical grounds. We tested our sub-model in situations were one broadening effect clearly dominates over the others and then compared the experimental spectral width with that predicted; usually the model results agreed very well with the predictions.

Using our model we studied the influence of acceleration, sample volume size and time window duration on the Doppler spectral width of signals obtained from a blunt profile passing through spherically Gaussian shaped sample volumes. Our results show that the effect of acceleration must be taken into account when long duration windows are used and that for short duration windows the spectral width is dominated by window broadening. The size of the sample volume affects the spectral width of the Doppler signal in two ways; by intrinsic broadening and by the range of velocities passing through it. Since these effects act in opposite directions it is reasonable to say that for each velocity field there must exist a sample volume size that minimises the spectral broadening.

A simple formula for estimating the spectral of Doppler signals was proposed in this work. The spectral widths computed with the formula agree well with the widths computed from the signals simulated by the model in various situations. This simple formula has probably the potential to allow for correction of windows broadening, non-stationarity broadening and intrinsic broadening.

We believe that the work described here is a contribution, though a small one, to improve the understanding of the Doppler signal and the effects of various factors on the Doppler spectral width. It also contributes to setting up the basis for the development of model based vascular disease detection. To achieve this latter goal the blood flow model must be improved in future (see the next section).

Our model generates simulated Doppler signals with controllable characteristics thus enabling their use as test signals during the development stages of new signal processing techniques. The model also enabled to study the effect of acceleration, sample volume size and data window duration on the Doppler spectral width.

7.2 Recommendations for future work

A model of any system represents our knowledge of the system and there is always the possibility for improving its representation of the real system. The improvement may be achieved in various ways, for example by lifting some of the model constraints or by improving the accuracy with which particular features of the system are modelled.

We indicate below some possible research lines for future work in this project.

One limitation of the lower limb blood flow model described in Chapter 3 is its inability to simulate the peculiarities of blood flow around branches and stenoses. It would be interesting to use the pressure and flow waveforms generated by the lower limb model to drive detailed models of flow around branches and stenoses. This could probably be achieved using Computational Fluid Dynamic (CFD) techniques to numerically solve the Navier-Stokes equation in the branches and the stenoses. Note that if stenoses are to be modelled the current model must be changed to account for the pressure drop experienced at a stenosis.

Another interesting improvement to the blood flow model would be to make the estimation of the model parameters an iterative process. The model would adjust autonomously its parameters to minimise the differences between its outputs and the waveforms measured in the lower limb arterial tree. This would make it possible to introduce a feedback loop capable of simulating the autonomous regulation of blood flow. Disease states and disease induced alterations, such as the opening of collaterals, could also be introduced into the lower limb model after an extensive investigation of their effect on blood flow, both on a local and sistemic scale.

The feedback mechanisms would permit the study of the influence of various vasomotor states on the blood flow and pressure waveforms and would, eventually, be a significant contribution to achieve model based arterial disease detection.

SPICE was a good option to implement the electric analogue of blood flow in the lower limb because it is very easy to change the model parameter during the development phase. However in future, if iterative selection of model parameters and feedback mechanisms are to be introduced into the blood flow model it will probably be better to use other techniques, such as scattering matrices, capable of simulating the circuit much faster than SPICE.

Experimental work should be carried out to validate *in vitro* the model for the inter-action between the velocity and ultrasonic fields presented in Chapter 4. This would require setting up an experiment for measuring and characterising the sample volume of a real Doppler flow detector.

Other interesting improvements to the model would be the implementation of sample volumes with diverse shapes corresponding, if possible, to real sample volumes produced by blood flow detectors. The model could probably be altered to lift the restriction of modelling laminar flow, extending its applicability to helical flow which is sometimes encountered in

the major vessel [Kilner et al. 1993].

The simple formula estimating the rms spectral width of the Doppler signal, which was derived in Chapter 6 from our Doppler model needs to be tested with *in vitro* experiments. The theoretical derivation of the formula and the numerical model against which the results were checked share the same assumptions, the experimental validation of the results would make the formula more useful.

As pointed out in Chapter 4 the local blood backscatter cross-section depends on the local time-varying velocity field (see for example, [Bascom et al. 1988, Cloutier & Shung 1993, Mo & Cobbold 1992, Wu & Shung 1996]). When more is known about this dependence and quantitative data is available the phenomenon should be incorporated into our Doppler signal model.

Finally we would like to propose the construction of a large scale database with typical *in vivo* Doppler signals characteristic of various disease stages and of normality. This would make the testing of new signal processing techniques easier and would allow the development of automatic classification techniques for the Doppler signal. It would also allow to compare the results of Doppler models with standard *in vivo* signals.

Similar databases exist or are under construction in other areas of biomedical engineering research such as in the processing of electroencephalogram signals.

Appendix A

Evaluation of function $\mathrm{M}(a, b, \beta)$ from chapter 5

In order to evaluate the following integral

$$\mathrm{M}(a, b, \beta) = \int_0^{2\pi} \exp\left(a\cos(\phi - \beta) + b\cos(2\phi)\right)\, d\phi \tag{A.1}$$

we note that $\exp(a\cos(\phi))$ can be expressed as a series of modified Bessel functions [Abramowitz & Stegun 1972, p. 376]. So the terms in the integrand of equation (A.1) can be written as:

$$\exp(a\cos(\phi - \beta)) = \mathrm{I}_0(a) + 2\sum_{k=1}^{\infty} \mathrm{I}_k(a)\cos(k(\phi - \beta)) \tag{A.2}$$

$$\exp(b\cos(2\phi)) = \mathrm{I}_0(b) + 2\sum_{n=1}^{\infty} \mathrm{I}_n(b)\cos(2n\phi) \tag{A.3}$$

Multiplying term by term and expanding $\cos(k(\phi - \beta))$ we obtain:

$$\begin{aligned}
\mathrm{M}(a, b, \beta) = &\int_0^{2\pi} \mathrm{I}_0(a)\mathrm{I}_0(b)\, d\phi \;+\; 2\,\mathrm{I}_0(a)\int_0^{2\pi} \sum_{n=1}^{\infty} \mathrm{I}_n(b)\cos(2n\phi)\, d\phi \\
&+ 2\,\mathrm{I}_0(b)\int_0^{2\pi} \sum_{k=1}^{\infty} \mathrm{I}_k(a)\cos(k(\phi - \beta))\, d\phi \\
&+ 4\int_0^{2\pi} \sum_{k=1}^{\infty} \left\{ \mathrm{I}_k(a)\cos(k\beta)\cos(k\phi) \sum_{n=1}^{\infty} \mathrm{I}_n(b)\cos(2n\phi) \right\} d\phi \\
&+ 4\int_0^{2\pi} \sum_{k=1}^{\infty} \left\{ \mathrm{I}_k(a)\sin(k\beta)\sin(k\phi) \sum_{n=1}^{\infty} \mathrm{I}_n(b)\cos(2n\phi) \right\} d\phi
\end{aligned} \tag{A.4}$$

The 2nd, 3rd and 5th right hand terms of equation (A.4) are zero for all k, n, and the 4th

term is not zero only for $k = 2n$. Its value is:

$$4\pi \sum_{k=1}^{\infty} \mathrm{I}_{2k}(a)\mathrm{I}_k(b)\cos(2k\beta) \tag{A.5}$$

and the complete integral is,

$$\mathrm{M}(a, b, \beta) = 2\pi \left[\mathrm{I}_0(a)\mathrm{I}_0(b) + 2 \sum_{k=1}^{\infty} \mathrm{I}_{2k}(a)\mathrm{I}_k(b)\cos(2k\beta) \right] \tag{A.6}$$

References

Abramowitz, M. & Stegun, I. A., eds [1972], *Handbook of Mathematical Functions with Formulas, Graphs, and Mathematical Tables*, Dover Publications, New York. {105,137}

Aldis, G. K. & Thompson, R. S. [1992], 'Calculation of Doppler spectral power density functions', *IEEE Transactions on Biomedical Engineering* **39**(10), 1022–1031. {35,100,103,112}

Angelsen, B. A. J. [1980], 'A theoretical study of the scattering of ultrasound from blood', *IEEE Transactions on Biomedical Engineering* **27**(2), 61–67. {33,34,40,80,89}

Angus, J. C., Edwards, R. V. & Dunning, Jr., J. W. [1971], 'Signal broadening in the laser Doppler velocimeter', *AIChE Journal* **17**(6), 1509–1510. {37}

Ata, O. W. & Fish, P. J. [1991], 'Effect of deviation from plane wave conditions on the Doppler spectrum from an ultrasonic blood flow detector', *Ultrasonics* **29**(5), 395–403. {82}

Avanzolini, G., Barbini, P., Cappello, A., Cevenini, G., Möller, D., Pohl, V. & Sikora, T. [1989], 'Electrical analogs for monitoring vascular properties in artificial heart studies', *IEEE Transactions on Biomedical Engineering* **36**(4), 462–470. {18}

Avolio, A. P. [1980], 'Multi-branched model of the human arterial system', *Medical and Biological Engineering and Computing* **18**, 709–718. {22,57,58}

Azimi, M. & Kak, A. C. [1985], 'An analytical study of Doppler ultrasound systems', *Ultrasonic Imaging* **7**, 1–48. {42}

Bamber, J. C. [1986], Speed of sound, *in* Hill [1986], chapter 5, pp. 200–224. {23}

Bascom, P. A. J. & Cobbold, R. S. C. [1990], 'Effects of transducer beam geometry and flow velocity profile on the Doppler power spectrum: a theorectical study', *Ultrasound in Medicine and Biology* **16**(3), 279–295. {34,87,100,103,112}

Bascom, P. A. J. & Cobbold, R. S. C. [1995], 'On a fractal packing approach for understanding ultrasonic backscattering from blood', *The Journal of the Acoustical Society of America* **98**(6), 3040–3049. {33}

Bascom, P. A. J. & Cobbold, R. S. C. [1996], 'Origin of the doppler ultrasound spectrum from blood', *IEEE Transactions on Biomedical Engineering* **43**(6), 562–571. {33,41}

Bascom, P. A. J., Cobbold, R. S. C. & Roelofs, B. H. M. [1986], 'Influence of spectral broadening on continuous wave Doppler ultrasound spectra: a geometric approach', *Ultrasound in Medicine and Biology* **12**(5), 387–395. {34,36}

Bascom, P. A. J., Routh, H. F. & Cobbold, R. S. C. [1988], Interpretation of power changes in Doppler signals from human blood—in vitro studies, *in* 'Proceedings of the IEEE Ultrasonics Symposium, Chicago, Illinois', pp. 985–988. {84,136}

Bastos, C. A. C. [1990], Removal of spectrum broadening resulting from non-stationarity in Doppler ultrasound signals, Master's thesis, School of Electronic Engineering Science, University of Wales—Bangor, UK. {38}

Bastos, C. A. C. & Fish, P. J. [1991], 'A Doppler signal simulator', *Clinical Physics and Physiological Measurement* **12**(2), 177–183. {40}

Bergel, D. H. [1961], 'The dynamic elastic properties of the arterial wall', *The Journal of Physiology* **156**, 458–469. {65}

Bonnefous, O. & Pesqué, P. [1986], 'Time domain formulation of pulse-Doppler ultrasound and blood velocity estimation by cross correlation', *Ultrasonic Imaging* **8**, 73–85. {31,42}

Bracewell, R. N. [1986], *The Fourier Transform and its Applications*, 2nd edn, McGraw-Hill, New York. {47,116}

Brody, W. R. & Meindl, J. D. [1974], 'Theoretical analysis of the CW Doppler ultrasonic flowmeter', *IEEE Transactions on Biomedical Engineering* **21**(3), 183–192. {40}

Burkhoff, D., Alexander, Jr., J. & Schipke, J. [1988], 'Assessment of Windkessel as a model of aortic input impedance', *American Journal of Physiology* **255**, H742–H753. {18}

Burns, P. N. [1988], Hemodynamics, *in* 'Clinical Applications of Doppler Ultrasound', Raven Press, New York, chapter 3, pp. 46–75. {63}

Cardoso, J. C. S. [1998], Investigation and Implementation of Real-Time Spectral Estimation Techniques for use with Pulsed Doppler Blood Flow Detectors, PhD thesis, School of Electronic Engineering and Computer Systems, University of Wales,Bangor, UK. {52}

Cardoso, J. C. S., Ruano, M. G. & Fish, P. J. [1996], 'Nonstationarity broadening reduction in pulsed Doppler spectrum measurements using time-frequency estimators', *IEEE Transactions on Biomedical Engineering* **43**(12), 1176–1186. {38,52,114}

Caro, C. G., Pedley, T. J., Schroter, R. C. & Seed, W. A. [1978], *The Mechanics of Circulation*, Oxford University Press, Oxford. {12,14}

Censor, D., Newhouse, V. L., Vontz, T. & Ortega, H. V. [1988], 'Theory of ultrasound Doppler-spectra velocimetry for arbitrary beam and flow configurations', *IEEE Transactions on Biomedical Engineering* **35**(9), 740–751. {35}

Chang, P. H., Shung, K. K., Wu, S.-j. & Levene, H. B. [1995], 'Second harmonic imaging and harmonic Doppler measurements with Albunex', *IEEE Transactions on Ultrasonics, Ferroelectrics, and Frequency Control* **42**(6), 1020–1027. {31}

Chen, C.-W., Shau, Y.-W. & Wu, C.-P. [1997], 'Analog transmission line model for simulation of systemic circulation', *IEEE Transactions on Biomedical Engineering* **44**(1), 90–94. {18}

Choi, H.-I. & Williams, W. J. [1989], 'Improved time-frequency representation of multicomponent signals using exponential kernels', *IEEE Transactions on Acoustics, Speech, and Signal Processing* **37**(6), 862–871. {52}

Cloutier, G., Qin, Z. & Durand, L.-G. [1996], 'Power Doppler ultrasound evaluation of the shear rate and shear stress dependences of red blood cell aggregation', *IEEE Transactions on Biomedical Engineering* **43**(5), 441–450. {33}

Cloutier, G. & Shung, K. K. [1993], 'Cyclic variation of the power of ultrasonic Doppler signals backscattered by polystyrene microspheres and porcine erythrocyte suspensions', *IEEE Transactions on Biomedical Engineering* **40**(9), 953–962. {33,84,136}

Cloutier, G., Shung, K. K. & Durand, L.-G. [1993], 'Experimental evaluation of intrinsic and nonstationary ultrasonic Doppler spectral broadening in steady and pulsatile flow loop models', *IEEE Transactions on Ultrasonics, Ferroelectrics, and Frequency Control* **40**(6), 786–795. {37,127}

Cobbold, R. S. C., Veltink, P. H. & Johnston, K. W. [1983], 'Influence of beam profile and degree of insonation on the CW Doppler ultrasound spectrum and mean velocity', *IEEE Transactions on Sonics and Ultrasonics* **30**(6), 364–370. {34}

Cohen, L. [1989], 'Time-frequency distributions—A review', *Proceedings of the IEEE* **77**(7), 941–981. {51}

Cohen, L. [1995], *Time-Frequency Analysis*, Prentice-Hall, Englewood Cliffs, New Jersey. {51}

Cox, R. H. [1969], 'Comparison of linearized wave propagation models for arterial blood flow analysis', *Journal of Biomechanics* **2**, 251–265. {18}

David, J.-Y., Jones, S. A. & Giddens, D. P. [1991], 'Modern spectral analysis techniques for blood flow velocity and spectral measurements with pulsed Doppler ultrasound', *IEEE Transactions on Biomedical Engineering* **38**(6), 589–596. {50}

de Pater, L. & van den Berg, J. [1964], 'An electrical analogue of the entire human circulatory system', *Medical Electronics and Biological Engineering* **2**, 161–166. {22}

Edwards, R. V., Angus, J. C., French, M. J. & Dunning, J. W. [1971], 'Spectral analysis of the signal from the laser Doppler flowmeter: time-independent systems', *Journal of Applied Physics* **42**(2), 837–850. {37}

Evans, D. H. [1985], 'On the measurement of the mean velocity of blood flow over the cardiac cycle using Doppler ultrasound', *Ultrasound in Medicine and Biology* **11**(5), 735–741. {34}

Evans, D. H. [1982*b*], 'Some aspects of the relationship between instantaneous volumetric blood flow and continuous wave Doppler ultrasound recordings—I. The effect of ultrasonic beam width on the ouput of maximum, mean and rms frequency processors', *Ultrasound in Medicine and Biology* **8**(6), 605–609. {15,34}

Evans, D. H. [1982*a*], 'Some aspects of the relationship between instantaneous volumetric blood flow and continuous wave Doppler ultrasound recordings—III. The calculation of Doppler power spectra from mean velocity waveforms, and the results of processing these spectra with maximum, mean, and rms frequency processors', *Ultrasound in Medicine and Biology* **8**(6), 617–623. {14,84}

Evans, D. H., McDicken, W. N., Skidmore, R. & Woodcock, J. P. [1989], *Doppler Ultrasound: Physics, Instrumentation, and Clinical Applications*, John Wiley & Sons, Chicester. {1,12,13,15,16,28,30,32,33,34,35,46,50,85,92}

Fan, L. & Evans, D. H. [1994*a*], 'Differences in the power structures of Fourier transform and autoregressive spectral estimates of narrow-band Doppler signals', *IEEE Transactions on Biomedical Engineering* **41**(4), 387–390. {50}

Fan, L. & Evans, D. H. [1994*b*], 'Extracting instantaneous mean frequency information from Doppler signals using the Wigner distribution function', *Ultrasound in Medicine and Biology* **20**(5), 429–443. {51}

Fich, S. & Li, J. K.-J. [1983], 'Aorto-ventricular dynamics: theories, experiments, and instrumentation', *Critical Reviews in Biomedical Engineering* **9**(3), 245–285. {7}

Filipczyński, L. & Etienne, J. [1972], 'Spherical focussing transducers with Gaussian surface velocity distribution', *Proceedings of Vibration Problems* **13**(2), 117–136. {82}

Fish, P. J. [1986], Doppler methods, *in* Hill [1986], chapter 11, pp. 338–376. {24,34,40,78,80,98,99,100,119}

Fish, P. J. [1990], *Physics and Instrumentation of Diagnostic Medical Ultrasound*, John Wiley & Sons, Chicester. {23,27,29,31,32}

Fish, P. J. [1991], 'Nonstationarity broadening in pulsed Doppler spectrum measurements', *Ultrasound in Medicine and Biology* **17**(2), 147–155. {2,37,116,117}

Fish, P. J. [1992], The Doppler effect and blood flow: an instrument optimisation programme, *in* D. J. McClements & M. J. Povey, eds, 'Developments in Acoustics and Ultrasonics', Institute of Physics Press, Bristol, pp. 91–127. {77,116}

Fish, P. J., Hoskins, P. R., Moran, C. & McDicken, W. N. [1997], 'Developments in cardiovascular ultrasound: Part 1: signal processing and instrumentation', *Medical and Biological Engineering and Computing* **35**, 561–569. {42}

Fort, A., Manfredi, C. & Rocchi, S. [1995], 'Adaptive SVD-based AR model order determination for time-frequency analysis of Doppler ultrasound signals', *Ultrasound in Medicine and Biology* **21**(6), 793–805. {50}

Garbini, J. L., Forster, F. K. & Jorgensen, J. E. [1982*a*], 'Measurement of fluid turbulence based on pulsed ultrasound techniques. Part 1. Analysis', *Journal of Fluid Mechanics* **118**, 445–470. {40}

Garbini, J. L., Forster, F. K. & Jorgensen, J. E. [1982*b*], 'Measurement of fluid turbulence based on pulsed ultrasound techniques. Part 2. Experimental investigation', *Journal of Fluid Mechanics* **118**, 471–505. {40}

Gill, R. W. [1985], 'Measurement of blood flow by ultrasound: accuracy and sources of error', *Ultrasound in Medicine and Biology* **11**(4), 625–641. {2,35}

Gore, J. C. & Leeman, S. [1977], 'Ultrasonic backscattering from human tissue: a realistic model', *Physics in Medicine and Biology* **22**(2), 317–326. {40}

Gosling, R. S. [1976], Extraction of physiological information from spectrum-analysed Doppler-shifted continuous-wave ultrasound signals obtained non-invasively from the arterial system, *in* D. W. Hill & B. W. Watson, eds, 'IEEE Medical Electronics Monographs 18–22', Peter Peregrinus, Stevenage, Hertfordshire, UK, chapter 4, pp. 73–125. {72}

Gradshtein, I. S. & Ryzhik, I. M. [1980], *Table of Integrals, Series, and Products*, Academic Press, New York. English translation of the Russian *Tablistsy integralov, summ, riadov i proizvedenii*, edited by Alan Jeffrey. {101}

Gray, H. [1973], *Grays's Anatomy* , 35th edn, Longman, Edinburgh. Edited by Roger Warwick and Peter L. Williams. {56}

Green, P. S. [1964], 'Spectral broadening of acoustic reverberation in Doppler-shift fluid flowmeters', *The Journal of the Acoustical Society of America* **36**(7), 1383–1390. {36}

Griffith, J. M., Brody, W. R. & Goodman, L. [1976], 'Resolution performance of Doppler ultrasound flowmeters', *The Journal of the Acoustical Society of America* **60**(3), 607–610. {36}

Gruodis, A. J. [1979], 'Transient analysis of uniform resistive transmission lines in a homogeneous medium', *IBM Journal of Research and Development* **23**(6), 675–681. {63}

Guo, Z., Durand, L.-G. & Lee, H. C. [1994*a*], 'Comparison of time-frequency distribution techniques for analysis fo simulated Doppler ultrasound signals of the femoral artery', *IEEE Transactions on Biomedical Engineering* **41**(4), 332–342. {52,114}

Guo, Z., Durand, L.-G. & Lee, H. C. [1994*b*], 'The time-frequency distributions of nonstationary signals based on a Bessel kernel', *IEEE Transactions on Signal Processing* **42**(7), 1700–1707. {52}

Guyton, A. C. [1991], *Textbook of Medical Physiology*, 8th edn, W.B. Saunders, Philadelphia. {8,9,11,17}

Hatle, L. & Anglesen, B. [1985], *Doppler Ultrasound in Cardiology*, Lea & Febiger, Philadelphia. {12,13}

Hedrick, W. R., Hykes, D. L. & Starchman, D. E. [1995], *Ultrasound physics and instrumentation*, 3rd edn, Mosby—Year Book, Inc., St. Louis, Missouri. {28,32}

Hein, I. A. & O'Brien, Jr., W. D. [1993], 'Current time-domain methods for assessing tissue motion by analysis from reflected ultrasound echoes—a review', *IEEE Transactions on Ultrasonics, Ferroelectrics, and Frequency Control* **40**(2), 84–102. {42}

Hill, C. R., ed. [1986], *Physical Principles of Medical Ultrasonics*, Ellis Horwood, Chicester. {139,142}

Hoeks, A. P. G., Hennerici, M. & Reneman, R. S. [1991], 'Spectral composition of Doppler signals', *Ultrasound in Medicine and Biology* **17**(8), 751–760. {35}

Holland, C. K., Brown, J. M., Scoutt, L. M. & Taylor, K. J. W. [1998], 'Lower extremity volumetric arterial blood flow in normal subjects', *Ultrasound in Medicine and Biology* **24**(8), 1079–1086. {66,71,72,73}

Hoskins, P. R. [1996], 'Accuracy of maximum velocity estimates made using Doppler ultrasound systems', *British Journal of Radiology* **69**(818), 172–177. {39}

Jacob, S. W., Francone, C. A. & Lossow, W. J. [1990], *Anatomia e Fisiologia Humana*, 5th edn, Editora Guanabara, Rio de Janeiro, Brasil. Portuguese translation of *Structure and Function in Man*. {9}

Jäger, K. A., Ricketts, H. J. & Strandness, Jr., D. E. [1985], Duplex scanning for the evaluation of lower limb arterial disease, *in* E. F. Bernstein, ed., 'Noninvasive Diagnostic Techniques in Vascular Disease', 3rd edn, CV Mosby, St. Louis, Missouri, chapter 60, pp. 619–631. {57,58}

Jensen, J. A. [1996], *Estimation of blood velocities using ultrasound: a signal processing approach*, Cambridge University Press, Cambridge. {32,42}

Johnston, K. W., Kassam, M. & Cobbold, R. S. C. [1983], 'Relationship between Doppler pulsatility index and direct femoral pressure measurements in the diagnosis of aortoiliac occlusive disease', *Ultrasound in Medicine and Biology* **9**(3), 271–281. {59}

Johnston, K. W., Kassam, M., Koers, J., Cobbold, R. S. C. & MacHattie, D. [1984], 'Comparative study of four methods for quantifying Doppler ultrasound waveforms from the femoral artery', *Ultrasound in Medicine and Biology* **10**(1), 1–12. {57,72}

Johnston, K. W., Maruzzo, B. C. & Cobbold, R. S. C. [1978], 'Doppler methods for quantitative measurement and localization of peripheral arterial occlusive disease by analysis of the blood flow velocity waveform', *Ultrasound in Medicine and Biology* **4**(3), 209–223. {58,59,72,73}

Jones, S. A. [1993], 'Fundamental sources of error and spectral broadening in Doppler ultrasound signals', *Critical Reviews in Biomedical Engineering* **21**(5), 399–483. {2,35,41,42,77}

Jones, S. A. & Giddens, D. P. [1990], 'A simulation of transit time effects in Doppler ultrasound signals', *Ultrasound in Medicine and Biology* **16**(6), 607–619. {41}

Kaluzynski, K. [1987], 'Analysis of application possibilities of autoregressive modelling to Doppler blood flow signal spectral analysis', *Medical and Biological Engineering and Computing* **25**, 373–376. {50}

Kaluzynski, K. [1989], 'Selection of a spectral analysis method for the assessment of velocity distribution based on the spectral distribution of ultrasonic Doppler signals', *Medical and Biological Engineering and Computing* **27**, 463–469. {50}

Kasai, C., Namekawa, K., Koyano, A. & Omoto, R. [1985], 'Real-time two-dimensional blood flow imaging using an autocorrelation technique', *IEEE Transactions on Sonics and Ultrasonics* **32**(3), 458–464. {31}

Kay, S. M. [1988], *Modern Spectral Estimation: theory and application*, Prentice-Hall, Englewood Cliffs, New Jersey. {43,44,48,49,50}

Kay, S. M. & Marple, Jr., S. L. [1981], 'Spectrum analysis—a modern perspective', *Proceedings of the IEEE* **69**(11), 1380–1419. {43,48}

Kernighan, B. W. & Ritchie, D. M. [1988], *The C programming language*, 2nd edn, Prentice-Hall, Englewood Cliffs, New Jersey. {87}

Kerr, A. T. & Hunt, J. W. [1992*a*], 'A method for computer simulation of ultrasound Doppler color flow images—I. Theory and numerical method', *Ultrasound in Medicine and Biology* **18**(10), 861–872. {42}

Kerr, A. T. & Hunt, J. W. [1992*b*], 'A method for computer simulation of ultrasound Doppler color flow images—I. Simulation results', *Ultrasound in Medicine and Biology* **18**(10), 873–879. {42}

Kikkawa, S., Yamaguchi, T., Tanishita, K. & Sugawara, M. [1987], 'Spectral broadening in ultrasonic Doppler flowmeters due to unsteady flow', *IEEE Transactions on Biomedical Engineering* **34**(5), 388–391. {37,124}

Kilner, P. J., Yang, G. Z., Mohiaddin, R. H., Firmin, D. N. & Longmore, D. B. [1993], 'Helical and retrograde secondary flow patterns in the aortic arch studied by three-dimensional magnetic resonance velocity mapping', *Circulation* **88**(5, Pt 1), 2235–2247. {136}

Kremkau, F. W. [1995], *Doppler ultrasound: principles and instruments*, 2nd edn, W.B. Saunders, Philadelphia. {27,32}

Kristoffersen, K. & Angelsen, B. A. J. [1988], 'A time-shared ultrasound Doppler measurement and 2-D imaging system', *IEEE Transactions on Biomedical Engineering* **35**(5), 285–295. {40}

Kroecker, E. J. & Wood, E. H. [1955], 'Comparison of simultaneously recorded central and peripheral arteriaal pressure pulses during rest', *Circulation Research* **3**, 623–632. Cited in [Nichols & O'Rourke 1990, p. 228]. {71,72}

Kundert, K. S. [1995], *The designer's guide to SPICE and SPECTRE*, Kluwer Academic Publishers, Boston. {59}

Lange, G. J. & Loupas, T. [1996], 'Spectral and color Doppler sonographic applications of a new test object with adjustable moving target spacing', *Journal of Ultrasound in Medicine* **15**(11), 775–784. {39}

Law, Y. F., Bascom, P. A. J., Johnston, K. W., Vaitkus, P. & Cobbold, R. S. C. [1991], 'Experimental study of the effects of pulsed Doppler sample volume size and position on the Doppler spectrum', *Ultrasonics* **29**(5), 404–410. {39}

Law, Y. F., Cobbold, R. S. C., Johnston, K. W. & Bascom, P. A. J. [1987], 'Computer-controlled pulsatile pump system for physiological flow simulation', *Medical and Biological Engineering and Computing* **25**, 590–595. {39}

Law, Y. F., Johnston, K. W., Routh, H. F. & Cobbold, R. S. C. [1989], 'On the design and evaluation of a steady flow model for Doppler ultrasound studies', *Ultrasound in Medicine and Biology* **15**(5), 505–516. {39}

Loupas, T. & McDicken, W. N. [1990], 'Low-order complex AR models for mean and maximum frequency estimation in the context of Doppler color flow mapping', *IEEE Transactions on Ultrasonics, Ferroelectrics, and Frequency Control* **37**(6), 590–601. {50}

Mat [1998], *MATLAB Function Reference*, The MathWorks, Inc., 24 Prime Park Way, Natick, MA 01760-1500, USA. {87}

McCarty, K. & Locke, D. J. [1986], Test objects for the assessment of the performance of Doppler shift flowmeters, *in* J. A. Evans, ed., 'Physics in Medical Ultrasound', The Institute of Physical Sciences in Medicine, 47, Belgrave Square, London SW1X 8QX, UK, chapter 12, pp. 94–106. {39}

McIlroy, M. B., Seitz, W. S. & Targett, R. C. [1986], 'A transmission line model of the aorta and its branches', *Cardiovascular Research* **20**, 581–587. {22}

Meire, H. B. & Farrant, P. [1995], *Basic ultrasound*, John Wiley & Sons, Chicester. {32}

Milnor, W. R. [1989], *Hemodynamics*, 2nd edn, Williams & Wilkins, Baltimore. {7,12,17,20,21,57,62,68,70,71,75,124}

Mo, L. Y. L. [1990], A unifying approach to modelling the backscattered Doppler ultrasund from blood, PhD thesis, Department of Electrical Egineering and Institute of Biomedical Engineering, University of Toronto, Canada. {42}

Mo, L. Y. L., Bascom, P. A. J., Ritchie, K. & McCowan, L. M. E. [1988], 'A transmission line modelling approach to the interpretation of uterine Doppler waveforms', *Ultrasound in Medicine and Biology* **14**(5), 365–376. {18,22}

Mo, L. Y. L. & Cobbold, R. S. C. [1986], "'Speckle" in continuous wave Doppler ultrasound spectra: a simulation study', *IEEE Transactions on Ultrasonics, Ferroelectrics, and Frequency Control* **33**(6), 747–752. {40,41}

Mo, L. Y. L. & Cobbold, R. S. C. [1989], 'A nonstationary signal simulation model for continuous wave and pulsed Doppler ultrasound', *IEEE Transactions on Ultrasonics, Ferroelectrics, and Frequency Control* **36**(5), 522–530. {41,78}

Mo, L. Y. L. & Cobbold, R. S. C. [1992], 'A unified approach to modelling the backscattered Doppler ultrasound from blood', *IEEE Transactions on Biomedical Engineering* **39**(5), 450–461. {41,78,79,84,136}

Mo, L. Y. L. & Cobbold, R. S. C. [1993], Theoretical models of ultrasonic scattering in blood, *in* Shung & Thieme [1993*b*], chapter 5, pp. 125–170. {42}

Morse, P. M. & Ingard, K. U. [1986], *Theoretical Acoustics*, Princeton University Press, Princeton, New Jersey. {25}

Newhouse, V. L., Bendick, F. J. & Varner, L. W. [1976], 'Analysis of transit time effects on Doppler flow measurement', *IEEE Transactions on Biomedical Engineering* **23**(5), 381–387. {36}

Newhouse, V. L., Furgason, E. S., Johnson, G. F. & Wolf, D. A. [1980], 'The dependence of ultrasound Doppler bandwidth on beam geometry', *IEEE Transactions on Sonics and Ultrasonics* **27**(2), 50–59. {37}

Newhouse, V. L. & Reid, J. M. [1990], 'Invariance of Doppler bandwidth with flow axis displacement', *Proceedings of the IEEE Ultrasonics Symposium, Honolulu, Hawai* **3**, 1533–1536. {37,39}

Newhouse, V. L., Varner, L. W. & Bendick, P. J. [1977], 'Geometrical spectrum broadening in ultrasonic Doppler systems', *IEEE Transactions on Biomedical Engineering* **24**(5), 478–480. {36,37}

Nichols, W. W. & O'Rourke, M. F. [1990], *McDonald's Blood Flow in Arteries: Theorectical, Experimental and Clinical Principles*, 3rd edn, Edward Arnold, London. {7,65,146}

Noordergraaf, A. [1969], Hemodynamics, *in* H. P. Schwan, ed., 'Biological Engineering', McGraw-Hill, New York, chapter 5, pp. 391–545. {7,19,21}

Noordergraaf, A. [1978], *Circulatory System Dynamics*, Academic Press, New York. {18,66}

Olinger, M. & Siegel, M. [1981], 'A simulation study and theoretical comparison of various processing techniques used in ultrasonic bloodflow measurement', *Ultrasonic Imaging* **3**, 294–302. {42}

Oppenheim, A. V. & Schafer, R. W. [1975], *Digital Signal Processing*, Prentice-Hall International, London. {44,45}

Oung, H. & Forsberg, F. [1996], 'Doppler ultrasound simulation model for pulsatile flow with nonaxial components', *Ultrasonic Imaging* **18**(3), 157–172. {42}

Papoulis, A. [1988], *Signal Analysis*, McGraw-Hill, New York. {116}

Papoulis, A. [1991], *Probability, Random Variables and Stochastic Processes*, 3rd edn, McGraw-Hill, New York. {42,83,115}

Patel, D. J., Greenfield, Jr., J. C., Austen, W. G., Morrow, A. G. & Fry, D. L. [1965], 'Pressure-flow relationships in the ascending aorta and femoral artery of man', *Journal of Applied Physiology* **20**(3), 459–463. {70}

Polak, J. F. [1995], Color flow and Duplex sonography in lower-extremity ischemia, *in* Taylor et al. [1995], chapter 16, pp. 337–354. {26}

Porat, B. [1994], *Digital Processing of Random signals: theory and methods*, Prentice-Hall, Englewood Cliffs, New Jersey. {45,50,51}

PSPICE [1993], *Circuit Analysis Reference Manual*, MicroSim Corporation, 20 Fairbanks, Irvine, California, CA 92718, USA. {59}

Raines, J. K., Jaffrin, M. Y. & Shapiro, A. H. [1974], 'A computer simulation of arterial dynamics in the human leg', *Journal of Biomechanics* **7**, 77–91. {22,63,67}

Rashid, M. H. [1990], *SPICE for Circuits and Electronics Using PSpice*, Prentice-Hall, Englewood Cliffs, New Jersey. {59}

Rayleigh, L. [1872], 'Investigation of the disturbance produced by a spherical obstacle on the waves of sound', *Proceedings of the London Mathematical Society* **4**, 253–287. {32}

Reith, E. J., Breidenbach, B. & Lorenc, M. [1978], *Textbook of Anatomy and Physiology*, 2nd edn, McGraw-Hill, New York. {8,11,57}

Rizzi, P. A. [1988], *Microwave Engineering—Passive Circuits*, Prentice-Hall International, Englewood Cliffs, New Jersey. {64}

Roth, A. C., Young, D. F. & Cholvin, N. R. [1976], 'Effect of collateral and peripheral resistance on blood flow through arterial stenoses', *Journal of Biomechanics* **9**, 367–375. {74}

Routh, H. F., Law, Y. F., Mo, L. Y. L., Ojha, M., Vaitkus, P. J., Cobbold, R. S. C., Johnston, K. W. & Bascom, P. A. J. [1989], 'Role of models in understanding and interpreting clinical Doppler ultrasound', *Medical Progress through Technology* **15**, 155–169. {38}

Ruano, M. G. & Fish, P. J. [1993], 'Cost/benefit criterion for selection of pulsed Doppler ultrasound spectral mean frequency and bandwidth estimators', *IEEE Transactions on Biomedical Engineering* **40**(12), 1338–1341. {50}

Rubin, J. M., Bude, R. O., Carson, P. L., Bree, R. L. & Adler, R. S. [1994], 'Power Doppler US: a potentially useful alternative to mean frequency—based color Doppler US', *Radiology* **190**, 853–856. {31}

Russell, S. V., McHugh, D. & Moreman, B. R. [1993], 'A programmable Doppler string test object', *Physics in Medicine and Biology* **38**(11), 1623–1630. {39}

Satomura, S. [1957], 'Ultrasonic Doppler method for the inspection of cardiac functions', *The Journal of the Acoustical Society of America* **29**(11), 1181–1185. {23,27}

Schlindwein, F. S. & Evans, D. H. [1989], 'A real-time autoregressive spectrum analyzer for Doppler ultrasound signals', *Ultrasound in Medicine and Biology* **15**(3), 263–272. {50}

Schlindwein, F. S. & Evans, D. H. [1990], 'Selection of the order of autoregressive models for spectral analysis of Doppler ultrasound signals', *Ultrasound in Medicine and Biology* **16**(1), 81–91. {50}

Sheldon, C. D. & Duggen, T. C. [1987], 'Low-cost Doppler signal simulator', *Medical and Biological Engineering and Computing* **25**, 226–228. {40}

Shung, K. K. [1982], 'On the ultrasound scattering from blood as a function of hematocrit', *IEEE Transactions on Sonics and Ultrasonics* **29**(6), 327–331. {33}

Shung, K. K., Cloutier, G. & Lim, C. C. [1992], 'The effects of hematocrit, shear rate, and turbulence on ultrasonic Doppler spectrum from blood', *IEEE Transactions on Biomedical Engineering* **39**(5), 462–469. {33,39}

Shung, K. K., Siegelmann, R. A. & Reid, J. M. [1976], 'Scattering of ultrasound by blood', *IEEE Transactions on Biomedical Engineering* **23**(6), 460–467. {32,33,40}

Shung, K. K. & Thieme, G. A. [1993*a*], Biological tissues as ultrasonic scattering media, in *Ultrasonic Scattering in Biological Tissues* [Shung & Thieme 1993*b*], chapter 3, pp. 53–74. {33}

Shung, K. K. & Thieme, G. A., eds [1993*b*], *Ultrasonic Scattering in Biological Tissues*, CRC Press Florida, Boca Raton, Florida. {147,150}

Shung, K. K., Yuan, Y. W., Fei, D. Y. & Tarbell, J. M. [1984], 'Effect of flow disturbance on ultrasonic backscatter from blood', *The Journal of the Acoustical Society of America* **75**(4), 1265–1272. {33}

Skolnik, M. [1970], *Radar Handbook*, McGraw-Hill, New York. {116}

Snyder, M. F., Rideout, V. C. & Hillestad, R. J. [1968], 'Computer modeling of the human systemic arterial tree', *Journal of Biomechanics* **1**, 341–353. {22}

Stanier, M. W. & Forsling, M. L. [1990], *Physiological Processes: an Introduction to Mammalian Physiology*, McGraw-Hill, London. {8,9,10}

Talhami, H. E. & Kitney, R. I. [1988], 'Maximum likelihood frequency tracking of the audio pulsed Doppler ultrasound signal using a Kalman filter', *Ultrasound in Medicine and Biology* **14**(7), 599–609. {41}

Taylor, K. J. W., Burns, P. N. & Wells, P. N. T., eds [1995], *Clinical Applications of Doppler Ultrasound*, 2nd edn, Raven Press, New York. {32,149}

Thompson, R. S. & Trudinger, B. J. [1990], 'Doppler waveform pulsatility index and resistence, pressure and flow in the umbilical placental circulation: an investigation using a mathematical model', *Ultrasound in Medicine and Biology* **16**(5), 449–458. {59}

Tortoli, P., Guidi, G., Guidi, F. & Atzeni, C. [1994], 'A review of experimental transverse Doppler studies', *IEEE Transactions on Ultrasonics, Ferroelectrics, and Frequency Control* **41**(1), 84–89. {39}

Tortoli, P., Guidi, G., Mariotti, V. & Newhouse, V. L. [1992], 'Experimental proof of Doppler bandwith invariance', *IEEE Transactions on Ultrasonics, Ferroelectrics, and Frequency Control* **39**(2), 196–203. {37,39}

Toy, S. M., Melvin, J. & Noordergraaf, A. [1985], 'Reduced models of arterial systems', *IEEE Transactions on Biomedical Engineering* **32**(2), 174–176. {18}

Tuinenga, P. W. [1988], *SPICE: A Guide to Circuit Analysis Using PSPICE*, Prentice-Hall, Englewood Cliffs, New Jersey. {59}

Vaitkus, P. J. & Cobbold, R. S. C. [1988], 'A comparative study and assessment of Doppler ultrasound spectral techniques part I: estimation methods', *Ultrasound in Medicine and Biology* **14**(8), 661–672. {50}

Vaitkus, P. J., Cobbold, R. S. C. & Johnston, K. W. [1988], 'A comparative study and assessment of Doppler ultrasound spectral techniques part II: methods and results', *Ultrasound in Medicine and Biology* **14**(8), 673–688. {50}

van Leeuwen, G. H., Hoeks, A. P. G. & Reneman, R. S. [1986], 'Simulation of real-time frequency estimators for pulsed Doppler systems', *Ultrasonic Imaging* **8**, 252–271. {40,78}

Wang, Y. & Fish, P. J. [1996], 'Arterial Doppler signal simulation by time domain processing', *European Journal of Ultrasound* **3**, 71–81. {40}

Wang, Y. & Fish, P. J. [1997], 'Correction for nonstationarity and window broadening in Doppler spectrum estimation', *IEEE Signal Processing Letters* **4**(1), 18–20. {35,38,113,116}

Wendling, F. [1991], Simulation of Doppler ultrasound signals for a laminar, pulsatile, nonuniform flow, Master's thesis, School of Mechanical Engineering Science, Georgia Institue of Technology, Georgia, USA. {39}

Wendling, F., Jones, S. A. & Giddens, D. P. [1992], 'Simulation of Doppler ultrasound signals for a laminar, pulsatile, nonuniform flow', *Ultrasound in Medicine and Biology* **18**(2), 179–193. {41,78}

Westerhof, N., Bosman, F., De Vries, C. J. & Noordergraaf, A. [1969], 'Analog studies of the human systemic arterial tree', *Journal of Biomechanics* **2**(2), 121–143. {22,57,58,61}

Westerhof, N., Elzinga, G. & Sipkema, P. [1971], 'An artificial arterial system for pumping hearts', *Journal of Applied Physiology* **31**(5), 776–781. {18}

Willink, R. D. & Evans, D. H. [1996], 'The effect of geometrical spectral broadening on the estimation of mean blood velocity using wide and narrow ultrasound beams', *IEEE Transactions on Biomedical Engineering* **43**(3), 238–248. {37}

Womersley, J. R. [1955*a*], 'Method for the calculation of velocity, rate of flow and viscous drag in arteries when the pressure gradient is known', *The Journal of Physiology* **127**, 553–563. {14,18,19}

Womersley, J. R. [1955*b*], 'Oscillatory motion of a viscous liquid in a thin-walled elastic tube—I: The linear approximation for long waves', *Philosophical Magazine* **46**, 199–221. {18}

Womersley, J. R. [1957], 'Oscillatory flow in arteries: the constrained elastic tube as a model of arterial flow and pulse transmission', *Physics in Medicine and Biology* **2**, 178–187. {18}

Wu, S. J. & Shung, K. K. [1996], 'Cyclic variation of Dopler power from whole blood under pulsatile flow', *Ultrasound in Medicine and Biology* **22**(7), 883–894. {84,136}

Young, D. F. [1979], 'Fluid mechanics of arterial stenoses', *ASME Journal of Biomechanical Engineering* **101**, 157–175. {74}

Young, D. F., Cholvin, N. R. & Roth, A. C. [1975], 'Pressure drop across artificially induced stenoses in the femoral arteries of dogs', *Circulation Research* **36**, 735–743. {16}

Young, D. F. & Tsai, F. Y. [1973*a*], 'Flow characteristics in models of arterial stenoses—I. Steady flow', *Journal of Biomechanics* **6**(4), 395–410. {74}

Young, D. F. & Tsai, F. Y. [1973*b*], 'Flow characteristics in models of arterial stenoses—II. Unsteady flow', *Journal of Biomechanics* **6**(5), 547–559. {74}

Yuan, Y. W. & Shung, K. K. [1988*a*], 'Ultrasonic backscatter from flowing whole blood. I: Dependence on shear rate and hematocrit', *The Journal of the Acoustical Society of America* **84**(1), 52–58. {33}

Yuan, Y. W. & Shung, K. K. [1988*b*], 'Ultrasonic backscatter from flowing whole blood. II: Dependence on frequency and fibrinogen concentration', *The Journal of the Acoustical Society of America* **84**(4), 1195–1200. {33}

Zeira, A., Zeira, E. M. & Holland, S. C. [1994], 'Pseudo-Wigner distribution for analysis of pulsed Doppler ultrasound', *IEEE Transactions on Ultrasonics, Ferroelectrics, and Frequency Control* **41**(3), 346–352. {52}